

**Observing surface properties of glaciers
A case study in the Nyainqêntanglha Range, Tibetan Plateau**

Shi, Junchao

DOI

[10.4233/uuid:ee8a035d-95ad-472c-9111-7044e058f9ee](https://doi.org/10.4233/uuid:ee8a035d-95ad-472c-9111-7044e058f9ee)

Publication date

2017

Document Version

Final published version

Citation (APA)

Shi, J. (2017). *Observing surface properties of glaciers: A case study in the Nyainqêntanglha Range, Tibetan Plateau*. [Dissertation (TU Delft), Delft University of Technology].
<https://doi.org/10.4233/uuid:ee8a035d-95ad-472c-9111-7044e058f9ee>

Important note

To cite this publication, please use the final published version (if applicable).
Please check the document version above.

Copyright

Other than for strictly personal use, it is not permitted to download, forward or distribute the text or part of it, without the consent of the author(s) and/or copyright holder(s), unless the work is under an open content license such as Creative Commons.

Takedown policy

Please contact us and provide details if you believe this document breaches copyrights.
We will remove access to the work immediately and investigate your claim.

Observing surface properties of glaciers

A case study in the Nyainqêntanglha Range, Tibetan Plateau



Observing surface properties of glaciers
A case study in the Nyainqêntanglha Range, Tibetan Plateau

Proefschrift

ter verkrijging van de graad van doctor
aan de Technische Universiteit Delft,
op gezag van de Rector Magnificus prof. ir. K. C. A. M. Luyben,
voorzitter van het College voor Promoties,
in het openbaar te verdedigen op dinsdag 16 mei 2017 om 10:00 uur

door

Junchao Shi

Bachelor of Science in Hydrology and Water Resource Engineering
geboren te Zhengzhou, China.

Dit proefschrift is goedgekeurd door de promotor:

Prof. dr. M. Menenti

Copromotor: Dr. R. C. Lindenberg

Samenstelling promotiecommissie:

| | |
|-----------------------|---|
| Rector Magnificus, | voorzitter |
| Prof. dr. M. Menenti, | Technische Universiteit Delft, promotor |
| Dr. R. C. Lindenberg, | Technische Universiteit Delft, copromotor |

Onafhankelijke leden:

| | |
|------------------------------|---|
| Prof. dr. ir. R. F. Hanssen, | Technische Universiteit Delft |
| Dr. S. Lhermitte, | Technische Universiteit Delft |
| Prof. dr. B. Su, | Twente Universiteit |
| Prof. dr. L. Ren, | Hohai Univeristy |
| Prof. dr. A. P. Siebesma, | Technische Universiteit Delft, reservelid |



Copyright © 2017 by Junchao Shi

All rights reserved. No part of the material protected by this copyright notice may be reproduced or utilized in any form or any means, electronic, mechanical, including photocopying, recording or by any information storage and retrieval system, without the prior permission of the author.

Typeset by the author with Latex documentation system

ISBN 000-00-0000-000-0

An electronic version of this dissertation is available at

<http://repository.tudelft.nl/>.

*Science is a wonderful thing
if one does not have to earn one's living at it.*

Albert Einstein



Contents

| | |
|---|------------|
| Summary | xi |
| Samenvatting | xv |
| Acknowledgments | xix |
| 1 Introduction | 1 |
| 1.1 Tibetan Plateau (TP) | 1 |
| 1.2 Regional Climate | 2 |
| 1.2.1 Warming influence | 3 |
| 1.2.2 Precipitation | 4 |
| 1.3 Response of glaciers to climate change | 4 |
| 1.4 Roadmap of this dissertation | 5 |
| 1.4.1 Research questions | 5 |
| 1.4.2 Organization of the dissertation | 5 |
| 2 Background | 7 |
| 2.1 Glaciers on the Tibetan Plateau | 7 |
| 2.2 Mass balance | 8 |
| 2.3 Surface process | 9 |
| 2.3.1 Surface mass balance | 9 |
| 2.3.2 Surface energy balance | 9 |
| 2.4 Surface roughness | 10 |
| 2.4.1 Influence on surface energy balance | 10 |
| 2.4.2 Development of surface roughness parameterization | 12 |
| 2.5 Glacier motion | 12 |
| 2.6 Nyainqêntanglha Range | 14 |
| 2.6.1 Geo-environment | 14 |
| 2.6.2 Established in situ measurement | 15 |
| 3 Parameterize surface roughness based on ICESat/GLAS full waveforms | 21 |
| 3.1 Introduction | 22 |
| 3.2 Study area and Data | 23 |
| 3.2.1 Study area | 23 |

| | | |
|----------|--|-----------|
| 3.2.2 | 2.2 ICESat/GLAS data | 24 |
| 3.2.3 | ASTER GDEM data | 24 |
| 3.3 | Methods. | 26 |
| 3.3.1 | Slope and roughness derived from ASTER GDEM | 26 |
| 3.3.2 | ICESat full waveform fitting process | 27 |
| 3.4 | Results. | 31 |
| 3.4.1 | ICESat full waveform examples over the study area | 32 |
| 3.4.2 | Comparison of parameters derived from ASTER GDEM and ICESat data | 35 |
| 3.4.3 | Analysis of ICESat full waveform parameters as a function of morphology | 36 |
| 3.5 | Conclusions. | 37 |
| 4 | Estimating glacier surface displacements | 47 |
| 4.1 | Introduction | 48 |
| 4.1.1 | Significance of surface displacement in glacier dynamics. | 48 |
| 4.1.2 | Significance of glaciers in the Nyainqêntanglha Range | 49 |
| 4.2 | Data Description | 51 |
| 4.3 | Methodology | 52 |
| 4.3.1 | Displacement derivation. | 54 |
| 4.3.2 | Post-processing and precision assessment | 56 |
| 4.3.3 | Displacement variability estimation | 58 |
| 4.4 | Results. | 61 |
| 4.5 | Discussion | 69 |
| 4.6 | Conclusions. | 69 |
| 5 | Response of glaciers to regional climate forcing | 71 |
| 5.1 | Introduction | 72 |
| 5.2 | Data | 76 |
| 5.2.1 | Land surface temperature (MODIS day, night) | 76 |
| 5.2.2 | Precipitation (TRMM) | 76 |
| 5.2.3 | Ancillary datasets. | 77 |
| 5.2.4 | Preprocessing of MODIS and TRMM | 77 |
| 5.3 | Analysis of monsoon temporal pattern | 77 |
| 5.4 | Response of glaciers with regional climate | 79 |
| 5.4.1 | Proposed mechanism of response. | 79 |
| 5.4.2 | Estimating temporal response. | 80 |
| 5.5 | Results. | 82 |
| 5.5.1 | Characterization of regional climate | 82 |
| 5.5.2 | Temporal patterns in precipitation and temperature | 88 |
| 5.5.3 | The interaction of ice flow with regional climate. | 90 |

| | | |
|----------|--|------------|
| 5.5.4 | Estimating the trend and amplitude of ice surface flow | 92 |
| 5.6 | Conclusions. | 95 |
| 6 | Conclusions and future work | 99 |
| 6.1 | Conclusions. | 99 |
| 6.2 | Future work. | 102 |
| | Curriculum Vitæ | 103 |
| | List of Publications | 105 |
| | References | 107 |



Summary

The state of glaciers on the Earth is recognized as a good indicator of the changing climate. A large amount of global freshwater is blocked within the glaciers on the continental surface. As the most elevated plateau in the world, the Tibetan Plateau is located in the southwestern part of China, central Asia. It stretches over $\sim 2.5 \times 10^6$ km² between the Taklamakan Desert and the Himalaya Mountains, over $\sim 20^\circ$ longitude ($78^\circ 25' \text{E} \sim 99^\circ 06' \text{E}$) and $\sim 10^\circ$ latitude ($26^\circ 44' \text{N} \sim 36^\circ 32' \text{N}$). Glaciers on the Tibetan Plateau are the main reservoirs of water that benefit the people living around several major Asian rivers downstream. The high elevation and morphology of the Tibetan Plateau (TP over 4000 m), influence the regional atmosphere circulations, i.e. the westerlies from inland of Eurasia and monsoons from Indian and East Asia. The land surface energy balance determines heating of the atmosphere at high elevation across a range of spatial and temporal scales resulting in a highly variable radiative and convective forcing. The latter does also apply to glaciers, with impacts on the mass balance of glaciers in the Tibetan Plateau. However, the understanding of the interactions between atmosphere and Tibetan glaciers still needs to be improved further.

The surface properties of glaciers characterize the interaction between the atmospheric boundary layer and glaciers. Traditionally, the surface properties of glaciers are either observed in situ or estimated by some retrieval approaches.

This dissertation describes remote sensing observations of two glacier properties:

- a) The surface roughness;
- b) The ice velocity of glacier surface flow.

This study focused on the Nyainqêntanglha Range on the Tibetan Plateau.

The specific results of the main work of this dissertation are summarized below.

Chapter 3 presents the potential parameterization of surface roughness using the spaceborne laser altimetry data. Glaciers in the Tibetan mountains are expected to be sensitive to turbulent sensible and latent heat fluxes. One of the most significant factors of the energy exchange between the atmospheric boundary layer and glacier is the roughness of the glacier surface. The aerodynamic roughness of a complex surface like a glacier is related to its geometric characteristics at multiple spatial scales. Methods to parameterize this roughness for

glaciers surface were applied in the remote regions of TP. In this study a two-stage approach was applied. First, the capability of return waveforms to characterize TP landscapes was evaluated. Extraction of parameters of waveforms measured by the ICESat/GLAS laser system from February, 2003 to November, 2004 was evaluated by analyzing data along several tracks across glaciers in the Nyainqêntanglha range. Surface features, namely roughness, slope and elevation were retrieved independently from ASTER GDEM. The response of GLAS waveforms to these glacier surface features has been documented by statistics on full waveform parameters, namely number of modes, width of the full waveform and elevation. These statistics show that the GLAS waveforms are related to the surface geometric features and useful to parameterize the surface aerodynamic roughness. Consequently, the retrieved waveform can be explained by the terrain characteristics. In our study area, roughness and slope of the surface can contribute several meters to even several tens of meters to the pulse shape. Next, the relationship between surface slope and roughness was derived first theoretically, then using the ASTER GDEM surface features and the observed GLAS waveform parameters. The later delivered the relationship between terrain characteristics and waveform parameters required to parameterize the surface aerodynamic roughness.

Chapter 4 shows the derivation of glacial surface displacements by applying feature-tracking methods to optical imageries. The glacier surface flow responds to changes in accumulation and ablation and through that, to regional climate, but must be mapped and monitored over long periods of time. We monitored the ice surface displacement of the glaciers in the entire Nyainqêntanglha Range over nearly two decades from 1993 to 2015 by applying a feature-tracking method to multi-temporal Landsat image data. Suitable images could only be retrieved in the non-monsoon season and were spaced by about one year, so that our estimates were approximately yearly values. Post-processing was applied to detect outliers, taking into account estimated spatial variability, towards higher quality of retrieved surface displacements. It reduces the bias existing in the final displacement measurements on the mountainous glaciers. The precision of ice displacement was evaluated by using measurements on the relative stable ground outside glaciers. Through the time series analysis of ice surface displacements, we found that the observations could be represented by a combination of a linear component and multi-annual component. This applied especially to the ablation zone of observed glaciers. The multi-annual component could be represented by a single periodic component with a period of multiple years. In practice, we estimated and mapped the linear trend ν and the amplitude of multi-annual component a . By capturing their spatial distributions we could evaluate their dependence on both elevation and slope. The observed glaciers

are active, as documented by the linear trend and amplitude of multi-annual component across the entire range of elevation and slope. The analysis indicates that the spatial variability of glacier multi-annual amplitude seems to be more dependent on elevations and slope than the linear trend in the Nyainqêntanglha Range. The study demonstrated that observations of ice surface displacement retrieved by optical image data provide useful insight on the glacier dynamics in the Nyainqêntanglha Range.

Chapter 5 further estimates the possible temporal patterns of the glacial surface displacements response within the Nyainqêntanglha Range under the regional climate. In this study, the regional climate has been characterized using TRMM precipitation and the MODIS land surface temperature data products, while the local glacier response to regional climate has been characterized using the period, linear trend and amplitude of the periodic component of glacier surface flow. The analysis of monthly precipitation and land surface temperature led to define seasons as they occur on the Tibetan Plateau. Most important for glaciers mass balance is the summer monsoon season when both high precipitation and high surface temperature occur. The statistical dependency of ice flow on precipitation and temperature was estimated by multi-regression analysis. According to the interaction between regional climate (precipitation and temperature) and glaciers, the linear trend and amplitude of periodic component of glacier surface displacement times series was evaluated by using FFT analysis combined with the least squares approach. Applying FFT analysis and least squares approach to regional climate forcing (precipitation and temperature) and ice flow in terms of surface displacement times series, the temporal patterns of ice flow are estimated. It indicates that the behavior of ice flow relates the patterns of glacier self-adjustment induced by regional climate forcing (temperature and precipitation). These findings imply that satellite based feature tracking method is capable to establish long term time series of ice flows and estimate interactions with regional climate variables in this region.



Samenvatting

De staat van gletsjers op aarde wordt gezien als een goede indicator voor het veranderende klimaat. Een grote hoeveelheid van het wereldwijde zoetwater is opgeslagen in gletsjers op het continentale landoppervlak. Het hoogste plateau ter wereld is het Tibetaanse Plateau, gelegen in het zuidwestelijke deel van China, Centraal-Azië. Het strekt zich uit over meer dan $2,5 \times 10^6 \text{ km}^2$ tussen de Taklamakan-woestijn en de bergen van de Himalaya over 20° lengte ($78^\circ 25' \text{E}$ $99^\circ 06' \text{E}$) en 10° breedte ($26^\circ 44' \text{N}$ $36^\circ 32' \text{N}$). Gletsjers op het Tibetaanse plateau zijn de belangrijkste waterreservoirs waaruit de mensen die stroomafwaarts rond de meerdere grote Aziatische rivieren leven, water kunnen putten. De hoogte en morfologie van het Tibetaanse Plateau (TP boven 4000 m) beïnvloedt de regionale atmosferische stromingen, met name de westelijke binnenlanden van Eurasië en moessons uit India en Oost-Azië. De energiebalans op het landoppervlak bepaalt de verwarming van de atmosfeer op grote hoogte over een reeks ruimtelijke en temporele schalen, wat resulteert in een zeer variabele stralings- en convectiekracht. Het laatste geldt ook voor gletsjers, met gevolgen voor de massabalans van gletsjers op het Tibetaanse Plateau. Echter, het begrijpen van de interacties tussen de atmosfeer en Tibetaanse gletsjers moet nog verder worden verbeterd. De oppervlakte-eigenschappen van gletsjers karakteriseren de wisselwerking tussen de atmosferische grenslaag en gletsjers. Traditioneel gezien worden de oppervlakkenmerken van gletsjers ofwel in situ waargenomen of geschat met behulp van benaderingswijzen voor gegevensontsluiting. Dit proefschrift beschrijft de remote sensing-waarnemingen van twee gletsjereigenschappen:

- a) de oppervlakteruwheid;
- b) De ijsnelheid van de gletsjeroppervlaktestroom.

Deze studie richtte zich op het Nyainqêntanglha gebied op het Tibetaanse Plateau.

De specifieke resultaten van het voornaamste werk van dit proefschrift worden samengevat hieronder.

Hoofdstuk 3 beschrijft de potentiële parametrisering van de oppervlakteruwheid door gebruik te maken van laserhoogtemetingen afkomstig van satellieten. Gletsjers in de Tibetaanse bergen zullen naar verwachting gevoelig zijn voor turbulent-gevoelige en latente warmtestromen. Een van de belangrijkste factoren van de energie-uitwisseling tussen de atmosferische grenslaag en gletsjer is de ruwheid van het gletsjeroppervlak. De aerodynamische ruwheid van een

complex oppervlak als een gletsjer is gerelateerd aan zijn geometrische kenmerken op meerdere ruimtelijke schalen. Methoden om deze ruwheid te parametriseren voor gletsjersoppervlakten werden toegepast op de afgelegen gebieden van TP. In deze studie is een tweetrapsbenadering toegepast. Als eerste werd bekeken of de ontvangen golfvormen in staat zijn om TP-landschappen te karakteriseren. De parameters van de golfvormen, welke zijn gemeten door het ICESat/GLAS lasersysteem van februari 2003 tot november 2004, zijn verkregen door gegevens te analyseren langs verschillende sporen over gletsjers in het Nyainqêntanglha gebied. Oppervlaktekenmerken, in de vorm van ruwheid, helling en hoogte, zijn op onafhankelijke wijze verkregen van ASTER GDEM. De response van GLAS-golfvormen van deze gletsjeroppervlaktekenmerken is vastgelegd in statistieken welke de volledige golfvormparameters beschrijven, namelijk aantal modes, breedte van het volledige golfvorm en de hoogte. Uit deze statistieken blijkt dat de GLAS-golfvormen zijn gerelateerd aan de oppervlaktegerelateerde geometrische eigenschappen en geschikt zijn om de oppervlaktegerelateerde aerodynamische ruwheid te parametriseren. Als gevolg hiervan kan de verkregen golfvorm worden verklaard door de terreinkenmerken. In ons studiegebied kunnen de ruwheid en de helling van het oppervlak meerdere meters tot zelfs enkele tientallen meter bijdragen aan de golfvorm. Vervolgens werd de relatie tussen oppervlaktehelling en ruwheid eerst theoretisch afgeleid en vervolgens gebruikmakend van de ASTER GDEM-oppervlaktekenmerken en de waargenomen GLAS-golfvormparameters. Het laatstgenoemde resulteerde in de relatie tussen terreinkarakteristieken en golfvormparameters die nodig zijn om de oppervlakte-gerelateerde aerodynamische ruwheid te parametriseren.

Hoofdstuk 4 beschrijft de derivatie van glaciële oppervlakverplaatsingen door toepassing van feature-tracking methodes op optische beelden. De gletsjeroppervlaktestroom komt overeen met veranderingen in accumulatie en ablatie en daardoor ook met het lokale klimaat, maar moet over lange perioden in kaart worden gebracht en gemonitord. We hebben de ijsoppervlakteverplaatsing van de gletsjers in het gehele Nyainqêntanglha gebied over bijna twee decennia van 1993 tot 2015 gemonitord door een feature-tracking methode toe te passen op multi-temporele Landsat beeldgegevens. Geschikte afbeeldingen kunnen alleen in het niet-moessonseizoen worden verkregen en lagen ongeveer een jaar uit elkaar met als gevolg dat we ruwweg jaarlijkse schattingen hebben verkregen. Nabewerking werd toegepast om uitschieters te detecteren, rekening houdend met de geschatte ruimtelijke variabiliteit, om zodoende een hogere kwaliteit van de geschatte oppervlakverplaatsingen te verkrijgen. Het vermindert de afwijking in de uiteindelijke metingen van verplaatsing op de bergachtige gletsjers. De precisie van ijsverplaatsing is verkregen door middel van metingen op de relatief stabiele grond buiten de gletsjers. Met behulp van tijdreeksanalyse van ijsopper-

vlakverplaatsingen kwam naar voren dat de observaties kunnen worden weergegeven door een combinatie van een lineair onderdeel en meerjarencomponent. Dit geldt vooral voor de ablatiezone van waargenomen gletsjers. Het meerjarencomponent kan worden uitgedrukt door een enkel periodiek component met een periode van meerdere jaren. In de praktijk hebben we de lineaire trend v en de amplitude van meerjarencomponent a geschat en in kaart gebracht. Door hun ruimtelijke verdeling vast te leggen, konden we hun afhankelijkheid analyseren met betrekking tot hoogte en helling. De waargenomen gletsjers zijn actief, zoals vernomen door de lineaire trend en amplitude van het meerjarencomponent over de gehele spanne van hoogte en helling. Uit de analyse blijkt dat de ruimtelijke variabiliteit van de gletsjers' meerjarige amplitude meer afhankelijk is van hoogten en hellingen dan de lineaire trend in het Nyainqêntanglha gebied. Uit de studie bleek dat waarnemingen van ijsoppervlakverplaatsing die zijn verkregen door optische beeldgegevens, een waardevol inzicht geeft in de gletsjerdynamiek in het Nyainqêntanglha gebied.

Hoofdstuk 5, vervolgens, schat de mogelijke temporele patronen van het glaciële oppervlakkenverplaatsingsrespons binnen het Nyainqêntanglha gebied met het lokale klimaat. In dit onderzoek is het lokale klimaat gekarakteriseerd door gebruik van TRMM-neerslag en de MODIS dataproducten met landoppervlaktemperatuur, terwijl de lokale gletsjerrespons op het regionale klimaat is gekarakteriseerd door de periodieke, lineaire trend en amplitude van het periodieke onderdeel van gletsjeroppervlaktestroom. De analyse van de maandelijks neerslag en landoppervlaktetemperatuur resulteerde in het bepalen van seizoenen zoals ze voorkomen op het Tibetaanse plateau. Belangrijkste voor de gletsjersbalans is het zomermoessonseizoen, wanneer zowel hoge neerslag als hoge oppervlaktetemperaturen voorkomen. De statistische afhankelijkheid van ijsstroom op neerslag en temperatuur werd geschat door middel van multi-regressie analyse. In overeenstemming met de interactie tussen het regionale klimaat (neerslag en temperatuur) en gletsjers werden de lineaire trend en amplitude van het periodieke component van de tijdsreeksen met gletsjeroppervlakverplaatsingen berekend met behulp van FFT-analyse gecombineerd met de kleinste-kwadraten oplossing. Met behulp van de toepassing van FFT-analyse en kleinste-kwadraten oplossing op regionale klimaatverandering (neerslag en temperatuur) en ijsstroom in termen van de tijdseries van oppervlakverplaatsing, worden de temporele patronen van ijsstroom geschat. Het geeft aan dat het mate van ijsstroom gerelateerd is aan de patronen van de zelfaanpassing van de gletsjer geïnduceerd door regionale klimaatverandering (temperatuur en neerslag). Deze bevindingen impliceren dat de feature-tracking methode met observaties van satellieten in staat is om tijdsreeksen van ijsstromen over grote tijdsspanne te verkrijgen en de interacties met regionale klimaatvariabelen in deze regio te schatten.



Acknowledgments

During my PhD journey, I received the careful guidance of my promoter, help from my colleagues and friends, and support from my family. All of them accompany me to experience numerous memorized moments in the Netherlands. Here, I would like to express my sincere appreciation to all of them.

First of all, my greatest gratitude goes to my promoter Prof. Massimo Menenti. He provided the opportunity which brought me from Hohai University to Delft University of Technology to start my PhD research. I was impressed by his experience and knowledge on different topics in the remote sensing field. One of the most significant moments was our first research meeting when I arrived at Delft. I was inspired to explore how to apply remote sensing techniques on the glaciology in my PhD research. He not only gave me the good supervision through my research, but I also benefited greatly from his support beyond the work. Massimo's education philosophy were valued for me in these past years, and will shape my future career. At the same time, I am grateful to my copromoter Dr. Roderik Lindenbergh who advises me a lot on my daily work. It helps me to improve many technical details and gives a lot of important clues to solve problems in many practical cases.

I would like to express my appreciation to Prof. Ramon Hanssen who was one of committee members as well. When I talked to him, he suggested me to consider different visions and angles for different problems. By his encouragement, I gained a lot of constructive concepts and methodology through discussing with the colleagues in the relevant fields of our department. Sincere thanks also go to Bob Su, Stef Lhermitte, Pier Siebesma and Liliang Ren for taking place in my PhD committee and providing valued reviews on the manuscript of this thesis.

It is my luck to be accompanied by a great group of colleagues Ben Gorte, Miren Vizcaino, Conelis Slobbe, Lorenzo Iannini, Ramses Moljin, Marcel Kleinerbrink, Seyed Enayat Hosseini Aria and others at the Department of Geoscience and Remote Sensing, TU Delft. I wish to thank Lidwien de Jong, Debbie Rietdijk, and Irma Zomerdijk for all the kind administrative support during my PhD. My officemates Yerong Wu, Yu Sun are acknowledged for creating nice working atmosphere. A great appreciation goes to my Chinese friends and colleagues Ling Chang, Jiangjun Ran and Haolv Shang, Jinhu Wang, Mengshi Yang, Zhou Kaixuan, Yueqian Shen and Jie Zhou for offering invaluable friendship and support along my study. In particular, I thank the helps and discussions from

Ling Chang, Jiangjun Ran and Haolv Shang on methodology and time series analysis.

Thank you to my friends, Mingliang Li, Hua Zhong, Yutian Yao, Jia Wan, Jianing Wang, Jiao Yuan, Hao Chen, Wenchao Wang, Xuefei Mei, Lu Wang and the guys of DCF etc. I will keep the fantastic and enjoyable time with all of you in mind.

And I would like to express appreciation to my supervisor Prof. Liliang Ren when I studied in Hohai University. The study and training in Hohai University gave a good basis and preparation for my PhD study. Your continuing enthusiasm and patience always impressed me in my study.

Last but not least, I sincerely thank my family for their unconditional and endless love and support.

Junchao Shi
Delft, May 2017

1

Introduction

The state of glaciers on the Earth is recognized as a good indicator of the changing climate. Approximately, ~70% global freshwater is blocked within the glaciers on the continental surface. Glaciers remained on the Tibetan Plateau are one of the main reservoirs of water that benefit the people living around several major Asian rivers downstream. The high elevation and morphology of the Tibetan Plateau (TP over 4000 m), influence the regional atmosphere circulations i.e. the westerlies from inland of Eurasia and monsoons from Indian and East Asia. The land surface energy balance determines heating of the atmosphere at high elevation across a range of spatial and temporal scales resulting in a highly variable radiative and convective forcing. The latter does also apply to glaciers, with impacts on the mass balance of glaciers in the Tibetan Plateau. However, the understanding of the interactions between atmosphere and Tibetan glaciers still needs to be improved further.

1.1. Tibetan Plateau (TP)

The most elevated plateau in the world, the Tibetan Plateau is located in the southwestern part of China, central Asia. It stretches over $\sim 2.5 \times 10^6$ km² between the Taklamakan Desert and the Himalaya Mountains, over $\sim 20^\circ$ longitude (78°25'E \sim 99°06'E) and $\sim 10^\circ$ latitude (26°44'N \sim 36°32'N). This high elevation results in two distinct phenomenon, i.e. a reduced air mass overlaying on the Tibetan Plateau than its surroundings and surface of the plateau can be warmed up more efficiently in this region. It has been found that the larger scale atmosphere-ocean interactions effect is linking with the thermodynamic process over the TP [148].

As a large glaciated area besides Antarctica and Arctic/Greenland, the moun-

tain glaciers occupy about 1.0×10^5 km² on the Tibetan Plateau. However, their mass changes remain poorly known, including their contributions to global sea level variations [71, 155]. Recent studies indicate that new evidence has been gathered on local climate changes, particularly on the effect of the atmosphere circulations and hydrological cycles modifications on Tibetan glaciers.

The TP's warming starts from the early of 1950s, which is earlier than the Northern Hemisphere's (mid-1970s). There is an increasing trend in surface air temperature and humidity, and decreasing trend in irradiance and wind speed since the 1980s [41, 61, 112]. The TP warming has also temporal variability associated with surrounding thermal and mechanical processes, and the timing of regional atmospheric circulations. For instance, the warming rate behaves differently at the year scale [111],

1. The maximum of warming rate occurs in the autumn;
2. The yearly warming rate is only half of the winter's warming rate;
3. The warming rate in spring and summer increase significantly.

Surface properties (i.e. elevation) modulate the process of TP's warming and its spatial patterns [107]. Using the historical meteorological and satellite data, some studies show that the TP warming relies on elevation differences [107, 149].

1.2. Regional Climate

Due to the high elevation and other geoenvironmental conditions, the Tibetan Plateau influences the atmosphere circulation of the Northern Hemisphere [161]. Atmospheric scientists have been exploring the regional climate of the plateau and its tempo-spatial variability for a long time [20, 30].

One of the concerns is that the proposed asymmetry of atmospheric circulation is related to the midlatitude westerlies from inland. Air flow is partly over the Tibetan Plateau and partly around it. The interplay of westerlies and monsoon climate is regarded as one of the primary determinants of the regime of Plateau climate [22, 90].

The other concern is the interaction between the Plateau thermal effects on the atmosphere and Asia climate [41, 42, 138]. Previous studies suggest that the middle troposphere is heated by the surface heat fluxes during the summer season, while surface cooling occurs in the winter [156, 157]. Furthermore, the land-ocean thermal contrast and the convection in the troposphere are controlled by the seasonal surface heating source and its spatial variability over the Tibetan Plateau. This process affects the Asian monsoon and onset of the Asian and Indian monsoons can be delayed or advanced [41, 144, 161].

1.2.1. Warming influence

More frequent seasonal warming has been observed on some high elevation regions, such as the TP (Tibetan Plateau) and the Tropical Andes [111]. The TP is the most sensitive to climate adjustments and experiencing temperature increasing from last century [15, 149]. In particular, observations suggest that the increment of the temperature is about 1.8 °C over the past 50 years on the TP. Alternatively, the warming and moistening trend with a warming rate of 0.36 °C per decade (1961-2007) was observed on the plateau compared with a global average of this warming rate, only 0.13 °C per decade over the last 50 years [88, 138].

The land and atmosphere energy budgets (sensible flux and latent flux and so on) are the main drivers of the warming over the Tibetan Plateau. The influence of this warming trend can be categorized at different spatial scales.

1. Local scale: influence on glacier changes

At local scale, the warming of TP has a direct influence on mountain glacier shrinking and melting [138, 149]. It has been found that 82% of the mountain glaciers have retreated or declined with the increasing temperature on the TP [88].

Mechanically, surface energy budgets play a significant role in the heating of TP and influence the snow/ice albedo feedback [161]. The more sensible flux is transferred upwards to the Atmosphere Boundary Layer (ABL), the higher precipitation due to the destabilized the atmosphere and developed convection [138].

Surface properties have a larger influence on the surface energy. In the summer season, the lower snow cover gives a much lower albedo and much higher net radiation, with higher surface temperatures [157, 161]. Moreover, a smaller fraction of net radiation in summer is consumed by melting of snow and ice than in the winter season [123, 124]. In numerical experiment, [138] and [161] also evaluated that the warming/cooling effect of the plateau in relation with increasing surface albedo.

2. Larger scale: relation with monsoons

At larger scales, the warming gradient from West to East of TP is only a local phenomena, but also associated with atmosphere circulations, i.e. the Indian and East Asian monsoons [85, 119, 139]. The surface warming and strengthened land-ocean thermal contrast have impacted the development of monsoon precipitation. The changing differences of thermal status and contrast between ocean and southern and eastern of the TP have been linked with the inter-annual fluctuations in the Asian Summer Monsoon [88]. Based on historical meteorological data, the northern plateau became warmer, and in the southern more humid from 1984 to 2006 [149]. It could indicate that the decreasing surface heating and atmosphere heating over the TP have changed the monsoon precipitation. Moreover, it is found that sensible heat and the total heat source decreased since

the 1980s. Total heating source peaks in July, while heating is stronger in the eastern TP than in the western TP. The Asian summer monsoon is strengthened by the atmosphere heating of the TP [148]. The seasonal development and onset of Asian monsoon over the Tibetan Plateau is inversely related to the intensity of the interaction between westerlies and the jet stream over the Asian-Pacific region [161].

1.2.2. Precipitation

The Asian summer monsoon, characterized by the South-Westerlies and Southerlies, supplies considerable moisture and determines the regional precipitation [38]. As described in the previous section, the thermal contrast between land and ocean dominates the occurrence of the Asian monsoon. In combination with Westerlies from inner Eurasia, the spatial variability of precipitation can be strengthened by warmer temperatures [131, 148]. Based on the reanalysis and in situ measurements, it is found that the precipitation is increased almost over the entire Tibetan Plateau from 1961 to 2001, even though some diverse subregional patterns have been noted, such as in the eastern part (dramatically increasing) and in the western part (decreasing). Moreover, the seasonal precipitation belt associated with this summer monsoon is supposed to vary at intraseasonal, interannual, and interdecadal time scales. Then, the timing of precipitation may correlate to the atmosphere circulation over the Pacific and Indian Ocean in terms of sea surface temperature and the changing snow cover over Eurasia [59, 145]. The combined analysis of multiple datasets, i.e. 97 meteorology stations and two integrated satellite datasets (CMAP and CPCP) suggested that the Tibetan Plateau is a moisture sink with limited net moisture convergence in summer [149, 161].

1.3. Response of glaciers to climate change

Climate variability result in the variations of radiation, temperature and precipitation so that the corresponding adjustment of geometry take place on the glacier. As described in the previous sections, the Tibetan Plateau is the main heating source and moisture sink within the regional climate system seasonally. Specifically, energy reaches the glacier surface not only as short and long wave radiation fluxes, but also by convection of latent and sensible heat fluxes. Theoretically, the larger the energy received by the glaciers, the larger the glaciers melt. Nevertheless, the refreezing processes, albedo variability due to the debris, topography of the surface will have an impact on the melting of the glaciers at the micro-scales. The glacier mass balance is driven primarily by melting, sublimation (ablation process) and snowfall (accumulation process). Due to the development of remote sensing observation and numerical atmospheric studies,

strong interannual variations in snow accumulation on the Tibetan Plateau have been documented [161]. The timing of snowfall and the evolution of temperature determine glacier regime, particular in areas dominated by the summer monsoon, i.e. where accumulation and ablation peak at the same time. Locally, the interplay of relief -driven winds and the surface energy balance may have an important role in determining spatial variability of accumulation and ablation.

1.4. Roadmap of this dissertation

1.4.1. Research questions

This study addresses the following research questions:

1. Is it feasible to retrieve surface properties from satellite laser altimetry data over the Tibetan Plateau?
2. How should glacier surface displacement and ice velocity of Tibetan glaciers be estimated?
3. Does glacier surface displacement of Tibetan glaciers respond to climate variability?

1.4.2. Organization of the dissertation

The comprehension on the physical relationship between glaciers and regional climate is essential to project the response of Tibetan glaciers on the potential global climate change. The surface process of these glaciers are considered as a significant interface between atmospheric boundary layer and the glacier surface. According to previous sections, both energy and moisture (mass) exchanges occur on this interface, affecting the glaciers own dynamics. Normally, the accumulation and ablation process develop in different seasons on the glaciers, such as, continental and temperate glaciers. The unique geolocation, regime of heat and moisture transported by the dominant winds over parts of the Tibetan Plateau makes the study of glacier surface process more challenging. In recent decades, several modeling and experimental researches have been initiated on the various Tibetan glaciers [5, 16, 47, 49, 96]. The glaciers over the Nyainqêntanglha Range are assessed to accumulate and ablate simultaneously, due to the interaction between westernlies and summer monsoons. Nevertheless, the specific characteristics of the mass and energy balance on these glaciers are still not well understood. In this thesis, as a part of the CEOP-AEGIS (Coordinated Asia-European long-term Observation system of Tibetan Plateau hydro-meteorological processes and the Asian-monsoon systEm with Ground satellite Image data and numerical Simulations) project, the glaciated zone over the Nyainqêntanglha Range located close to the Nam Co Lake was chosen as the study area. Here, the glacier surface roughness, and displacements are chosen

as key surface features to be studied [48, 113].

- Chapter 2 the main background is described, including the status of Tibetan glaciers, a summary on the Nyainqêntanglha Range, the general regime of glacial surface and previous measurements related to glacial surface processes on this range.
- Chapter 3 presents the potential parameterization of surface roughness using spaceborne laser altimetry data.
- Chapter 4 shows the derivation of glacial surface displacements combining the feature-tracking methods with optical imageries.
- Chapter 5 further estimates the possible temporal patterns of the glacial surface displacements response to the regional climate within the Nyainqêntanglha Range.
- The conclusion and recommendations are summarized in the Chapter 6.

2

Background

The high altitude of the Tibetan Plateau enhances the influence of monsoon climate from East Asia and Indian Ocean, when mitigating the influence of the mid-latitude westerlies [21, 152]. The glaciers on the Tibetan Plateau not only supply a considerable fraction of the water of several Asian large rivers, but also contribute to the global sea level rise (SLR) due to the widespread negative mass balance on the plateau [18]. Numerous investigations have been dedicated to many aspects of glaciers state and evolution, such as determining area and length statistics, topography mapping and boundary delineation, volume/mass change estimates, as well as meteorological observations and estimates of the energy balance at the surface [38, 39]. Recent studies estimate the remaining extent of glaciers at 100,000 km² over the entire plateau including ~ 40,000 km² in India, Pakistan and ~ 59,000 km² in China [122, 155].

In this chapter, the general state of glaciers on the Tibetan Plateau is described firstly. Then, the review focuses on a specific study area, the Nyainqêntanglha Range, the geoenvironmental situation and its role in the regional climate changes. Processes in the mountain glaciers characteristics this area will be briefly introduced to explain the linkage between the surface process determining the energy balance and glacier flow.

2.1. Glaciers on the Tibetan Plateau

Numerous glaciers are distributed in the mountain ranges of Central Asia, such as Tien Shan, Pamirs, Karakoram, Kunlun, Nyainqêntanglha and Himalaya in Western China. According to the thermal regime of the glacier, climatology and some previous investigations, these mountain glaciers were categorized into different types: sub-continental, temperate and extreme continental [121, 122] ini-

tially. Many recent remote sensing studies e.g. by Lidar, optical imaging, gravimetry in combination with numerical modeling of glacier dynamics improved the understanding for thermal regime of Tibetan glaciers and their response to climate forcing [38]. These studies suggest that glacier energy and mass balance are influential by the local topography and atmospheric conditions. This leads to the definition of inhomogeneous zones in the response of Tibetan glaciers to climate: Seven zones are identified: Northeast, Northwest, two zones in the Central Plateau and three in the Himalayas. Re-arranging these zones along three transects are: 1) Southwest-Northeast oriented; 2) Southeast-Northwest oriented and 3) along the Himalayas. These transects are evident with the weakening of monsoons and strengthening of westerlies from south part of the plateau to the interiors. Specifically, the Himalayan glaciers seem to be reduced in terms of the length and area recently. Some investigated glaciers in the southeastern part of the plateau shrank more extremely than others with the average recessed length of 48.2 m/yr as well as the recessed area of 0.57%/yr, 1970s-2000s. However, the decreasing trend has been diminished to the interior of the plateau gradually. The tiny rate of recession is about 0.9 m/yr (length) and 0.07%/yr (area) detected in the eastern Pamir [155].

2.2. Mass balance

A glacier can be divided into two parts: accumulation zone (higher elevation) and ablation zone (lower elevation). The net accumulation is dominant in the accumulation zone where the mass gain (i.e. snow fall) exceeds the mass loss (i.e. melting process). Conversely, the net ablation is more significant in the ablation zone coupling the gravitational force of ice body to drive the glacier deformation and movement. The general pattern of flow in a glacier is determined by the net mass balance. We define b_s as the specific summer mass balance, b_w as the specific winter balance, and b_n as the specific net balance [60],

$$b_n = b_s + b_w \quad (2.1)$$

Mountain glaciers can be growing or shrinking in response to the combined influence of the accumulation and ablation over a period of time. The item, glacier mass balance, is used to estimate the temporal variation of the glacier. The mass balance varies in the course of time, while a glacier reaches a new equilibrium under climatic conditions [4, 165].

Snow accumulation occurs at the glacier surface, with depletion occurring by melting, sublimation, or redistributed by air flow, i.e. by surface processes [60, 100]. Glacier flow is determined by gravitational sliding coupling internal deformation. Understanding glacier response to climate forcing requires modeling

glacier flow in combination with observations of key-properties such as surface roughness and surface velocity [102, 108, 129]. And the retrieval of these properties by satellite data sets provides a potential way for applications over large spatial coverage and long term monitoring [33, 105, 117].

2.3. Surface process

2.3.1. Surface mass balance

As described above, glacier mass balance is a changing complex process coupling certain climatic conditions. In other words, the glacier surface process is dominant where the surface topography evolves by interaction between underlying ice body and overlying atmosphere boundary layer, in terms of thermodynamics, hydrology and mass/ energy exchange at the glacier surface [142].

Surface mass balance (SMB) refers to increasing or decreasing mass at the glacier surface. The general form of SMB at any location of glacier surface can be expressed as below [32],

$$SMB = PR - RU - SU_s - SU_{ds} - ER_{ds} \quad (2.2)$$

where PR is total precipitation (including both solid and liquid forms), RU refers to meltwater runoff, SU_s is surface sublimation and the last two terms represent sublimation (SU_{ds}) of drifting snow and erosion (ER_{ds}) by drifting snow, respectively. SMB is usually expressed in units of mm w.e.yr^{-1} or $\text{kg m}^2 \text{ yr}^{-1}$, the same units that are used to express precipitation in meteorology [81].

2.3.2. Surface energy balance

The glacier-atmosphere interaction refers to the exchanges of momentum, heat and mass between the glacier surface and overlying atmosphere boundary layer (ABL). As the main interface of a glacier with atmosphere boundary layer, the glacier surface, plays a significant role in the energy and moisture exchange of the glaciers. The surface energy balance on each location on the glacier surface is coupled within atmosphere boundary layer dynamics and modulated by surface albedo and aerodynamic roughness.

Most of mountain glaciers remains in the broad, high elevated area on the Tibetan Plateau. The influence of arid, and cold air flows, katabatic winds, sometimes dominate the local climate of glaciated mountain region. Thus, both mass and energy distribution of the glaciers can be regulated by the various air flow in the forms of snow drifting and heat transportation.

According to equation 2.1, b_w includes precipitation and drifting alone when ignoring mass increment by condensation and avalanching. Similarly, the b_s is considered as a function of surface melt, neglecting the evaporation, bottom pro-

cess and so on, while the energy involved in these phase change processes is taken into account. The surface energy fluxes [151] can be formulated directly as flows

2

$$SEB = S_{in} + S_{out} + L_{in} + L_{out} + H + LE + G \quad (2.3)$$

where S_{in} , S_{out} represent the incoming and reflected shortwave radiance, respectively; L_{in} , and L_{out} are the incoming and outgoing longwave radiance, respectively. H and LE are the turbulent fluxes of sensible heat and latent heat fluxes, respectively; and G is the subsurface heat flux. All fluxes are defined to be positive when directed toward the surface.

Alternatively, the net radiation flux can be derived from the surface energy balance equation 2.3,

$$R_n = H + LE + G \quad (2.4)$$

where R_n is the net radiation flux, including S_{in} , S_{out} , L_{in} , and L_{out} .

2.4. Surface roughness

2.4.1. Influence on surface energy balance

As described in the previous section, glaciers and atmospheric boundary layer interact through the glacier surface to exchange momentum heat and relevant moisture. Such processes are characterized by large spatial and temporal variability of atmosphere [98, 101]. The glacier surface energy fluxes, including net radiation flux R_n , sensible heat flux H , and latent heat flux LE etc., need to be parameterized using observable glacier surface properties such as surface temperature, albedo, emissivity, surface roughness and so forth.

In high elevated region, glaciers are located in the irregular and rugged topography. The local rugged topography and glacier surface irregularity can modulate the atmosphere boundary layer flows and in turn the relevant momentum and heat fluxes through force drag (shear stress and form drag). For mountain glaciers, turbulent heat fluxes including sensible flux H and latent flux LE are considered to be important sources of glacier surface melt.

Based on Monin-Obukhov similarity theory, several methods have been developed to estimate turbulent fluxes by using the logarithmic wind profile and other glacio - meteorological parameters [34, 36]. Some previous studies indicate that the determination of turbulent fluxes still constitutes a major uncertainty in the surface energy balance, while the parameterization of surface roughness parameters are influential on the turbulent heat fluxes [35, 151].

Following the bulk aerodynamic approach and implementing the stability

correction [103], the turbulent fluxes are computed as

$$H = \rho_a \frac{C_p k^2 u (T - T_s)}{(\ln z / \ln z_{0m})(\ln z / \ln z_{0T})} (\Theta_m \Theta_v)^{-1} \quad (2.5)$$

$$LE = \rho_a \frac{L_s k^2 u (q - q_s)}{(\ln z / \ln z_{0m})(\ln z / \ln z_{0q})} (\Theta_m \Theta_v)^{-1} \quad (2.6)$$

where ρ_a and C_p refers to the density and specific heat capacity of air, respectively. L_s is latent heat of sublimation of snow or ice, and κ is the von Karman constant. τ is surface stress and u^* is the friction velocity. z_{0m} is the surface roughness parameter for momentum; z_{0T} and z_{0q} are the surface roughness parameters for temperature and humidity, respectively. To compute turbulent fluxes (equations 2.5 and 2.6), it is assumed that the air temperature is equal to the surface temperature of the snow/ice at z_{0T} and that the air is saturated with respect to the surface temperature of the snow/ice at z_{0q} . This last assumption helps calculate surface specific humidity q_s .

The nondimensional stability functions for momentum (Θ_m), heat (Θ_h) and moisture (Θ_v) can be expressed in terms of Ri_b [127]:

$$Ri_b = \frac{g(T - T_s)(z - z_{0m})}{Tu^2} \quad (2.7)$$

where T and u are mean values of air temperature and horizontal wind speed at the level of measurement z , respectively. The parameter g is acceleration of gravity. Assuming that local gradients of mean horizontal wind speed u , mean temperature T and mean specific humidity q are equal to the finite differences between the level of measurement and the surface.

$$(\Theta_m \Theta_v)^{-1} = (\Theta_m \Theta_h)^{-1} = (1 - 5Ri_b)^2, \quad (2.8)$$

when Ri_b is positive (stable)

$$(\Theta_m \Theta_v)^{-1} = (\Theta_m \Theta_h)^{-1} = (1 - 16Ri_b)^{0.75} \quad (2.9)$$

when Ri_b is negative (unstable)

Moreover, it is found that z_{0T} and z_{0q} can be derived by using the ratio between z_{0T}/z_{0m} and z_{0q}/z_{0m} , which are expressed in terms of the polynomials of Reynolds number Re_* on the glaciated area:

$$\ln(z_{0T}/z_{0m}) = b_0 + b_1 \ln(Re_*) + b_2 (\ln(Re_*))^2 \quad (2.10)$$

where $b_{0,1,2}$ refer to the polynomial coefficients determined by the aerodynamic flow regime.

$$\ln(z_{0q}/z_{0m}) = b'_0 + b'_1 \ln(Re_*) + b'_2 (\ln(Re_*))^2 \quad (2.11)$$

where $b'_{0,1,2}$ refer to the polynomial coefficients determined by the aerodynamic flow regime.

2

2.4.2. Development of surface roughness parameterization

Surface aerodynamic roughness is defined by the logarithmic vertical profile of mean horizontal wind speed. i.e. it requires measurements of wind speed at different heights over sufficiently long period of time. Moreover, when dealing with large and heterogeneous landscapes, it becomes very challenging to capture the spatial variability of surface aerodynamic roughness using such measurements. The z_0m can not be derived easily when using wind profile measurements, since the logarithmic vertical profile only applies when the surface atmospheric layer is in dynamic equilibrium with the land surface. The rugged topography at most glacier locations further adds to the challenge of determining an effective aerodynamic roughness z_{0m}^{eff} accounting for the topography influence. Even over the flat terrain the effective aerodynamic roughness is determined by the dimensions, and density distribution of obstacles. Determining the aerodynamic roughness of glacier is as complex as in any inhomogeneous landscape, requiring a detailed characterization of the glacier surface to estimate the surface aerodynamic roughness [6, 9]. The challenge, therefore, is to parameterize the surface aerodynamic roughness as a function of observable geo-spatial variables. Airborne laser scanning provides the detailed measurements required to derive surface geometry at the level of detail and accuracy required to determine the surface aerodynamic roughness [37, 128]. The remote sensing approach (i.e. laser measurements) can be used to determine the geometric properties of territorial landscapes required to estimate the surface aerodynamic roughness, as done first by [94]. It estimates the effective aerodynamic roughness considering remote sensing derived land surface geometrical parameters. In particular, the geometric roughness of surface is the key to treat form drag during the calculation. Compared to conventional techniques (i.e. bulk similarity technique based on wind profile dataset), the remote sensing approach derived measurements are potential to improve the resolution of measurements spatio-temporally.

2.5. Glacier motion

The evolution of the glacier shape is governed by ice flow and mass fluxes at the glacier boundary. The gravitational force and internal deformation control the ice flow downwards [66]. The knowledge of glacier flow field is essential for understanding the response of glaciers to climate forcing, since the ice velocity pattern is a measure of glacier mass imbalance between accumulation and ablation [69]. Such imbalance leads to the redistribution of mass. Since a significant

driver of the imbalance is the pattern in the glacier surface energy balance, surface heat fluxes, surface temperature and surface flow velocity are interrelated, as explained briefly in this section [32].

For the reasons below only generalized formulations are considered here to discuss the relevant energy balance and ice velocity:

Firstly, boundary conditions including the irregularity of surface and bottom, and variability of temperature and its gradient;

Secondly, the advection of heat and temperature distribution is affected by ice flow;

Thirdly, the potential three dimensional problem by i.e. the extension to the flowline and so forth.

All these sorts of issues result in the difficulty of analytical full solutions to be derived from the generalized formulations.

When taking into account heat conduction and heat advection by ice flow, the generalized energy balance of an ice volume can be expressed as [60]:

$$\frac{\partial \theta}{\partial t} = \underbrace{\kappa \left[\frac{\partial^2 \theta}{\partial x^2} + \frac{\partial^2 \theta}{\partial y^2} + \frac{\partial^2 \theta}{\partial z^2} \right]}_{\text{conduction}} + \frac{1}{\rho C} \left[\frac{\partial K}{\partial x} \frac{\partial \theta}{\partial x} + \frac{\partial K}{\partial y} \frac{\partial \theta}{\partial y} + \frac{\partial K}{\partial z} \frac{\partial \theta}{\partial z} \right] - \underbrace{\left[u_x \frac{\partial \theta}{\partial x} + u_y \frac{\partial \theta}{\partial y} + u_z \frac{\partial \theta}{\partial z} \right]}_{\text{advection}} + \underbrace{\frac{Q}{\rho C}}_{\text{strain heating}} \quad (2.12)$$

For convenience, this generalized energy balance equation 2.13 can be simplified as

$$\frac{\partial \theta}{\partial t} = \kappa \nabla^2 \theta + \frac{1}{\rho C} \nabla K \cdot \nabla \theta - \mathbf{\bar{u}} \cdot \nabla \theta + \frac{Q}{\rho C} \quad (2.13)$$

by using the operators,

$$\nabla = \frac{\partial}{\partial x} \hat{i} + \frac{\partial}{\partial y} \hat{j} + \frac{\partial}{\partial z} \hat{k} \quad (2.14)$$

where

θ —the temperature of ice

ρ —the density of ice

C —the heat capacity of or specific heat

K —the thermal conductivity of ice

$\kappa = K/\rho C$ —the thermal diffusivity of ice

Q —the heat production

t —time

$\hat{i}, \hat{j}, \hat{k}$ —are unit vectors in the x, y, z directions, respectively

$\vec{u} = u_x \hat{i} + u_y \hat{j} + u_z \hat{k}$ —the vector velocity

2.6. Nyainqêntanglha Range

2.6.1. Geo-environment

This study focuses on the Nyainqêntanglha Range nearby Nam Co Lake (located at $90^{\circ}16' \sim 91^{\circ}03' \text{E}$, $30^{\circ}30' \sim 30^{\circ}55' \text{N}$). Previous studies have shown that the variations of the lake water level and volume on the Tibetan Plateau are driven by temperature, rainfall, humidity and solar radiation [141]. Since 1970s, the Nam Co Lake has been considered as one of the indicators on the regional climate change. In 2005, the Institute of Tibetan Plateau Research, Chinese Academy of Science, set up the Nam Co Lake Multi-Layer Comprehensive Observation and Research Station (Nam Co Station). This has mitigated considerably the scarcity of meteorological observations in the lake basin, regular monitoring of necessary meteorological parameters within this area.

According to the historical and latest in situ observations, the general warming trend is found and coincident with the local annual mean temperature, at a rate of $0.404 \text{ }^{\circ}\text{C}/10 \text{ a}$ from 1976 to 2009. The elevation in the basin ranges from 4718 m (lake area) to 5500 m (the average on the Nyainqêntanglha Range). It results in more solar radiation absorbed within the Nam Co Lake region around 2900-3200 h/a. Melting water from the glaciers in the Nyainqêntanglha Range flows into the Nam Co Lake (lake area: $\sim 1,920 \text{ km}^2$ in 1979) and other main rivers (e.g. Yarlung Tsangpo, and Nu River). Until 2009, the water storage has been increasing to $870.30 \times 10^8 \text{ m}^3$, with the tendency of $2.67 \times 10^8 \text{ m}^3$; the lake area enlarged to 2015.12 km^2 in the period of 1976-2009 [162]. An summary on the evolution of lake area and lake volume in Table 2.1.

As a highly elevated inland lake on the Tibetan Plateau, the water storage of Nam Co Lake relies on the several sources: precipitation (both liquid and solid forms), surface flow, subsurface flow. Recent studies indicate that the glacial meltwater as well as precipitation are two main inputs for increment of the lake

Table 2.1: Variations of lake water storage and surface area in different periods. A_b , A_e , V_b , V_e represent the lake area and water storage in the beginning and ending of each period. This table is based on the investigation of lake water changes by [162].

| Period | Lake surface area (km ²) | | | Water storage (10 ⁸ m ³) | | |
|-----------|--------------------------------------|---------|-------------------------------|---|--------|--|
| | A_b | A_e | Tendency (km ² /a) | V_b | V_e | Tendency (10 ⁸ m ³ /a) |
| 1976-1999 | 1972.48 | 1968.23 | 5.35 | 786.06 | 824.35 | 1.59 |
| 1999-2006 | 1968.23 | 2015.12 | 6.67 | 824.35 | 866.97 | 6.41 |
| 2006-2009 | 2015.12 | 2015.35 | 0.76 | 866.97 | 870.30 | 1.63 |

water storage [80, 140]. The evident increasing of temperature (1% significant level), precipitations (10% significant level), and reduction of evaporation can explain the positive trend in lake area and volume [162].

2.6.2. Established in situ measurement

Numerous studies document the increasing of change of Tibetan glaciers during recent decades, although the overall picture for the entire Tibetan Plateau is far from comprehensive. Ding et al. [39], Li et al. [86] and Yao et al. [153] suggest on the basis of in-situ glaciological investigations that glacier length, width, area and ice mass are decreasing over the Tibetan Plateau. For instance, Pieczonka et al. [105] found ice mass is decreasing by using Multi-temporal digital terrain models (DTMs) in 12 glaciers, Central Tien Shan. The thickness of these glaciers has been decreased 18.7 ± 5.6 m in their ablation zones from 1976 to 2009. The total mass loss converted from the decrease in surface elevation was about 0.33 ± 0.15 m w.e.a⁻¹ between 1976 and 2009. The loss in two largest glaciers, Koxkar and West Qongterang, is about 0.27 ± 0.15 m w.e.a⁻¹ and 0.43 ± 0.15 m w.e.a⁻¹ over this period, respectively. Similarly, a mass loss of glaciers was observed in the Himalaya region [71]. Contrariwise, an anomalous gain of mass has been estimated in the Karakoram glaciers [50, 134]. Scherler et al. [116] also found that the Himalayan glaciers respond to the regional climate change but with some noticeable spatial variability. The monsoon-influenced glaciers (i.e. Himalaya) has been shrinking, while the westerlies-influenced glaciers are advancing or stable in the Karakoram. Therefore, more observations and a better understanding of the relationship between glaciers and regional climate is necessary when assessing the responses of Tibetan glaciers to global climate [97, 155].

In particular, the glaciers in the Nyainqêntanglha Range, within the transitional area from monsoon to westerlies dominated climate, has received much

attention since recent years. These glaciers are located in the rough, high elevation of the Nyainqêntanglha Range, whose are higher than ~5000 m in most parts. Those glaciers are affected by the charge of coupling between continental climate from Central Asia and summer monsoons from oceans. Glaciers in this region were delineated using in combination with the 1970s topographic maps, DTMs and satellite images, providing a good reference to determine the variation of the Nyainqêntanglhan glaciers [72, 153, 163].

A glacier inventory includes the geometric and glaciological information on each individual glacier. To clarify the recent state of mountain glaciers in the Nyainqêntanglha Range, the new glacier inventory is updated by using multiple temporal and spectral satellite data, such as, Hexagon KH-9 and Landsat MSS (both 1976), Metric Camera (1984), and Landsat TM/ETM+ (1991, 2001, 2005, 2009) combining with previous inventory dataset. Data records on some related glacial parameters, e.g. minimum, maximum, median elevation, slope, aspect, area, were reconstructed through this study [19]. The results show that there are still ~1000 glaciers covering an area of ~800 km², including ~15% on the northern side of the ridge and ~85% on the southern side of the Nyainqêntanglha Range. Shrinkage of these glaciers have been detected, in particular, 42 km² of ice cover recessed in the south-western area from 1976 to 2001. The shrinkage rate of these glaciers during the period 2001-2009, was larger than the value in 1976-2001. Interestingly, the smaller and lower elevated glaciers seem to contribute to diminishing of the total glacier area over the range. Statistically, the state of these glaciers within the higher than 6000 m area is rather stable and their area almost consistent. Intensive recession of area diminishing occurred between 5500 m and 5700 m altitudes.

Six meteorological stations are located around the Nyainqêntanglha Range and Nam Co Lake basin, three of them (Xainza, Baingoin, and Nagqu) in the Northern part, the others (Xigaze, Lhasa, and Damxung) are in the Southern part and were installed by the Climatic Data Center, National Meteorological Information Center, China Meteorological Administration. The meteorological data, such air temperature, precipitation, are prepared for essential basic information on glacier energy and mass balance estimates from 1950s to 2000s.

Table 2.2: The change of glacier area over the Nyainqêntanglha Range and Nam Co Basin from 1976 to 2009. This table is based on the glacial investigation by [19].

| | Area (km ²) | | | 1976-2001 | | | 2001-2009 | | | 1976-2009 | | |
|----------------|----------------------------|-------------|-------------|----------------------------------|-------------------|----------------------|----------------------------------|-------------------|----------------------|----------------------------------|-------------------|----------------------|
| | 1976 (km ²) | 2001 (%) | 2009 (%) | Δa (km ²) | Δa (%) | $\Delta a/yr$ (%) | Δa (km ²) | Δa (%) | $\Delta a/yr$ (%) | Δa (km ²) | Δa (%) | $\Delta a/yr$ (%) |
| South | 734.1 | 692.4 | n.a. | -41.7 | -5.7 | -0.23 | n.a. | n.a. | n.a. | n.a. | n.a. | n.a. |
| Western | ± | ± | | ± | ± | ± | | | | | | |
| Region | 25.7 | 19.4 | | 22.4 | 3.1 | 0.12 | | | | | | |
| Nam Co | 212.5 | 198.1 | n.a. | -14.4 | -6.8 | -0.27 | n.a. | n.a. | n.a. | n.a. | n.a. | n.a. |
| Drainage | ± | ± | | ± | ± | ± | | | | | | |
| Basin | 7.4 | 5.5 | | 6.5 | 3.1 | 0.12 | | | | | | |
| Glaciers | 504.8 | 475.3 | n.a. | -29.5 | -5.8 | -0.23 | n.a. | n.a. | n.a. | n.a. | n.a. | n.a. |
| southeast of | ± | ± | | ± | ± | ± | | | | | | |
| the main ridge | 17.7 | 13.3 | | 13.3 | 2.6 | 0.12 | | | | | | |
| Detailed | 207.1 | 194.5 | 186.6 | -12.6 | -6.1 | -0.24 | -7.8 | -4.0 | -0.5 | -20.5 | -9.9 | -0.3 |
| study | ± | ± | ± | ± | ± | ± | ± | ± | ± | ± | ± | ± |
| area | 7.2 | 5.5 | 5.4 | 6.4 | 3.1 | 0.12 | 5.4 | 2.8 | 0.34 | 6.4 | 3.1 | 0.1 |

Table 2.3: Mass balance results for the Zhadang and Gurenhekou glaciers on the Nyainqêntanglha Range, Nam Co Basin from 2005 to 2008. N_{ab} , N_{ac} , V_a , N_a is corresponding to net annual ablation, net annual accumulation, annual volume change, annual net specific mass balance, respectively. This table is based on the glacial investigation by [160].

| Mass balance year | | Mass balance | | | |
|-------------------|-----------|----------------------------------|----------------------------------|-------------------------------|------------------|
| | | N_{ab} (10^6m^3) | N_{ac} (10^6m^3) | V_a (10^6m^3) | N_a (m.w.e) |
| Zhadang | 2005/2006 | -2.15 | 0.10 | -2.05 | -1.1 |
| | 2006/2007 | -1.82 | 0.32 | -1.50 | -0.8 |
| | 2007/2008 | -0.23 | 0.60 | 0.37 | +0.2 |
| Gurenhekou | 2004/2005 | -0.59 | 0.05 | -0.54 | -0.4 |
| | 2005/2006 | -0.73 | 0.32 | -0.41 | -0.3 |
| | 2006/2007 | -0.73 | 0.48 | -0.25 | -0.2 |
| | 2007/2008 | -0.28 | 0.63 | 0.35 | +0.3 |

One of recent experiments on glacier surface parameters monitoring was set up on Glacier Zhadang and Gurenhekou located on the north and south sides of the ridge, Nyainqêntanglha Range. In this study, the long term conditions of temperature and precipitation within this region were analyzed based on the measurements at the six meteorological stations Xigaze, Lhasa, Damxung, Xainza, Baingoin, and Nagqu initially (1970-2008), while the NAMOR station was established by Chinese Academy of Sciences in 2006. The results imply that the temperature increased on both sides of the Nyainqêntanglha Range over last four decades, although the rate of temperature change on the northern side was larger than on the southern side during this period (1970–2007). Similarly, the average of annual precipitation on the southern side is much higher than the other side. The historical 1:100000 topographic map (with the horizontal accuracy 10 m), ASTER imagery (with the horizontal accuracy 15 m, acquired in 2007) were merged with the DGPS campaign in 2007 and processed to determine the change in glacier area over these decades. The results show that the reduction of the area on Zhadang glacier was at the rate of $0.017 \text{ km}^2\text{y}^{-1}$ i.e. faster than on the Gurenhekou glacier where it was $0.006 \text{ km}^2\text{y}^{-1}$ from 1970 to 2007. The mass balance of these two glaciers was also evaluated Zhadang (2005-2008) and Gurenhekou (2004-2008). The conventional drilled stake method was applied. The arrays of drilled stakes were installed to cover all the areas of accumulation and ablation zones on these glaciers (Zhadang 16 drilled stakes, Gurenhekou 20 drilled stakes) [160]. There are more negative mass balance signals detected on the Glacier Zhadang than Gurenhekou , except 2007/2008. The authors underline,

however, that the uncertainties on the locations, orientations, and elevations of these drilled stakes, must be taken into account, in combination with the spatial variability and seasonality of snowfall. All the measurements can be corresponding to the weakening of the Indian monsoon and strengthened westerlies within the Nyainqêntanglha Range region [160, 162, 164].

Table 2.4: Seasonal energy fluxes at the glacier surface and proportional contribution of each flux. Sum* indicates the sum of the energy fluxes in absolute values; the proportional contribution of each flux was calculated as $|energy\ flux|/sum$. This table is based on the glacial investigation by Zhang et al. [163].

| Mass balance year | Season | Sum* $W\ m^{-2}$ | S_{net} % | L_{net} % | H_S % | H_L % | G % |
|----------------------|--------|---------------------|----------------|----------------|------------|------------|--------|
| 2009/2010 | Winter | 136 | 33 | 42 | 16 | 8 | 0 |
| 2010/2011 | Winter | 134 | 35 | 45 | 13 | 5 | 2 |
| 2009/2010 | Summer | 173 | 62 | 26 | 6 | 4 | 2 |
| 2010/2011 | Summer | 147 | 52 | 34 | 6 | 7 | 2 |
| All observed periods | - | 148 | 45 | 37 | 10 | 6 | 2 |

Table 2.5: Calculated annual and seasonal mass-balance components at automatic weather station 2 (AWS2): mass balance=precipitation-runoff-evaporation; runoff=rainfall+meltwater-refrozen water (mm w.e.). This table is based on the glacial investigation by Zhang et al. [163].

| Mass balance component | 2009/2010 | | 2010/2011 | | 2009/2010 | 2010/2011 |
|------------------------|-----------|--------|-----------|--------|-----------|-----------|
| | Winter | Summer | Winter | Summer | | |
| Precipitation | 112 | 456 | 64 | 423 | 568 | 487 |
| Rainfall | 0 | 118 | 0 | 63 | 118 | 63 |
| Snowfall | 112 | 338 | 64 | 360 | 450 | 424 |
| Meltwater | 0 | 2427 | 0 | 867 | 2427 | 867 |
| Refrozen water | 0 | 117 | 0 | 104 | 117 | 104 |
| Runoff | 0 | 2428 | 0 | 826 | 2428 | 826 |
| Evaporation | 69 | 40 | 46 | 46 | 109 | 92 |
| Mass balance | 43 | -2012 | 18 | -449 | -1969 | -431 |

The experiment on Zhadang glacier included detailed monitoring of glacier surface parameters. All the measurements were acquired by two automatic weather stations (AWSs) and one automatic energy budget station, which were maintained Glacier Zhadang since 2005 and 2009, respectively. These two automatic

weather stations (AWS 1 5400 m.a.s.l and AWS 3 5800 m.a.s.l) aim to assemble the basic meteorological observations. The target of the successive automatic energy budget station (AWS 2 5660 m.a.s.l) is more specifically for the glacier surface energy budget monitoring. The parameters such as, incoming and reflected radiation, air temperature, net radiation are recorded in a time series. As described in the previous section Eq. 2.3, the general energy balance model is used for surface energy balance estimates on Glacier Zhadang. All the assembled in situ surface parameters are used as model input. Other variables were estimated, e.g. surface albedo, and longwave radiation, and appeared to be mutually coherent. During the experimental period, the turbulent sensible (10%) and latent heat fluxes (6%) were more dominant in the surface energy fluxes compared with subsurface heat flux ($\sim 2\%$ of the total energy fluxes). The seasonal fluctuation of these energy fluxes primarily results from the net shortwave and longwave radiation, which are also influential on the mass balance process. For instance, the melt process is rare due to the negative net all-wave radiation (mainly induced by the negative longwave radiation) in winter. At times, an energy sink is developed and the energy is compensated by the positive turbulent and subsurface heat fluxes on the glacier. In the case of summertime, the net shortwave radiation is more dominant with net radiation inducing ice melt. Moreover, the seasonality and forms of precipitation seem to be influential on the differences of the summer mass balance between 2010 and 2011 as well [163].

3

Parameterize surface roughness based on ICESat/GLAS full waveforms

Glaciers in the Tibetan mountains are expected to be sensitive to turbulent sensible and latent heat fluxes. One of the most significant factors of the energy exchange between the atmospheric boundary layer and glacier is the roughness of the glacier surface. However, methods to parameterize this roughness for glaciers surface in the remote regions are not well known. In this paper we use the data acquired by ICESat/GLAS laser altimetry from February, 2003 to November, 2004, along several tracks over glaciers of the Nyainqêntanglha range, in central Tibet. We make a study of the waveforms measured by the ICESat/GLAS laser system over mountainous and glacial areas. The surface characteristics are evaluated within laser footprints over the glacier outlines based on the glaciological inventory of the Tibetan Plateau constructed by CAREERI, CAS. For this purpose, we extract waveform parameters: the waveform width, the number of modes, the RMS width of the waveform. These parameters are compared with surface slope and roughness obtained from the ASTER GDEM (Global Digital Elevation Model). Through this analysis, the impact of morphology on the returned laser waveform is shown for the Nyainqêntanglha range. Roughness, and slope of the surface can be quite significant and may contribute from several meters to tens of meters to the pulse extent. The waveform analysis results indicate that the received waveforms are an accurate representation of surface relief within the GLAS footprints.

3.1. Introduction

Recent meteorological and glaciological studies show that a significant proportion of the total energy absorbed by glacier surfaces comes from turbulent fluxes [23, 34, 98, 101]. When evaluating the energy exchange over glaciers, the atmospheric boundary layer (ABL) is generally supposed to be stratified [8, 9]. This energy transfer process is commonly parameterized by the 'bulk eddy' aerodynamic method, which assumes that airflow in the atmospheric boundary layer is turbulent and fully adjusted to the underlying terrain. Monin-Obukhov similarity theory is applied to parameterize the relation between the meteorological elements and surface fluxes. At the same time, these stratification effects in the atmospheric boundary layer (ABL) are considered as well [7, 35, 58]. The irregularity/undulations of the glacier surface, besides albedo, temperature, and so on, are significant controllers during the surface-atmosphere exchange of mass and energy [10]. Normally, this irregularity is defined as roughness, which is parameterized as a momentum sink for the atmospheric flow.

These surface irregularity/undulations are generally categorized according to their size. The large-scale undulations have usually a typical wavelength of 3-4 times the ice thickness [25]. In contrast, small-scale surface irregularities associated with sastrugi and wind-formed features, form over periods of hours to days and are inherently transient and unpredictable in a deterministic sense [132]. The other type, containing crevasses, is developed where the stresses of the ice form variations in flow exceeding the breaking strength of the ice in tension. Glaciers with these types of features are widely distributed in mountainous areas, and their shape and flow are characterized by fluctuating surface relief, flowing downhill. Many energy balance models use refinements of the boundary layer turbulence theory, as described by [99]. The aerodynamic roughness z_0 is used to scale the logarithmic increase of wind speed with height in a neutrally stratified layer from a level of no motion near the surface. Furthermore, the aerodynamic roughness z_0 is experimentally determined from high-precision wind velocity and air temperature profiles. Such resulting roughness estimates are found to be in good agreement with the existing relationships linking the geometric and the aerodynamic roughness. This suggests that for natural surfaces, z_0 can be estimated on the basis of the geometric characteristics of the roughness elements.

Under normal turbulent flow conditions over melting snow and ice surfaces, z_0 depends solely on the dimensions, and density distribution of surface roughness elements [6, 9, 103, 127]. The value of z_0 increases with increasing height, surface area and density of surface roughness, until the ratio between the silhouette area (upwind face of elements) and unit ground area reaches 0.4. After this value, a transition to 'skimming' flow occurs and z_0 starts to reduce again [24, 54].

The standard method to derive z_0 is from the vertical profiles of horizontal wind speed and air temperature, using measurements at two or more heights in the atmospheric boundary layer (ABL).

Until the past decades, there have been two main acceptable strategies to estimate the aerodynamic roughness. On one hand, in situ-measurements dependent on the bulk transfer equations were tested both for polar ice sheets and various mountainous glacier zones [7]. The temperature, wind speed, and other relevant meteorological elements are recorded and applied for a local aerodynamic roughness approximation. On the other hand, since the end of last century, work done by [37, 94, 128] indicate that the capabilities of measurements obtained by laser and optical remote sensing are promising for the determination of the aerodynamic roughness. Compared to conventional techniques, these approaches to estimate z_0 by remote sensing measurements are potential to achieve a resolution that is much higher than meteorological measurements in both the spatial and temporal domain.

Spaceborne laser altimetry is a relatively new instrumental possibility to assess the morphology of the illuminated objects based on the full waveform information. The return waveform is influenced by effects like cloud attenuation, system noise, and morphology et al.. NASA launched in January, 2003, the Ice Cloud and land Elevation Satellite (ICESat), whose accuracy reaches 15 centimeters in the vertical direction within a ~ 65 m footprint, with a spacing of ~ 172 m between two adjacent shots [2]. Compared to radar altimeter missions, the emitted pulse width and laser divergence both decreased. These properties enable ICESat/GLAS to observe relatively small-scale characteristics of morphology of glaciers in the alpine zone.

Although, the track coverage in middle latitude areas (such as the Tibetan Plateau) is not as dense as over the polar zones, it still supplies enough signals for statistical analysis of the full waveform signal. Therefore, we address the following issues in this research: (i) estimate the theoretical relation between spaceborne laser signals and surface irregularity. (ii) derive the representative parameters of this irregularity as roughness from spaceborne laser altimetry.

3.2. Study area and Data

3.2.1. Study area

In this study, we consider the glaciers *Guren*, *Guila*, *Lisheng*, and *Bili* located on the south slope of the Nyainqêntanglha ($30^{\circ}19'0''\text{N}$, $90^{\circ}7'50''\text{E}$) range. It is a mountain range lying approximately 300 kilometers north-west of Lhasa in central Tibet [27]. The ice volume of about 4900 km^3 is distributed over 7080 glaciers in this mountain range. Nevertheless, there are only 28 valley glaciers longer than

10 km [154, 165]. These glaciers play a significant role in the circulation of the Yarlung Tsangpo and Nu Rivers. The study area is limited by elevation range from 4498 m to 7162 m. and the mean slope is 17.51° . A glacier inventory is a basic tool to explore issues related to glacial studies and morphology studies in glacial areas. Since 1970s, Chinese scientists have focused on this task through aerial photographs and in situ measurements. The latest Chinese glacier inventory has been a fusion of new topographic maps, DEMs, optical imagery (ASTER, Landsat TM/ETM) and historical records. All the four glacier outlines used below correspond to the Chinese glacier inventory by CAREERI, CAS described in [121, 122].

3.2.2.2 ICESat/GLAS data

The Geoscience Laser Altimeter System (GLAS) is loaded on the ICESat satellite. This instrument consists of two channels, at 1064 nm and 532 nm. The first channel is designed for the measurement of surface topography. There are three lasers on ICESat/GLAS. Laser 1 started to collect data in February, 2003, but it failed shortly after its launch. Laser 2 and 3 have collected data with a number of 33 day sub-cycle campaigns to increase their longevity. The receiver on GLAS records the echo waveform in 200 bins over sea and 544(1000) bins over land, depending on which of the two lasers is used, with a beam width of $\sim 110 \mu\text{rad}$ and a pulse rate of 40/s [77].

The ICESat /GLAS data used in this study were acquired within campaign L2A(September–November, 2003), L2B(February–March, 2004), L2C(May–June, 2004), and L3A(October–November, 2004). Among 15 GLAS data products, we investigate the products of Level 1A raw data and Level 2 global land surface elevation data, release 428 and 429, available from the National Snow and Ice Data Center (NSIDC). The GLAS products used in the assessment are GLA01 (L1A Global Altimetry) and GLA14 (Land Surface Altimetry). The former stores the transmitted and received waveforms from the altimeter while the latter contains land surface elevation, land footprint geolocation and reflectance, as well as geodetic, instrumental, and atmospheric corrections for range measurements. These two datasets can be linked by the record index and shot number(1-40). A total of 1316 shots is picked out for further evaluation in this area. The area illuminated by the GLAS/ICESat pulse will vary significantly during the span of each campaign, over the course of one orbit, and even shot by shot (shown in Fig. 3.1).

3.2.3. ASTER GDEM data

ASTER imagery is captured from a multi-spectral imaging sensor on-board the NASA Terra platform, launched in December, 1999. It is designed to monitor sur-

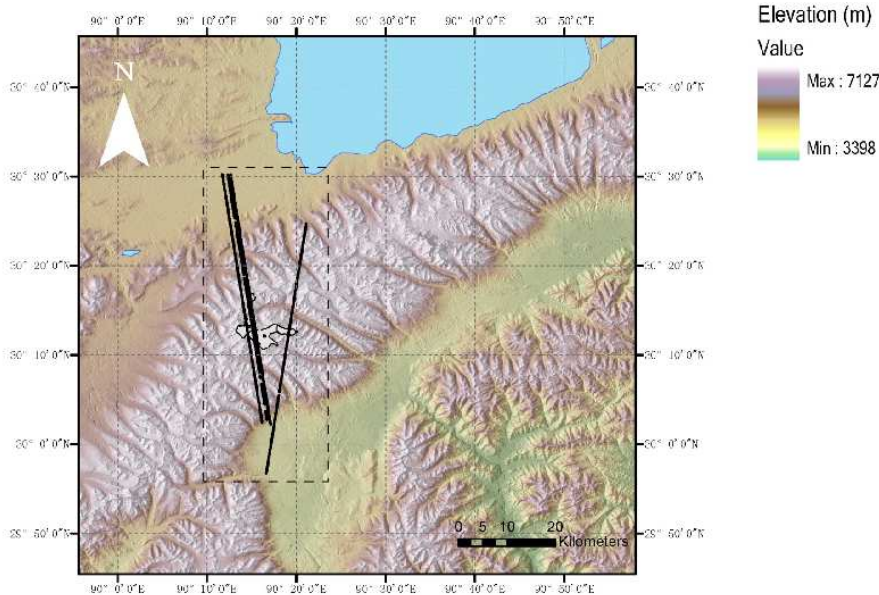


Figure 3.1: The measurements were performed by ICESat/GLAS laser altimetry in 2003 and 2004. The bold lines indicate the ICESat tracks over the study area, the background is the rendered elevation captured from ASTER GDEM, the outline of Nam Co lake mask is taken from MODIS MOD44W water mask. The glacier outlines are cropped from the Chinese Glacier Inventory, CAREERI, CAS.

face geodynamic processes, such as, glacier movements, land slides and flood disaster assessment, by higher resolution and better coverage than other previous space-borne optical instruments. The main spectral and geometric capabilities of the imaging system, are three VNIR (visible and near-infrared), six SWIR (short-wave-infrared), five TIR (thermal infrared) bands and one NIR along-track stereo band with 15 m, 30 m, 90 m, and 15m spatial resolution, respectively [147].

For normal ASTER DEMs generation, the stereo band 3B is often combined with 3N (the same spectral range $0.76 - 0.86\mu m$) [45]. After ground control point selection, epipolar image selection, image matching and geocoding, the final ASTER DEMs will be established. Then, ASTER DEM standard data products are resampled with 30 m postings, and with Z accuracies generally between 10 m and 25 m root mean square error (RMSE) [130].

The version of ASTER Global DEM (GDEM1) in this study was released to the public on June 29, 2009. There are 1.2 million DEM tiles covering land surfaces between $83^{\circ}N$ and $83^{\circ}S$ latitudes. The general quality is estimated at 20 meters at 95 % confidence for vertical data and 30 meters at 95 % confidence for horizontal data. Due to the lack of GPS and other sources of ground control points, cloud

contamination and water masking issues, the DEMs in high elevation regions like Nam Co Lake, Nyainqêntanglha Range still need to be validated.

3.3. Methods

3.3.1. Slope and roughness derived from ASTER GDEM

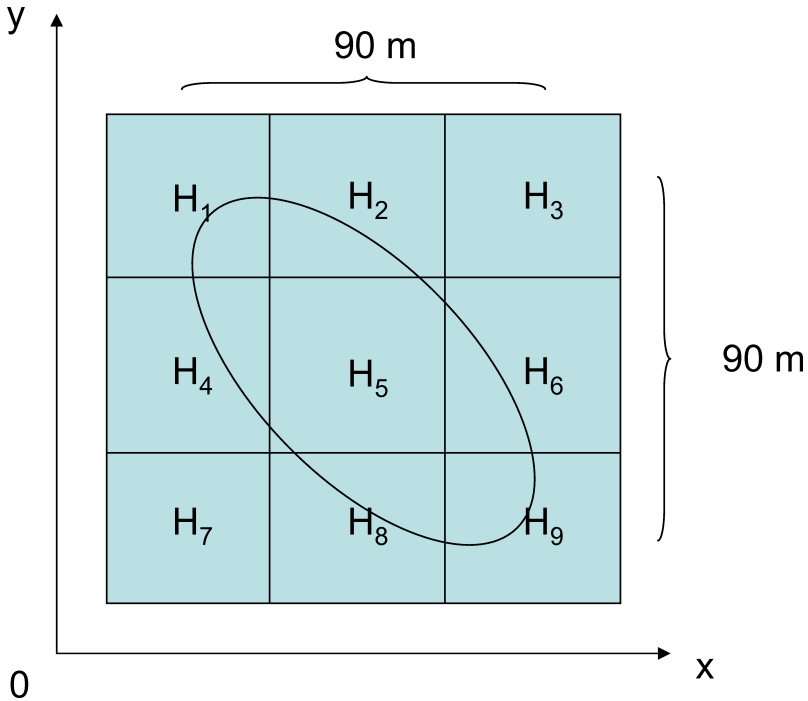


Figure 3.2: Example of a moving window. The black ellipse corresponds to one footprint of ICESat illuminating the surface target. Each pixel is 30 m×30 m, the characters from H_1 to H_9 indicate the magnitude of elevation. Both slope, and roughness will be calculated at this moving window scale.

To evaluate the GLAS performance over mountainous glacial surfaces of varying relief, slope and roughness values for representative geomorphological terrains in our study area were quantified using ASTER GDEM. These two parameters were defined at a length scale of 90 m, approximating the footprint diameter of the GLAS laser beams, by calculating the best fitting local mean plane to a 3×3 grid of elevation values (see Fig. 3.2). The slope calculation (Equations 1 to 5) used the algorithm described by [26].

$$slope_{radians} = \arctan(\Delta S) \quad (3.1)$$

$$\Delta S = \sqrt{(dz/dx)^2 + (dz/dy)^2} \quad (3.2)$$

$$[dz/dx] = \frac{(H_3 + 2H_6 + H_9) - (H_1 + 2H_4 + H_7)}{8 * x_cell_size} \quad (3.3)$$

$$[dz/dy] = \frac{(H_7 + 2H_8 + H_9) - (H_1 + 2H_2 + H_3)}{8 * y_cell_size} \quad (3.4)$$

where dz/dx and dz/dy are the height change rate of the surface in two orthogonal directions from the center cell. Then, we transform the unit of slope from radians to degrees using Equation 3.5 (see Fig.3.2).

$$slope_{degrees} = slope_{radians} \cdot \frac{180}{\pi} \quad (3.5)$$

The surface roughness can be defined in several different ways, but for consistency with the ICESat data, we quantified the roughness from the ASTER GDEM data as the standard deviation of the differences with the locally best fitting plane as follows. First, the plane $P(x, y)$ best fitting the elevations in the 3×3 ASTER GDEM window, in the least square sense is estimated, given by

$$P(x, y) = rx_i + sy_i + t \quad (3.6)$$

Then, the roughness σ_R is defined as

$$\sigma_R = \sqrt{\frac{1}{9} \Delta H} \quad (3.7)$$

with

$$\Delta H = \sum_{i=1}^9 [H_i - (rx_i + sy_i + t)]^2 \quad (3.8)$$

All these implementations are done in the commercial software Arc/Infor.

3.3.2. ICESat full waveform fitting process

The quality of the full waveform is essential to determine the range from the satellite to the features on the ground. Normally, the emitted pulse is considerably stable and introduces little error in the elevation calculation. However, the echo waveform can be modified by changes in emitted pulse energy, cloud effects, surface reflectivity and characteristics of the surface illuminated within a single laser footprint [158]. To shape the features of echo waveforms, we used a waveform fitting procedure to remove noise. Waveforms were removed from further analysis due to one of the following reasons:

- The raw waveform can not be decomposed by the Gaussian fitting algorithm.
- The deviation between ICESat GLA14 and ASTER GDEM is greater than 100 m.

Based on previous ICESat waveform studies by the NASA ICESat/GLAS team, the assumption is that the waveform is decomposable as a number of Gaussian components and a noise component [1, 3]. In our case, the glaciers of interest are located in a continental summer-precipitation climate. In general, the peaks of the echo waveform represent relevant surface morphological features. Waveform extent is defined as the vertical distance between the first and the last elevation at which the waveform exceeds a threshold level corresponding to the peak and 4 times the standard deviation of the background noise [2]. The decomposition of the waveform is formulated as follows:

$$w(t) = \sum_{m=1}^{N_p} W_m + \varepsilon \quad (3.9)$$

$$W_m = A_m e^{-\frac{(t-t_m)^2}{2\sigma_m^2}} \quad (3.10)$$

where $w(t)$ is the amplitude of the waveform at time t , W_m is the contribution from the m_{th} Gaussian mode, N_p is the number of Gaussian modes found in the waveform, A_m is the amplitude of the m_{th} Gaussian, t_m is the Gaussian position, σ_m is the $\frac{1}{e}$ half-width (standard deviation) of the m_{th} Gaussian, and ε is the bias (noise level) of the waveform.

The original data from GLA01 is formatted in binary and counts. We converted them to ASCII and voltage for further processing. In the fitting step, Gaussian components are fitted to the return waveform.

A robust least-squares method is used to compute the model parameters. That is, the values of ε , A_m , t_m , σ_m are obtained by fitting the theoretical model to the observed waveform in such way that the difference between model and observation is minimized in the least-squares sense. The parameters n modes (the number of fitted peaks), and the full waveform width are generated for further analysis in later sections [43]. Both of them encode specific physical information: n_{modes} , the number of waveform peaks, roughly corresponds to the number of elevation levels (including the objects and the earth surface). And the width of the full waveform represents the elevation range between lowest and highest surface elements within an ICESat/GLAS footprint (Fig.3.3).

Theoretical impact of morphology on the ICESat full waveform

In this paragraph the theoretical response of an ICESat waveform on the reflecting terrain is described [52]: This theory assumes that the average waveform

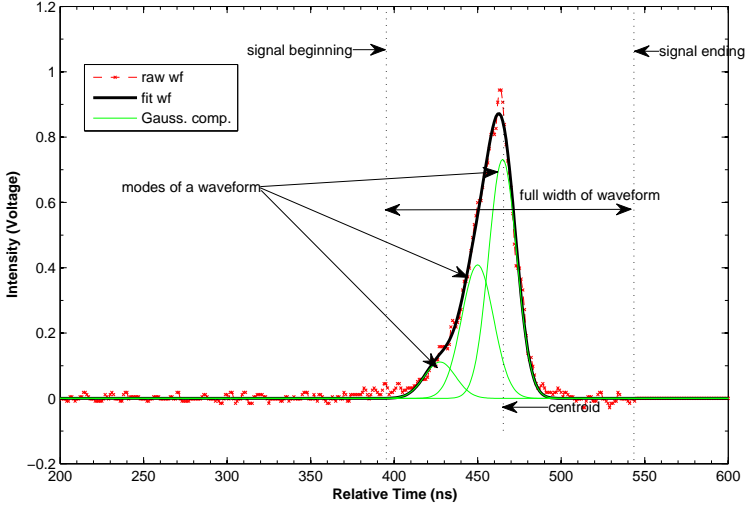


Figure 3.3: Demonstration of the waveform width and waveform modes of a typical ICESat/GLAS returned waveform. The red dashed line, the black solid line and the green solid line represent the raw waveform, the fitted waveform and the Gaussian components, respectively. Here, the number of modes is 3; the width of full waveform equalizes to about 145 ns corresponding to ~ 21 m.

shape due to terrain reflection is related to the probability density of variation of terrain elevations within the laser footprints. We use the series of equations below, these items are defined at first: the photon counts N , the centroid time of the received pulse T_p , the rms pulse width σ_{SR} , which are the function of temporal moments of the pulse and defined as follows.

$$N = \int_0^{\infty} p(t) dt \quad (3.11)$$

$$T_p = \frac{1}{N} \int_0^{\infty} t p(t) dt \quad (3.12)$$

$$\sigma_{SR}^2 = \frac{1}{N} \int_0^{\infty} (t - T_p)^2 p(t) dt \quad (3.13)$$

where $p(t)$ is the real signal strength. Furthermore, these parameters are

proved sensitive for certain statistics of the surface target [53].

$$\begin{aligned}
 (\sigma_{SR}^2) = & \quad \sigma_F^2 + \sigma_h^2 \\
 & \quad \text{(system effects)} \\
 & \quad + \frac{4Var(\Delta\xi) \cos^2 S_x}{c^2 \cos^2(f+S_x)} \\
 & \quad \text{(surface roughness effects)} \\
 & \quad + \frac{4z^2 \tan^2 q_t}{c^2 \cos^2 f} \\
 & \quad \text{(beam curvature effects)} \\
 & \cdot [\tan^2 q_t + \tan^2(f + S_x) + \frac{\tan^2 S_y \cos^2 S_x}{\cos^2(f+S_x)}] \\
 & \quad \text{(nadir angle and surface slope effects)}
 \end{aligned} \tag{3.14}$$

where

σ_F —the transmitted laser rms pulse width

σ_h —the rms width of receiver impulse response

$Var(\Delta\xi)$ —rms roughness of the statistical surface

c —speed of light

S_x, S_y —along-track and across-track slope, respectively

q_t —laser beam divergence angle

f —laser pointing angle off nadir

For the GLAS system both the pointing uncertainty (1.5 arcsec) and the normal off-nadir pointing angles (< 1 deg) are small, thus the above equation was simplified as:

$$\begin{aligned}
 (\sigma_{SR}^2) = & \quad \sigma_F^2 + \sigma_h^2 \\
 & \quad \text{(system effects)} \\
 & \quad + \frac{4Var(\Delta\xi)}{c^2} \\
 & \quad \text{(surface roughness effects)} \\
 & \quad + \frac{4z^2 \tan^2 q_t}{c^2} \\
 & \quad \text{(beam curvature effects)} \\
 & \cdot [\tan^2 q_t + \tan^2 S] \\
 & \quad \text{(nadir angle and surface slope effects)}
 \end{aligned} \tag{3.15}$$

From these equations, the laser system contribution to the width of the received pulse include the widths of the transmitted pulse and the receiver impulse response. The received pulse is broadened by the surface roughness and slope of the ground target and by the beam curvature.

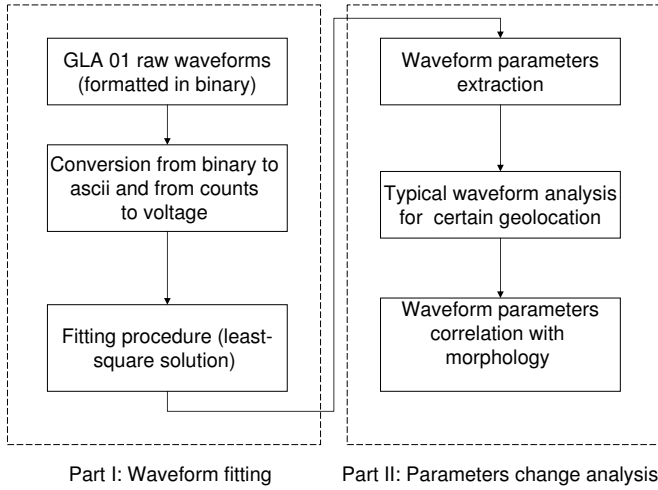


Figure 3.4: Processing chain of full waveform parameter evaluation. It includes two work flows fitting processing and parameter analysis. The raw waveform data of GLA01 is converted to ascii format, unit are transferred from count to voltage, and Gaussian modes are fitted using the least-squares method in Part I. All these steps were implemented as IDL and matlab scripts. Part II comprises waveform parameters extraction, filtering, analysis of typical example waveform, waveform parameters correlation with morphology in this region.

The relevant procedures of this study are summarized in a scheme in Fig.3.4. Part 1 is mainly about the full-waveform fitting algorithm. We use the methodology mentioned before to fit all the selected waveforms in the study region. Part 2 aims at comparing the waveform parameters obtained from the fitting procedures to the topographic slope and roughness as obtained from ASTER GDEM.

3.4. Results

In this section, we show several typical example waveforms for different locations in the area and analyze the variation according to their topography and landscape type. Moreover, we do a case study to investigate the distribution of parameters on the named glaciers *Guren*, *Guila*, *Lisheng*, and *Bili*. We divided each of the four glaciers into ablation and accumulation zone dependent on the glaciological inventory of Nyainqêntanglha by CAREERI, CAS. The attributes of these glaciers are mentioned in Table.3.1.

Next, we compare the ICESat derived parameters, elevation, waveform width and waveform number of modes to the ASTER GDEM elevation, roughness, and

Table 3.1: It shows the morphological features of the four named glaciers in the study area, S, L, H, D, V represents area, length, elevation, depth and volume, respectively. t, ac, al, ex means total, accumulation zone, ablation zone, exposed area, respectively.

| | S_t (km^2) | S_{ac} (km^2) | S_{al} (km^2) | S_{ex} (km^2) | L_t (km) | H_{max} (m) | \bar{H} (m) | H_{min} (m) | H_{al} (m) | \bar{D} (m) | V (m^3) |
|---------|---------------------|------------------------|------------------------|------------------------|-------------------|----------------------|----------------------|----------------------|---------------------|----------------------|------------------|
| Guren | 5.6 | 1 | — | 5.6 | 4.2 | 6260 | 5830 | 5400 | — | 78 | 0.44 |
| Guila | 14.69 | 1 | 4.32 | 13.69 | 7.2 | 6384 | 5882 | 5380 | 5900 | 108 | 1.59 |
| Lisheng | 4.4 | 1 | 1.6 | 4.4 | 3.3 | 6360 | 5924 | 5488 | 5900 | 72 | 0.32 |
| Bili | 5.6 | 1 | — | 1.4 | 4.2 | 6080 | 5855 | 5630 | — | 48 | 0.07 |

slope. Finally, the experimental waveform response is estimated with the predicted response as discussed in Section 3.3.

Table 3.2: The waveform shift comparison between ablation zone and accumulation zone in Guila and Guren glaciers. n modes and W are chosen in the analysis. n modes means the number of peaks in each return pulse. W interprets as the width of full waveform (from the beginning to the end).

| | Guila | | Guren | |
|----------------|-----------------------|---------------------------|-----------------------|--------------------------|
| | Ablation zone (13) | Accumulation zone (19) | Ablation zone (14) | Accumulation zone (5) |
| <i>n modes</i> | 3.76 ± 2.2 | 4.68 ± 1.83 | 4 ± 1.51 | 6 |
| <i>W (m)</i> | 30.81 ± 17.24 | 43.02 ± 28.37 | 44.48 ± 11.58 | 70.44 ± 13.38 |

3.4.1. ICESat full waveform examples over the study area

Accumulation and ablation zones can be divided into much more specific zones, these being distinct zones with characteristics features in the surface layers of a glacier. As most laser scanning systems are operating in the near infrared part of the electromagnetic spectrum, some differences on the surface by different surface types e.g. snow, firn and ice can be observed.

In the view of glacio-morphology, over 90% of the glaciers in this study area are valley glaciers, mountain glaciers and small glaciers. First of all, we set several criteria to describe the morphological characteristics of the glacier: the general shape; the terminus location; the longitudinal profile; supply source of the glacier; activity of the ice tongue. Moreover, we geolocated the ICESat/GLAS samples on the glaciers using the CAREERI glacier mask. Finally, we pick up four larger glaciers *Guren*, *Guila*, *Lisheng*, and *Bili* to analyze further.

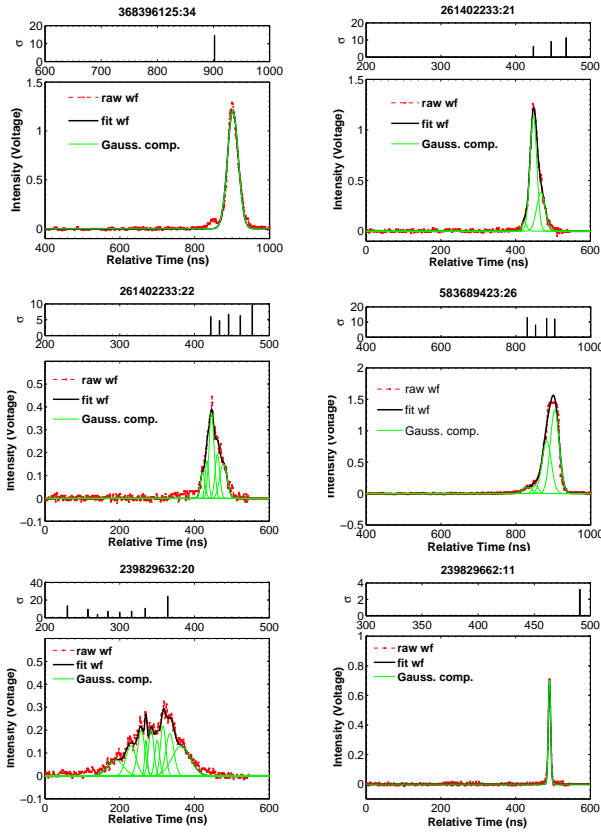


Figure 3.5: Typical waveform examples were picked out over different features. (a),(b) are in the accumulation zone of Guila, (c),(d) is in the ablation zone of Guila and Lisheng, respectively. (e) located in the rare mountainous area and (f) is on the lake surface. Note: to describe the complexity of bare mountainous area, we set number of modes larger than 6, when the specific plotting is implemented in (e).

The four named glaciers are close to each other and span an altitude range of 796.5 m on average. *Guren* glacier (30°12.78'N, 90°14.31' E) lies in a valley, the orientation of exposed area and ablation zone are both northern. It is a cirque from morphology, whose terminus is debris-covered and hill-downwards, the longitudinal profile is regular down to the hill-foot and not very steep. The tongue retreats slowly [102, 154]. *Guila* (30°11.92'N, 90°16.35' E) is located southeast of *Guren* and is also a valley glacier consisting of multiple-basins on the upward side. Its terminal is debris-covered, but the longitudinal profile reveals some ice-falls and crevasses and tower shape ice, the main source is avalanche and relevant snow. The retreat of the tongue is still not very fast. *Lisheng* and

Bili are mountain glaciers, niche, frontal characteristics is expended. The main mass source of the glacier is the same as for *Guren*, the glacier front has retreated slightly.

Mountainous terrain, where topographic relief within a footprint is small compared to landscape sizes typically yields a multi-modal GLAS waveform. The intensity is a good indicator for glacial optical properties. Ice, snow, and surface irregularities (mainly crevasses) show a good differentiation in terms of geometry and reflectance. Fig.3.5(a), (b) show shot 34 and 21 geo-located in the accumulation zone of *Guila*, whose slope and roughness are 9.9° , 1.01 m for shot 34; and 49.5° , 1.54 m for shot 21, respectively. The distribution is Gaussian in both cases, shot 34 is fitted with only one main peak, the amplitudes are both close to 1.2 v. Although the waveform width of shot 21 is broadened by the slope effect and is fitted with 3 peaks, it still comes from a glacier. We considered two other shots 22, 26 in the ablation zone of *Guila* and *Lisheng* (Fig.3.5(c), (d)). The most remarkable feature is their larger widths about 11.27 m, and 12.01 m, respectively. There are 5 peaks in shot 22, the peak of the last Gaussian mode responds to the lower ground surface within the ICESat 70 m footprint. Specifically, the number of peaks in shot 26 is less than 6 as well, the peak of last Gaussian mode corresponds to the surface elevation, and the maximum intensity is also much lower than the values in (a), (b). In combination with the glacier inventory by CAREERI, and Landsat TM imagery 2003, the waveform can be interpreted as over crevasses. Similarly, shot 26 is interpreted as coming from a debris overlaying the glacier. We find more oscillations in the return pulse which involved more morphological features.

Table 3.3: The attributes of culled out waveforms in both regions from February 2003 to November 2004. GLA, MOU, represent glacier, mountainous area, respectively.

| | GLA | MOU |
|-------------------|------|------|
| $n \text{ modes}$ | 4.8 | 4.89 |
| $W \text{ (m)}$ | 47.9 | 48 |

Through ICESat track coverage of the four glaciers analysis, we selected *Guila* and *Guren* as the most interesting regions for a case study. Then, we generated the distribution of these waveform parameters on both ablation and accumulation zones (see Table.3.2). The measurements locate in the ablation zone, near the tongue of the glacier, the area line is just below the equilibrium line. As well, the air temperature is above pressure freezing point, thus speeding up the melting of glaciers. In this area, there is no snow and possibly also a thin

layer of water covering the glacier. Clearly, the reflectivity of this area is lower than surrounding bedrocks. n_{modes} is sensitive to the roughness of the surface. The value of n_{modes} increased by the roughness of the four named glaciers ($1.03 \pm 0.04 \sim 1.15 \pm 0.17$ m) is larger than 3 on the average. Then, the situation in glacier and mountainous zone are computed and the results shown in Table.3.3. To link the ICESat waveforms and the morphology further, total of 1188 points is selected in the mountains.

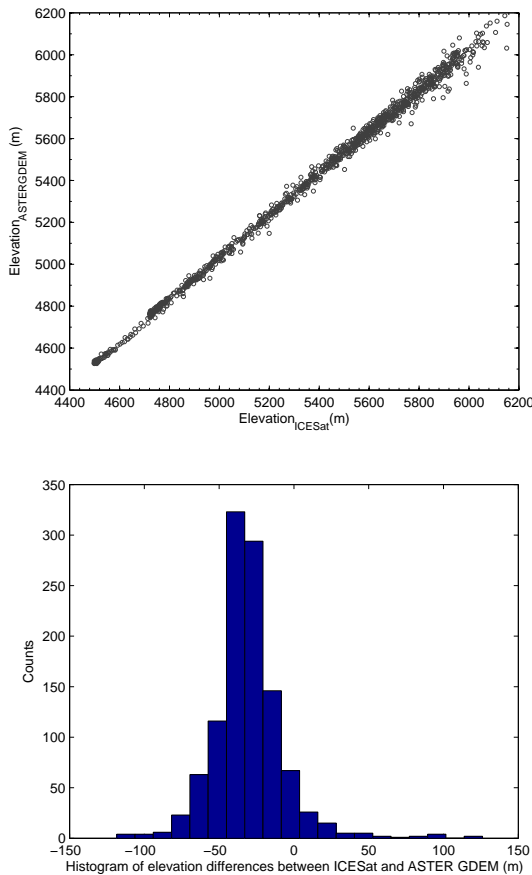


Figure 3.6: Correlation in elevation between ICESat and ASTER GDEM shown in (a); the histogram of deviations obtained from ASTER GDEM elevation subtracts from ICESat elevation shown in (b). We divide all the differences into 20 bins, the occupancies of variable deviations in different range can be found in this histogram.

3.4.2. Comparison of parameters derived from ASTER GDEM and ICESat data

To compare the quality of the ICESat elevations, we make a scatter plot of its elevation against that from ASTER GDEM. It shows a linear trend in Fig. 3.6(a). The differences of elevations between ASTER GDEM and ICESat are also visualized in the histogram in Fig. 3.6(b). In terms of absolute magnitude, our calculation shows that the accuracy of ICESat elevation is higher. And the largest difference is 126.10 m, the difference is on average around 33.96 ± 18.17 m over all the samples. The surface features roughness and slope are chosen as the shaping factor of the waveforms (see Fig. 3.7). Next, we compute the cumulative histograms of ASTER GDEM roughness and slope compared to the ICESat/GLAS full width of the return waveform, respectively (Fig. 3.8).

Based on the cumulative histograms above, we explore the variability and spreading (or dispersion) of the ASTER GDEM slope and roughness with ICESat number of modes and waveform width. Fig. 3.9 and 3.10 show the scatter plots of the ASTER GDEM slope and roughness vs. the ICESat waveform number of modes and the ICESat waveform width, respectively. As expected, both the number of modes and the waveform width increase, on average, with the corresponding ASTER GDEM slope and roughness. Indeed, both surface slope and roughness have a widening effect on the waveform: as the vertical distribution of scatterers increase with both growing slope and roughness, the waveform widens as there is more time difference between return time of the lowest and highest scatterer in the illuminated footprint. The relation between surface slope and roughness versus number of modes is less direct. But clearly, in the high relief mountainous terrain, the possibility of scattering at different heights, contributes to the increase of the number of modes.

3.4.3. Analysis of ICESat full waveform parameters as a function of morphology

In this section, we will measure surface roughness at scales on the order of the footprint size. As described before, the shape of the laser echo pulse reveals much about the topography of the region within the laser footprint. Different elevations within the area of footprint will reflect the light with different travel times, leading to pulse spreading. A height difference of h between two points would result in reflected photons returning with a time difference of $2h/c$, c being the speed of light.

Based on the theory in the methodology part, the terrain characteristics (slope S and roughness σ_R) can influence the spreading of the echo pulse shape combined with the rms width of the receiver impulse response and the rms laser pulse width.

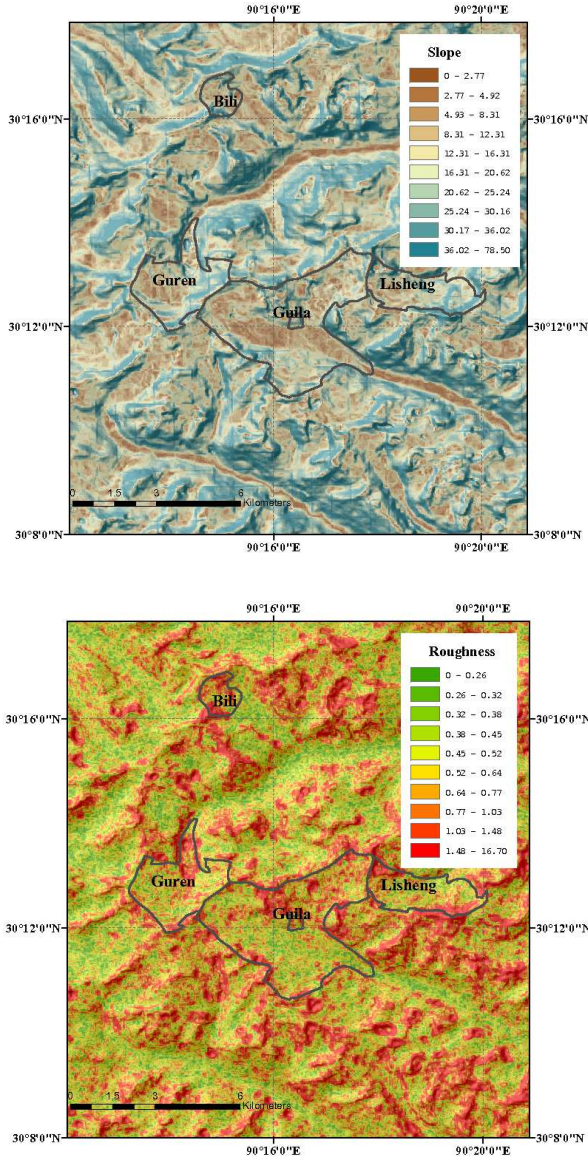


Figure 3.7: (a) slope (unit:degree) and (b) roughness (unit:meter) extracted from ASTER GDEM. The gray bold line is the outline of these four larger glaciers, *Guren*, *Guila*, *Lisheng*, and *Bili*. The values of the calculated slope and roughness are color scaled from low to high gradually.

Here, we use three parameters, σ_{SR} , the rms pulse width of the echo ICE-Sat laser signal (unit:ns), $\sigma_h = 0.425FWHM \approx 1.7$, the rms width of the receiver

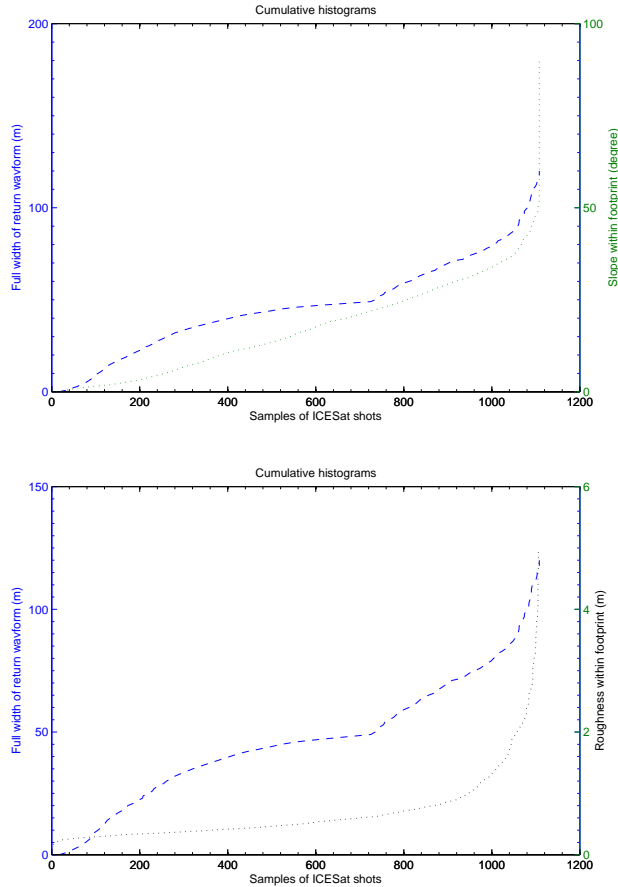


Figure 3.8: Cumulative histograms of surface slope with full width of return waveform shown in (a); Cumulative histograms of surface roughness full width of return waveform shown in (b), blue line indicates full width of return waveform, dotted line is surface slope in (a), dotted line is surface roughness in (b).

impulse response (unit:ns), and $\sigma_F = 6$, the transmitted ICESat laser pulse rms width (unit:ns). In the beginning, we fill the gaps of the σ_{SR} series by 1-D interpolation, caused by attenuation filtering procedure. Then, using the simplified expression[53], we set the interpolated σ_{SR} as initial estimates, to optimize the σ_{SR} by nonlinear least squares robust method. According to this process, all the possible singularities, due to σ_{SR} insufficiently large, can be avoided. Therefore, we obtain the final acceptable rms pulse width of the echo ICESat laser signal, satisfying the Equation (13-14). This can be interpreted as the general relation between the the terrain characteristics and returned ICESat laser pulse.

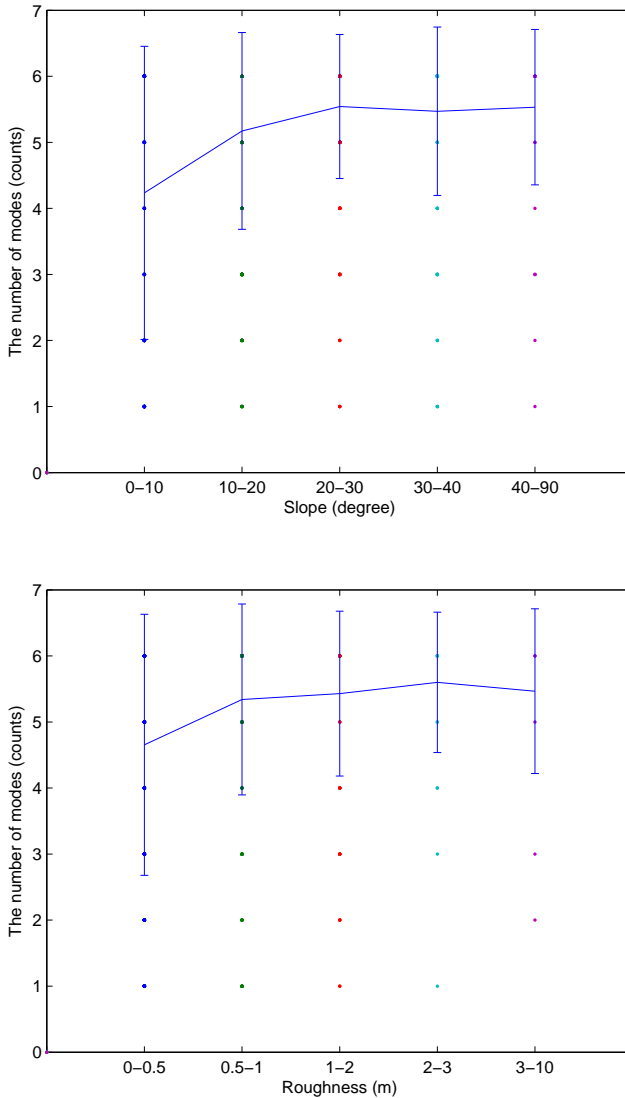


Figure 3.9: The distribution of ASTER GDEM derived slope and roughness vs. number of ICESat waveform modes.

Next, we classify the RMS width observation data into groups based on the slope and roughness, respectively. Specifically, we group the RMS width data into three groups (0 ~ 0.7 m), (0.7 ~ 1.0 m), (> 1.0 m). According to the range of the slope (0 to 60°), nearly all the observations fall into the dashed outlined

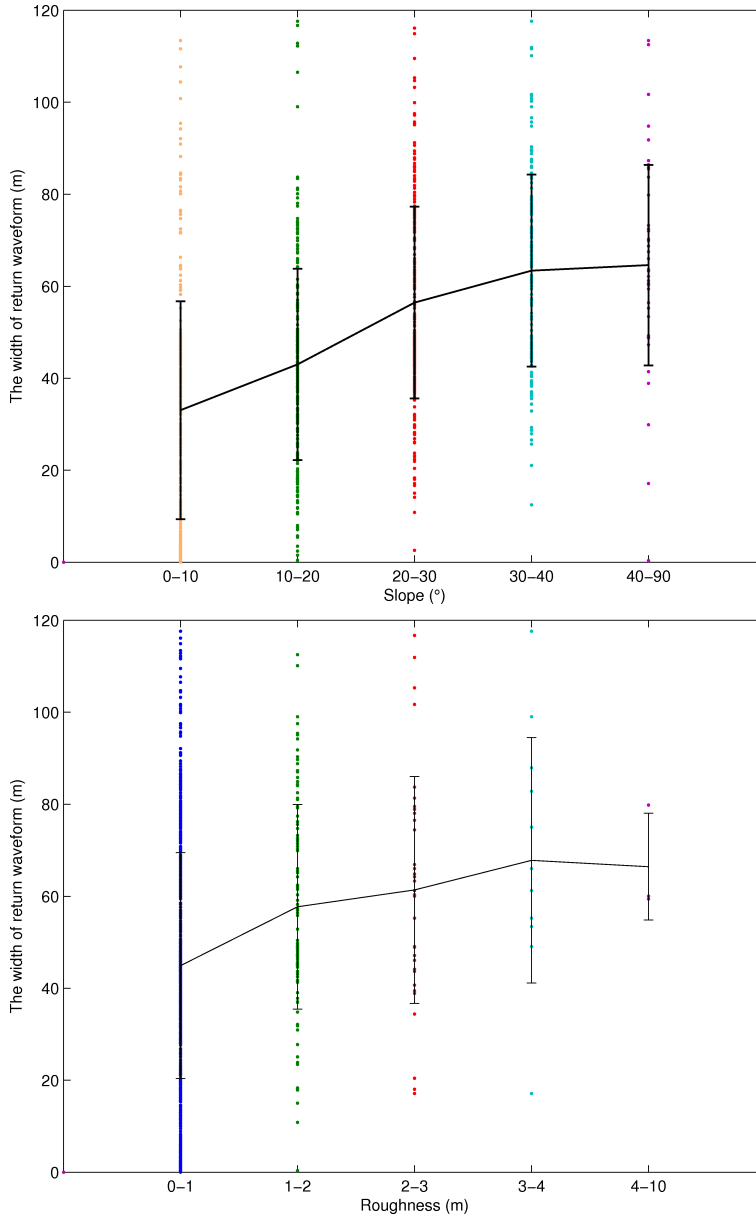


Figure 3.10: The distribution of ASTER GDEM derived slope and roughness vs. width of the full ICESat waveform.

zone. During each group, we divide the samples into several bins dependent on the slope at the interval of 10 °(see Fig. 3.11). All three different colored RMS

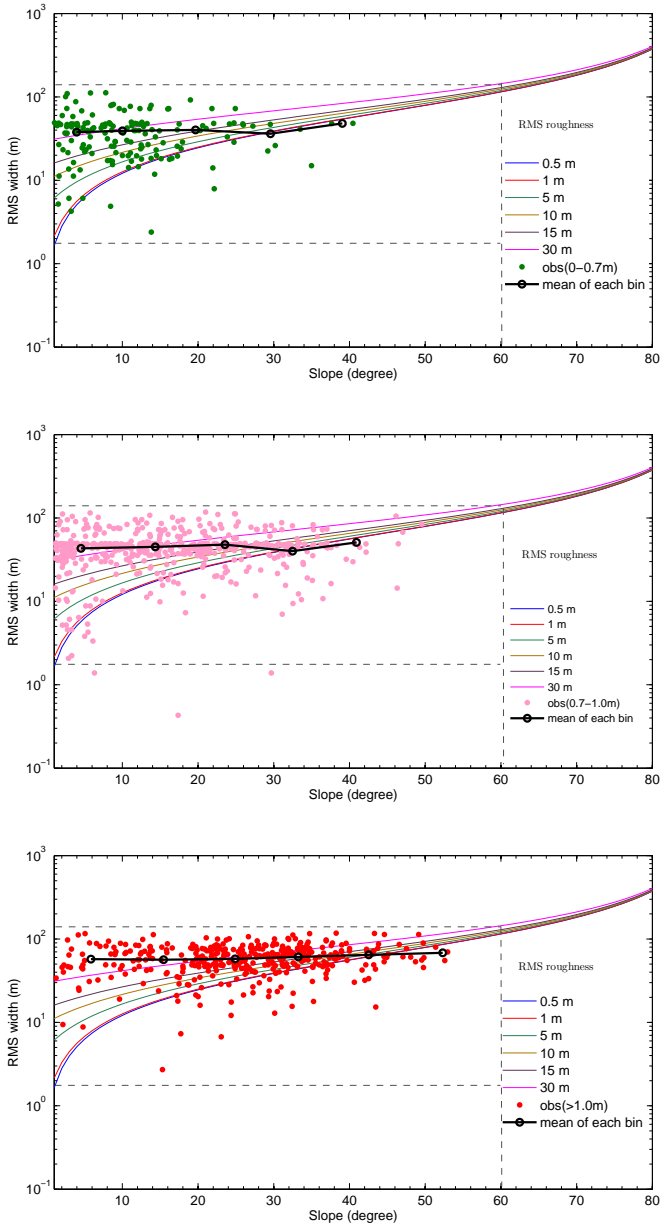


Figure 3.11: RMS width of received pules contributed by total slope and rms roughness for ICE-Sat/GLAS system. Each color line represents the series RMS width for certain RMS roughness. Owing to the RMS roughness, all the relevant RMS width observation values are classified three categories. Green dots shows the roughness values fall into 0~0.7 m, pink and red dots mean the roughness are in 0.7~1 m and larger than 1 m, respectively. Bold curve indicates the mean of each bin, in Fig.3.11.

widths groups show the approximate increasing trend with the majority of slope. Simultaneously, the average of RMS widths in Fig. 3.11 show a slightly increasing trend with each group of the majority of RMS roughness in general. And in Fig. 3.12, the group 1 (obs 0-0.7 m) and group 2 (obs 0.7-1.0 m) show a little drop in the general increasing trend. Perhaps, this results from the existing extreme values in the groups, and the relative small number of samples (only 8 in group 1, and 78 in group 2) compared with the other groups.

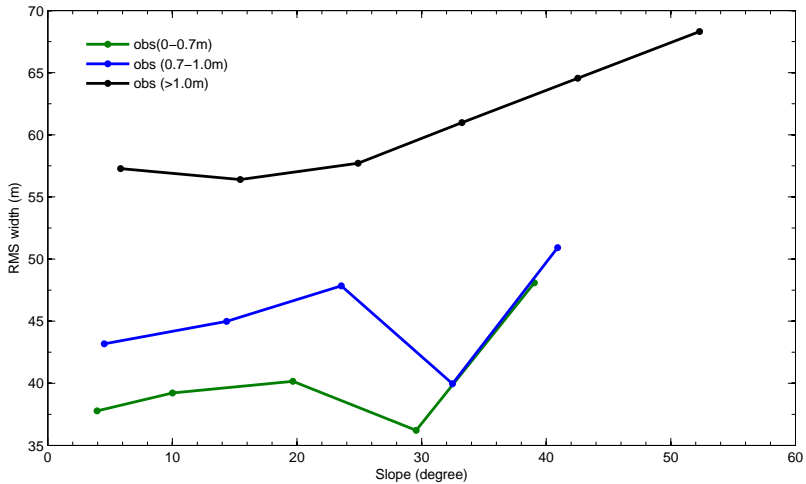


Figure 3.12: This figure shows bold curves, which indicates the mean of each RMS width bin grouped by slope.

In total, the results indicate that the roughness approximately contribute to increasing rms widths. And it is also shown that a dispersion of the rms width based on roughness at low total slopes from analysis above. But at steep slopes zone, rms widths are insensitive to roughness and increase logarithmically with the slope. In other words, the variation of width caused by roughness are not considerably compared to the change caused by slopes. In general, surface roughness is related to the spreading of the Gaussian pulse. Thus, pulse spreading can be caused by footprint roughness or by footprint-scale sloping. For much of the terrain, the dominant cause of spreading is from roughness rather than from slope (Fig. 3.11, 3.12). Furthermore, we use the terrain response function and its variance to calculate the ICESat-derived roughness shown in Fig.3.13. From this figure (3.13), we find that the ICESat-derived roughness fluctuates consistently during the relevant smaller range. To quantify the changes between these two roughness, we compute the distribution of the deviation between the ICESat-

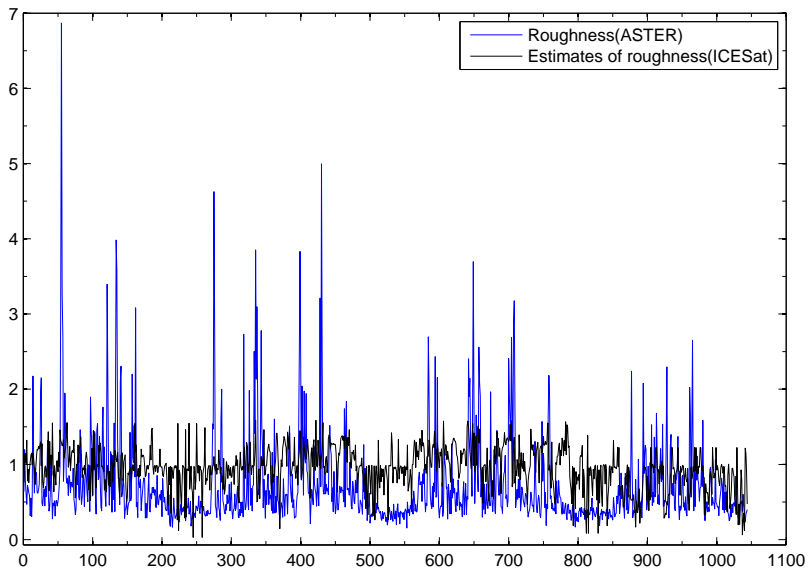


Figure 3.13: The comparison of surface roughness from ASTER GDEM (blue) against the roughness from ICESat waveform (black). All the values of the two roughness are in meters.

derived roughness and the ASTER GDEM-derived roughness in Fig. 3.14 (a). The results shows that the ICESat-derived roughness fluctuates from 0.03 m to 1.58 m, compared with the ASTER GDEM-derived roughness that varies between 0.15m and 6.87 m. Over 90% of the absolute deviation of these two roughness falls between 0 and 2 m. Simultaneously, the PDF (possibility density function) of the roughness deviation follows very well with a gamma function (see Fig. 3.14 b).

3.5. Conclusions

We studied the extraction of parameters of waveforms measured by the ICESat/GLAS laser system. We give examples of these parameters over mountainous and glacial terrain. Furthermore, we compare these full waveform parameters derived from ICES/GLAS: number of modes, width of the full waveform and elevation, with surface features derived from ASTER GDEM: roughness, slope and elevation. Through this analysis, the response of the laser waveform to morphology is studied for our region of interest. In terms of descriptive statistics, the relationship between ICESat/GLAS waveform attributes and surface parameters from ASTER-GDEM is investigated as well. Next, the link between the theoretical influence of surface slope and roughness on the ICESat waveform parameters and the practical results is quantified. Consequently, the received laser shape can be described by the contribution of terrain characteristics.

In our study area, roughness and slope of the surface can contribute several meters to even several tens of meters to the pulse shape. Simultaneously, the representative parameter of this irregularity, roughness is derived from ICESat/GLAS as well. These results confirm that spaceborne laser altimetry is potentially efficient to describe the irregularities of terrain over high altitude mountainous areas. This means that satellite full waveform laser altimetry is a new capable way to derive basic elements (the terrain irregularities) of the energy exchange process in the atmospheric boundary layer of remote areas in the Tibetan Plateau and similar mountainous regions on Earth.

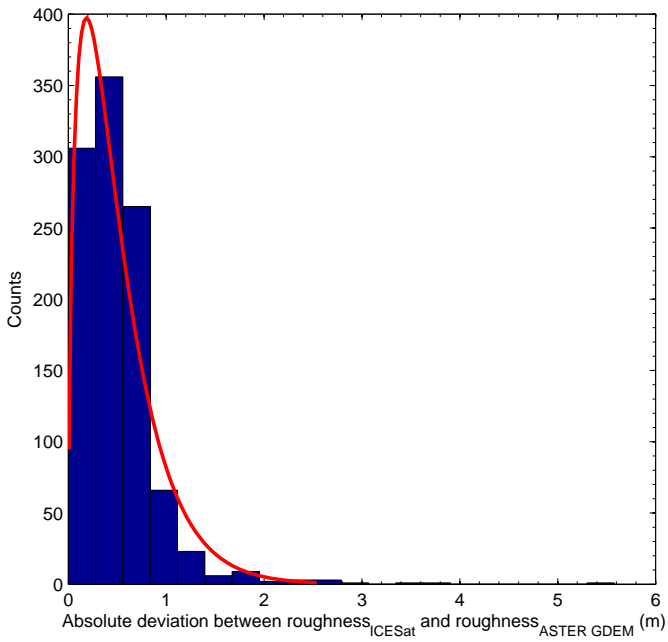
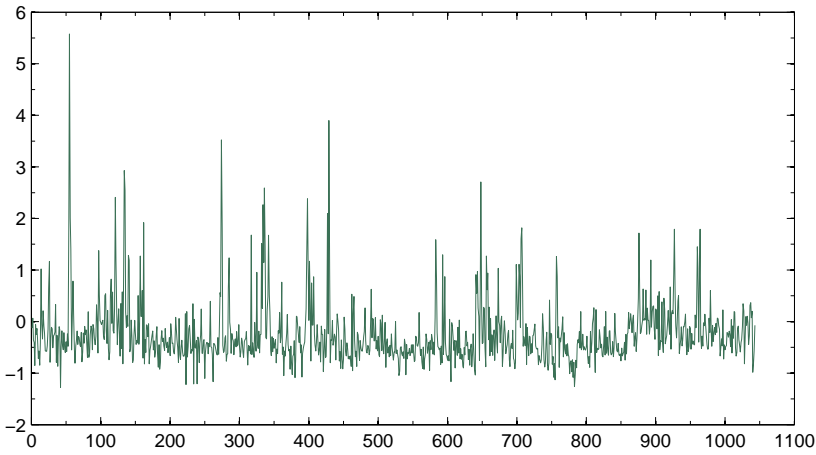


Figure 3.14: The deviation of the these two roughnesses is shown in (a). According to the statistical fitting, the absolute deviation of these two roughnesses distribute nearly follow gamma distribution, most of the values are limited from 0 to 2 m, (b). All roughness deviations are in meters.



4

Estimating glacier surface displacements in the Nyainqêntanglha Range, China from 1993 to 2015

Mountain glaciers are distributed in the transition zone between monsoon and continental climates on the Tibetan Plateau, China. Theoretically, the ice surface displacements have a large variability both in space and time. Here, we chose the entire Nyainqêntanglha Range, to the south of the Nam Co Lake, Tibetan Plateau for a case study. In this study, we monitored the ice surface displacement of these glaciers over nearly two decades from 1993 to 2015 by applying a feature-tracking method (COSI-Corr) to multi-temporal Landsat image data. The precision of the ice displacement estimates was evaluated by using measurements on the relative stable ground outside glaciers. Through the time series analysis of ice surface displacement, we found that a combination of a linear trend and the amplitude of multi-annual component of ice surface displacement is observed in most areas of these glaciers, more especially in the ablation zones. First, the long term linear trend and multi-annual variability of ice surface displacements are estimated. Second, the appropriate mean surface velocity, linear trend v and amplitude of multi-annual component a and their spatial distributions are assessed as well. Third, the correlation of v and a with elevation and slope are evaluated. The displacement observations indicate that the dominant feature of ice flow in the study area is different in the upper and lower zones of the observed glaciers. It appears that these glaciers are all active, the heterogeneous spatial patterns are identified

around all over the glacier area from low elevations and small slopes to high elevation and large slopes within the Nyainqêntanglha Range. The study demonstrates that ice surface displacements based on spaceborne optical imagery (Landsat) have potential for long term detection and understanding of glacier motions in the Nyainqêntanglha Range.

4.1. Introduction

Mountain glaciers are one of the main water reservoirs, and associated with regional climate change on the Tibetan Plateau [96]. The high altitudes of the Tibetan Plateau enhance the influence of the monsoon climate from East Asia and the Indian Ocean, while the high altitudes limit the influence of the midlatitude westerlies [21, 152]. Various glaciers are distributed in the elevated mountain ranges, such as Tien Shan, Pamirs, Karakoram, Kunlun, Nyainqêntanglha and Himalaya. According to their thermal regime, these mountain glaciers were categorized into several classes: sub-continental type, temperate type and extreme continental type [121, 122] initially. Recently, more attention has been paid to large scale remote sensing techniques (i.e. Lidar, optical imagery, gravimetry) and numerical modeling of glacier dynamics in response to regional climate. That strengthened the understanding of the inherent thermal regime of the different types of Tibetan glaciers and their response to changing climate conditions [38, 155]. However, the understanding of mechanisms determining ice mass flow in these mountain glaciers is still scarce owing to the lack of sufficient geodetic and glaciological measurements.

4.1.1. Significance of surface displacement in glacier dynamics

It is known that gravity driven basal sliding is one of the dominant controlling factors of glacier and ice sheet movement. The mechanical characteristics of glaciers depend on the temperature, their conditions and changes of those mechanical characteristics will affect ice deformation and the flow dynamics. This implies that both the thermal forcing due to the surface climate and the basal geothermal heat into the body of ice, reshape the distribution of internal temperature of ice, which consecutively result in a gradual change of the ice flow patterns. The bed topography is a more significant constraint for mountain glaciers than for ice sheets in the polar area. Except in the surging state, the displacement of a glacier is in the order of hundred of meters per year [66, 67, 121, 122]. By monitoring surface displacement, deformational and basal processes within the glaciers can be further understood. For instance, surface displacement is a moderate indicator of glacier motion under a certain climate conditions when the ice body moves at the temperate base. Alternatively, changes in glacier surface motion can be helpful to recognize the roles of melting and sliding, and spatial

assessment of these changes can be used to partition the structure of a glacier [109, 129].

4.1.2. Significance of glaciers in the Nyainqêntanglha Range

Table 4.1: The glaciological features of the eight polythermal glaciers of interest in the study area, S_t , L_t , \bar{D} , V represent the total area, the total length, the mean of the depth and the volume, respectively. These data are derived from the CGI (Chinese Glacier Inventory) and Table 3 in [19].

| | Zhadang | Panu | Lalong | Tangse No.2 | Xibu | Lisheng | Guila | Guren |
|-------------------|---------|-------|--------|-------------|-------|---------|-------|-------|
| S_t (km^2) | 2.48 | 12.88 | 10.29 | 2.96 | 23.35 | 4.4 | 14.69 | 5.6 |
| L_t (km) | 2.7 | 5.3 | 3.6 | 2.1 | 9.3 | 4.2 | 7.2 | 4.2 |
| \bar{D} (m) | 59 | 102 | 86 | 69 | 139 | 48 | 108 | 78 |
| V (km^3) | 0.15 | 1.26 | 0.64 | 0.27 | 4.39 | 0.07 | 1.59 | 0.44 |

In this study, we focus on a glaciated area on the transition between monsoon and continental climates as can be found in the Nyainqêntanglha mountain Range. Approximately 90 % of the annual precipitation occurs in summer and is the main source of glacier mass. Specifically, the accumulation and ablation of glaciers occurs simultaneously during the summer season in this region [73]. Over the past decades, fluctuations of ice motion were observed at ice masses across polar areas and mountains [115, 129]. However, the studies of long term patterns of ice motions on the Tibetan glaciers are still limited due to the high altitude and complicated environmental conditions. Since the 1950s, glaciologists have paid attention to this issue through a combination of thermometers, steam drill, and other terrestrial surveying methods. Abundant temperature data of ice bodies were recorded on various glaciers over the entire Tibetan Plateau within this long period. Vertical profiles of temperature from the surface to the bed, of the studied polythermal glaciers were measured along with the melting base and sub-freezing temperature in the upper layers [63]. A glacier inventory was gradually established using airborne, and spaceborne optical image data and topographical maps during the following decades to assess the glaciers' dynamics [122, 165]. Based on previous estimations that used Landsat TM/ETM+ scenes, the total area of all glaciers in this mountain range was 795.6 ± 22.3 km^2 until 2001 [19]. The area of some sampled glaciers (Zhadang, Tangse No. 2, Lalong, Xibu, Panu, see Fig. 4.1) decreased by -6 ± 3 % during the period of 1976–2001, while no advancing was detected for any of these sampled glaciers, their lengths decreased by about 10 m per year on average between 2001 and 2009. It was also observed that the ice cover responds to the monsoon wind and temperature fluctuations, which probably triggers glacier shrinkage within this region [19]. Details on these selected glaciers are listed in Table 4.1.

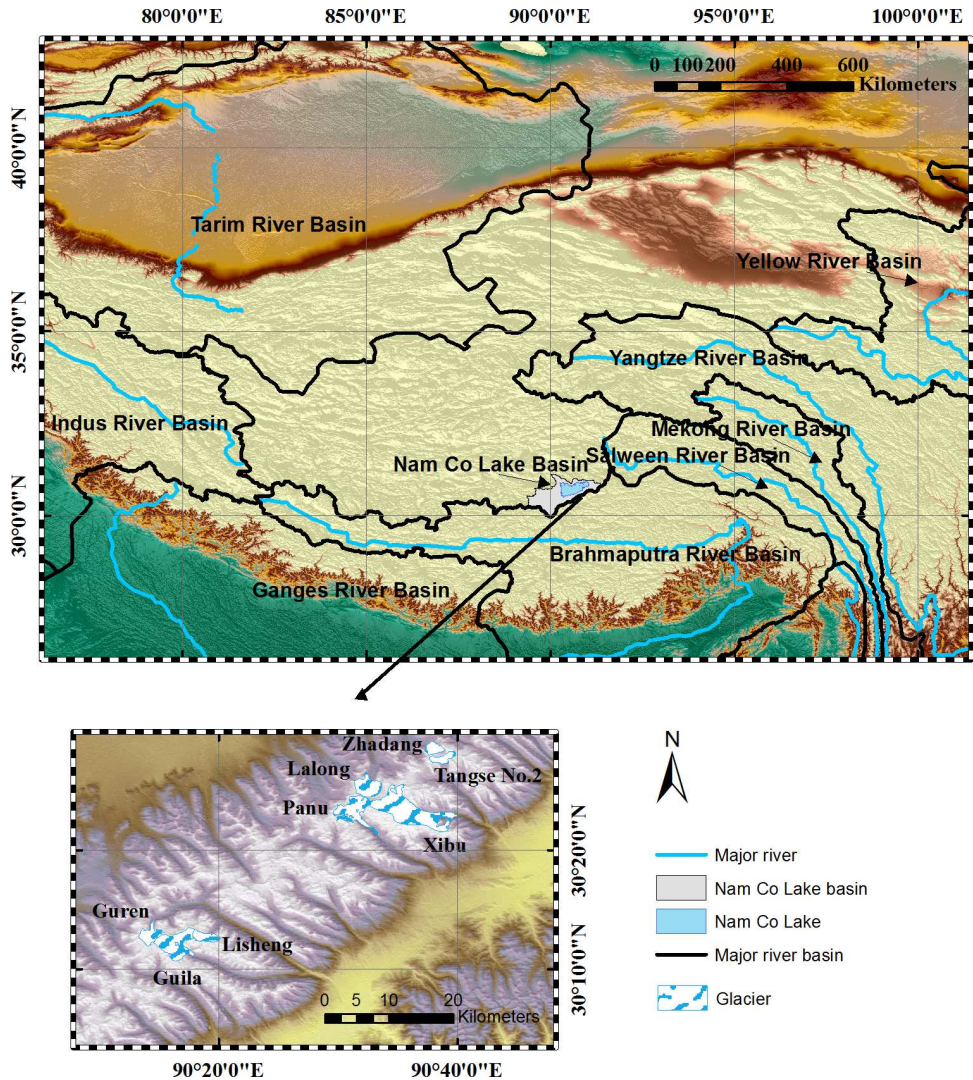


Figure 4.1: The location of the studied polythermal glaciers in the study area based on the CGI (Chinese Glacier Inventory) [19]. The color rendered relief is the elevation of the glaciated surface derived from SRTM and ASTER GDEM. Major rivers and their basin delineations are derived and adapted from the database of ICIMOD (International Center for Integrated Mountain Development).

4.2. Data Description

Table 4.2: The specifications of the Landsat scene used in this study. All scenes used in this study from path 138 and row 39.

| Acquisition date (mm/dd/yyyy) | Spacecraft platform | Sensor | Processing Level | Frame (path/row) | Cloud cover (%) |
|----------------------------------|---------------------|----------|------------------|------------------|-----------------|
| 1/14/1993 | Landsat 4 | TM | 1T | 138/039 | 10 |
| 10/8/1994 | Landsat 5 | TM | 1T | 138/039 | 1 |
| 10/13/1996 | Landsat 5 | TM | 1T | 138/039 | 17 |
| 1/1/1997 | Landsat 5 | TM | 1T | 138/039 | 18 |
| 10/30/1999 | Landsat 7 | ETM+ | 1T | 138/039 | 4 |
| 11/1/2000 | Landsat 7 | ETM+ | 1T | 138/039 | 1 |
| 12/22/2001 | Landsat 7 | ETM+ | 1T | 138/039 | 20 |
| 5/15/2002 | Landsat 7 | ETM+ | 1T | 138/039 | 18 |
| 12/20/2003 | Landsat 5 | TM | 1T | 138/039 | 28 |
| 3/25/2004 | Landsat 5 | TM | 1T | 138/039 | 16 |
| 10/9/2006 | Landsat 5 | TM | 1T | 138/039 | 19 |
| 1/13/2007 | Landsat 5 | TM | 1T | 138/039 | 25 |
| 1/16/2008 | Landsat 5 | TM | 1T | 138/039 | 16 |
| 1/18/2009 | Landsat 5 | TM | 1T | 138/039 | 26 |
| 12/23/2010 | Landsat 5 | TM | 1T | 138/039 | 18 |
| 10/7/2011 | Landsat 5 | TM | 1T | 138/039 | 17 |
| 2/1/2014 | Landsat 8 | OLI-TIRS | 1T | 138/039 | 4 |
| 3/24/2015 | Landsat 8 | OLI-TIRS | 1T | 138/039 | 7 |

As one of well-known continuous spaceborne missions, numerous good quality multi-spectral images have been acquired from Landsat satellite since 1980s. In general, the Level 1 Product Generation System (LPGS) is applied to generate the standard Landsat products [28, 146]. Since Landsat-4 was launched in 1982, the Thematic Mapper (TM), imaging spectro-radiometers of Landsat (Landsat 4, 5 and 7), have been providing multispectral imagery appropriate for many different applications [92]. However, artifacts such as the so-called memory effect (ME), scan-correlated shift (SCS), and coherent noise (CN) are degrading Landsat imagery. Radiometric and geometric calibration and correction are considered as essential procedures to remove these instrument artifacts and atmospheric path degradation from Landsat data [135]. To address these calibration and correction issues, the Level 1 Product Generation System (LPGS) is currently applied for the standard Landsat product. Initially, all the raw imageries acquired by the Landsat Ground System (LGS) from Landsat TM sensor are reformatted. The imagery data, Payload Correction Data (PCD), Mirror Scan Correction Data (MSCD), calibration data and metadata are attached together. Then, user requests for higher level products of Landsat scenes are processed through Standard Terrain Correction (Level 1T – with better precision and terrain correction) if necessary. If no ground-control or elevation data necessary for L1T correction are available, the Level 1G (with only systematic correction) or Level 1Gt

(with systematic terrain correction) is the best level of correction applied to the imageries [143]. The radiometric and geometric accuracy of Landsat data can be improved systematically by Standard Terrain Correction combining ground controls points while employing a Digital Elevation Model (DEM) in the product Level 1T. In particular, DEMs including Shuttle Radar Topography Mission (SRTM), National Elevation Dataset (NED), Canadian Digital Elevation Data (CDED), and Global 30 Arc-Second Elevation (GTOPO 30) with Ground control points from the GLS 2000 dataset guarantee the geodetic accuracy of the production. Eventually, the Landsat standard product is generated in geotiff format, at a resolution of 30 m for TM, ETM+ data after applying the Cubic Convolution (CC) resampling, projection and map (North-up) orientation procedures [28, 146]. The latest Operational Land Imager (OLI) and Thermal Infrared Sensor (TIRS) are operating on Landsat 8 which was launched in 2013. Landsat 8 extends the time span of Landsat series products to over 40 years. Therefore, the Landsat 1T product was chosen because of its better temporal and spatial coverage and high radiometric quality over the mountain range.

Here, we select the western Nyainqêntanglha Range glaciers, and the period from 1993 to 2015 for ice surface displacement analysis. This area is located on the south side of the Nam Co lake, which is the largest lake over the Tibetan Plateau. First, we examine the quality of every acquisition of the Landsat 1T product over this region by considering the possible degradation factors like cloud attenuation, radiometric and geometric properties resulting in potential mismatching, decorrelation and other bias for features—tracking [129]. Second, we assess the time interval of the single pairs (master and slave) fed for feature—tracking. In this study, we focus on deriving the annual ice speed of mountain glaciers, the adjacent acquisitions within T-1, T, T+1 (year T) are set to select for every single pair to minimize the seasonal variations and increase the frequency of similar surface condition when features—tracking is implemented [33]. Finally, 17 scenes belonging to the same frame path 138, row 39 Landsat Level 1T image products were acquired for further ice surface displacement derivation (see Table. 4.2).

4.3. Methodology

As the development of spaceborne optical datasets, feature tracking techniques are providing promising insights on ice flow dynamics. Feature-tracking methods applied to optical imagery are useful to monitor diverse ice surface displacements over a long period of time [108, 115, 117]. The core of this technique is image matching. Since the 1980s, various feature-tracking methods based on image matching were developed and tested for a number of case studies over glaciated area [129]. In earlier years, the potential of sequential spaceborne im-

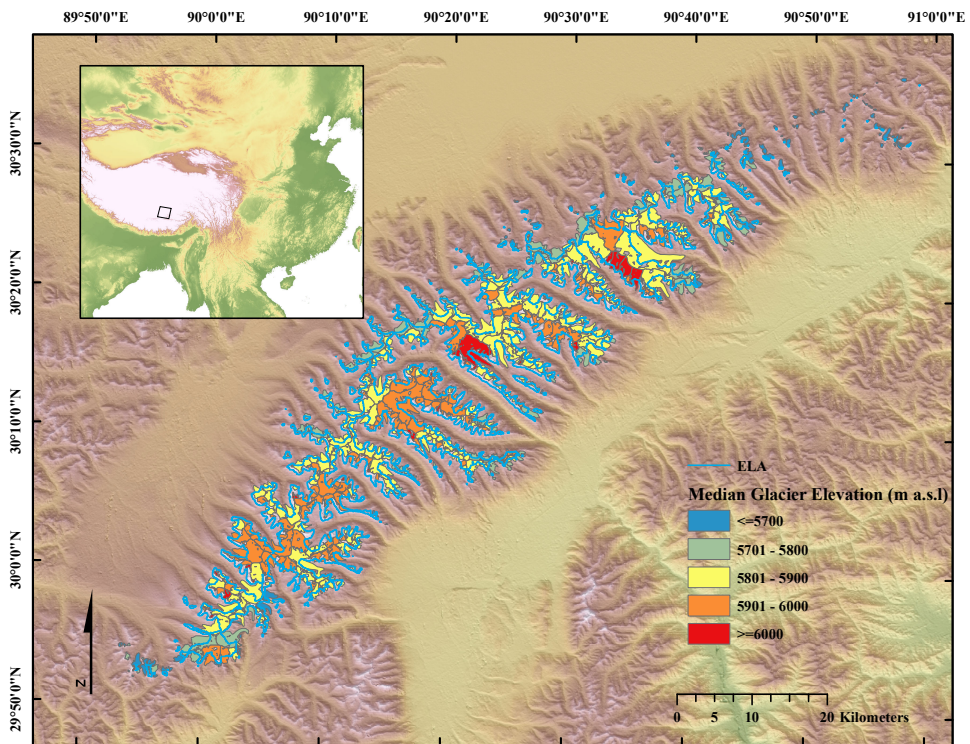


Figure 4.2: The entire spatial coverage of chosen glaciated area in the Nyainqêntanglha Range from the latest Randolph Glacier Inventory. According to median elevation of every individual glacier, all the glaciated area can be classified into 5 groups. The bold blue line indicates the proxy of ELA (Equilibrium Line Altitudes) [Wu et al.] to identify the ablation and accumulation approximately.

ages was described for studying the ice shelf and glaciers of Antarctica [40, 89]. Then, normalized cross-correlation feature tracking was developed to estimate the speed of ice flow in the polar and other regions [17, 115]. In this method, the features are limited in a rectangular window. These differences improve accuracy of displacement from the pixel size to better resolution and higher quality of the final speed measurements [83]. This algorithm was adapted for ice speed and surge dynamic studies on the Tibetan Plateau [31, 108, 110]. Inspired by this algorithm, various feature-tracking methods were developed. Some of them apply least squares matching and cross-correlation in the spatial domain, while others are implemented in the frequency domain [129]. Here, we choose the feature-tracking methods developed by Leprince et al. [82], whose emphasis is not only on the orthorectification and the coregistration of pairs of repeated images, but who also introduced a specific phase correlation algorithm. The phase difference estimation of this method is implemented in the frequency domain. The moving window size of this method is smaller than for most other methods, which is probably more suitable for rough ice surfaces (crevasses, debris covered parts etc.). Recently, a number of studies are widely applied for the Tibetan glaciers dynamics, such as for surge behavior of glaciers in the Karakoram mountain range and variations of Himalayan types glaciers [33, 109, 116–118].

4.3.1. Displacement derivation

In this study, the phase-correlation based feature-tracking method (COSI-Corr) is used. All the main orthorectification and correlation procedures are implemented in the software package (COSI-Corr, written primarily in IDL). Here, the orthorectified Landsat images are used as input to the COSI-Corr for correlation detection. During each displacement derivation, the overlapping part of the two images is prepared for correlation detection in the Fourier domain. Here, we assume io_m and io_s as the original master image and the shifted version of the master image (slave), which differ by a relative displacement (Δ_x, Δ_y) , thus

$$io_m(x, y) = io_s(x - \Delta_x, y - \Delta_y) \quad (4.1)$$

According to the Fourier shift theorem [82], we deduce the relation between the Fourier transforms I_m, I_s of the original images io_m and io_s , as below

$$I_m(\omega_x, \omega_y) = I_s(\omega_x, \omega_y) e^{-j(\omega_x \Delta_x + \omega_y \Delta_y)} \quad (4.2)$$

ω_x – the frequency variable in column;

ω_y – the frequency variable in row.

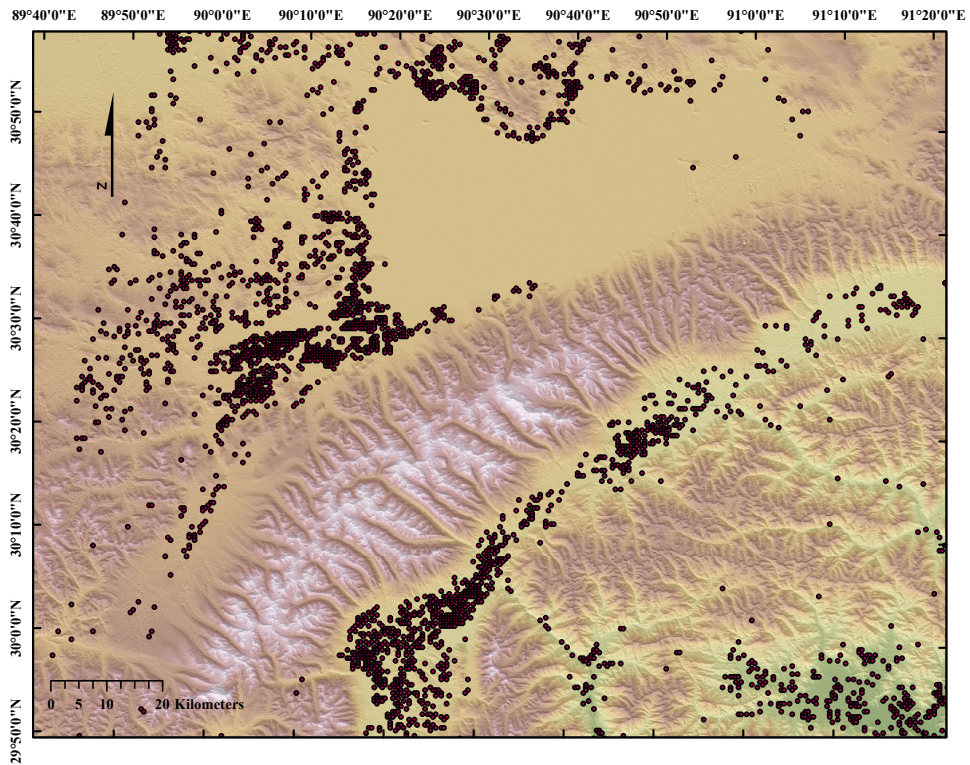


Figure 4.3: An overview of the chosen reference displacements according the selecting procedures on the stable ground.

When * refers to the complex conjugate, the normalized cross-spectrum of the original images i_{o_m} and i_{o_s} can be written as

$$C_{i_m, i_s}(\omega_x, \omega_y) = \frac{I_m(\omega_x, \omega_y) I_s^*(\omega_x, \omega_y)}{|I_m(\omega_x, \omega_y) I_s^*(\omega_x, \omega_y)|} = e^{j(\omega_x \Delta_x + \omega_y \Delta_y)} \quad (4.3)$$

Then the displacement of these two imageries (master, and slave) can be derived by measuring the phase difference of each imagery's Fourier transform within the sliding correlation window by starting from upper-left corner of the scene. Alternatively, it can be demonstrated that the 2-D slope of the cross-spectrum's phase is a good estimation of the displacement of the two correlated imageries.

4.3.2. Post-processing and precision assessment

To assess the quality of the derived surface displacements, several error sources will be clarified at first. The uncertainty of orthorectification, the imagery-to-imagery registration imperfection of used Landsat scenes, and the bias of correlation methods are primarily affecting the estimation of the displacements. For instance, additional erroneous horizontal shifts can be introduced during the orthorectification. These horizontal shifts are not coincident with real horizontal displacements, but related to errors, such as inappropriate systematic information (camera position, look direction or lens distortions), atmospheric effects, and errors in the digital elevation model (DEM). When inaccurate DEMs are utilized for the imagery-orthorectification, the DEM errors will affect horizontal shifts owing to the elevation change, and the horizontal displacements will not be influenced. According to previous studies, the imagery-to-imagery registration will result in small uncertainties of Landsat imageries (ETM+ is about 5 m, TM is about 6 m) [79, 126]. Additionally, some decorrelations will exist due to the surface elevation change during the matching procedure. Therefore, the matched Landsat scenes are acquired from the same path and row (138/39) to minimize the DEM errors in the processing chain of displacements [129]. Other systematic, terrain-induced errors are corrected due to the specifications of the Landsat L1T products used here [28].

Outlier detection procedure

Displacements in east/west (E/W), north/south (N/S) and the quality of correlation index (SNR) are derived and stored as three bands in one formatted image file. Next, we examine whether mismatches, outliers and gaps exist in the scene. Preliminarily, the decorrelation area is culled out on the basis of the extreme values of displacements. However, we find that the pure filtering of the

invalid and low quality displacement estimates reduce the variability of meaningful information in the derived displacements as well. In particular, it leads to discontinuities in displacement times series and spatial distributions on parts of the studied glaciers, which undermines the estimation of the related temporal and spatial variability analysis. According to our statistics, i.e. the mean SNR in each derived displacement map, values larger than 0.60, are assumed to be acceptable. Remaining displacements are fed to further displacement variability (ice speed) analysis (see Section 4.3.3).

Precision assessment and uncertainty

To refine the quality of displacements and improve their consistency, we use the medians of the displacement observations for further processing. Compared to the mean of the observations, the median is not sensitive to the presence of noise. For instance, the mean value will increase to infinite when some infinite values (e.g. NaN-no data) exist in the pixels. In contrast, the median remains insensitive with respect to this sort of outliers. In image processing, the median operator is often used as a nonlinear operator to reduce raw image noise. Here, we apply the median operator within a 3×3 moving window, considering the complexity of the glaciated terrain and the potential loss of image resolution in the displacement map. Next, displacements are categorized as belonging within or outside (the stable ground) a glacier region. This setting is chosen by using glacier outlines from the Randolph Glacier Inventory [104] (see Fig. 4.3).

Here, we assume that terrain outside glacier areas is stable, which implicitly corresponds to a zero-displacement at time scale. However, the displacements in the assumed stable area are attenuated by localized geo-environmental influence and errors propagated from the processing chain. Thus, the uncertainty of displacements in the stable area is assumed to be an appropriate reference to assess the precision of derived displacement for each acquisition.

First, we estimate the uncertainty of displacements on the stable ground by using temporal deramping (remove a linear trend) of observation time series. Second, the average of residuals of all points within the stable ground is calculated with respect to the possible uncertainty of derived displacements by using the feature tracking method. Hereafter, the uncertainty of displacements at the k -th acquisition is estimated as

$$\underline{\hat{e}}^k = \frac{1}{N} \sum_{i=1}^N \underline{\hat{e}}_i^k, \forall k \quad (4.4)$$

where i is the number of displacement and $\underline{\hat{e}}_i^k$ is the residual of the i -th point after removing the linear trend at the k -th displacement [29]. All the displace-

ments after correcting by this uncertainty at the k th acquisition are expressed as

$$D_i^{k'} = D_i^k - \underline{\hat{e}}_i^k, \forall i \quad (4.5)$$

The corrected displacement time-series $D_i^{k'}$ will be used in the following variability analysis in Section 4.3.3.

4.3.3. Displacement variability estimation

According to a previous glaciological study in the Nyainqêntanglha Range mentioned in Section 4.1.2, relevant surveys of ice dynamics are sparse. It is difficult to acquire historical records and references on the magnitude of ice surface displacement D and linear trend v in long time series corresponding to our research period and spatial coverage. In conventional geodetic theory, the mathematical model is predefined and observations are repetitively sampled to minimize residuals compared with the model [11–13]. At the same time, the quality of observations can be biased by potential measurement errors propagated in the processing chain. All the quality controls facilitating the potential rejection of the null hypothesis, can be assessed appropriately when an a-priori mathematical model is designed [14]. Consequently, the form of the mathematical model is constrained by the quality of valid observations. In other words, the parameterization of the chosen mathematical model can be dependent on the fluctuation of the observations as well.

In this study, we expect to estimate the variation of ice surface displacement between 1993 and 2015. Based on the image pair selections criteria and processing described in Section 5.2.1, and 4.3.2–4.3.2, 17 displacements are retrieved in this period of time on the glaciated area. The least squares approach is applied to assess whether the displacement varies with time t during this period (see Table 4.2). Considering the validity of the observation time series, we are mainly interested in whether there is an increasing or decreasing linear trend in retrieved ice surface displacements and the designed mathematical model is expressed as

$$E\{D\} = A x; \quad D\{D\} = Q_{DD} \quad (4.6)$$

$m \times 1$ $m \times n$ $n \times 1$ $m \times m$

$$A = \begin{pmatrix} 1 & t_1 & \sin(\frac{2\pi t_1}{T_D}) & \cos(\frac{2\pi t_1}{T_D}) \\ 1 & t_2 & \sin(\frac{2\pi t_2}{T_D}) & \cos(\frac{2\pi t_2}{T_D}) \\ \dots & \dots & \dots & \dots \\ 1 & t_m & \sin(\frac{2\pi t_m}{T_D}) & \cos(\frac{2\pi t_m}{T_D}) \end{pmatrix} \quad (4.7)$$

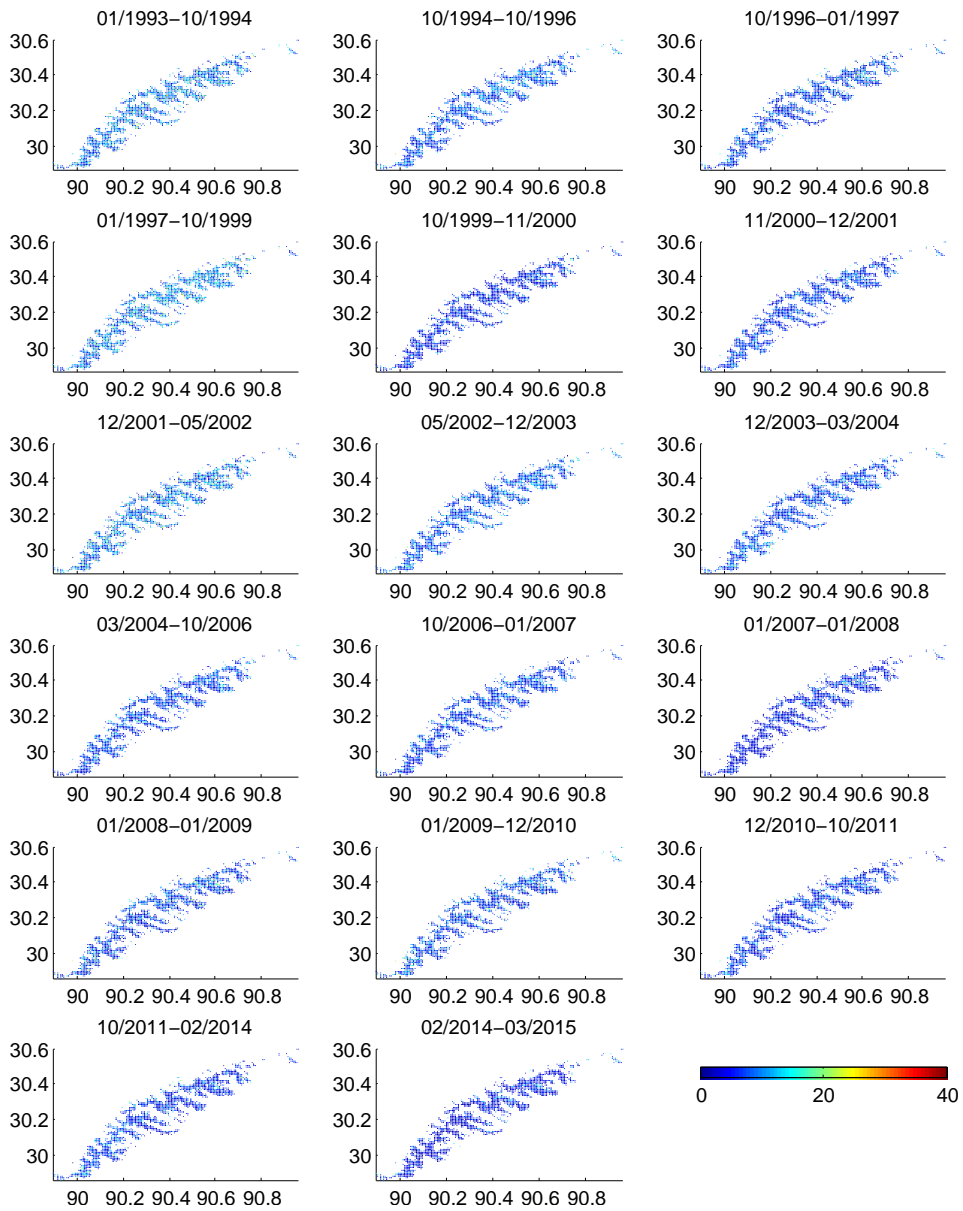


Figure 4.4: The surface displacements (unit: m) between two adjacent temporal acquisitions within the glaciated area from 1993 to 2015.

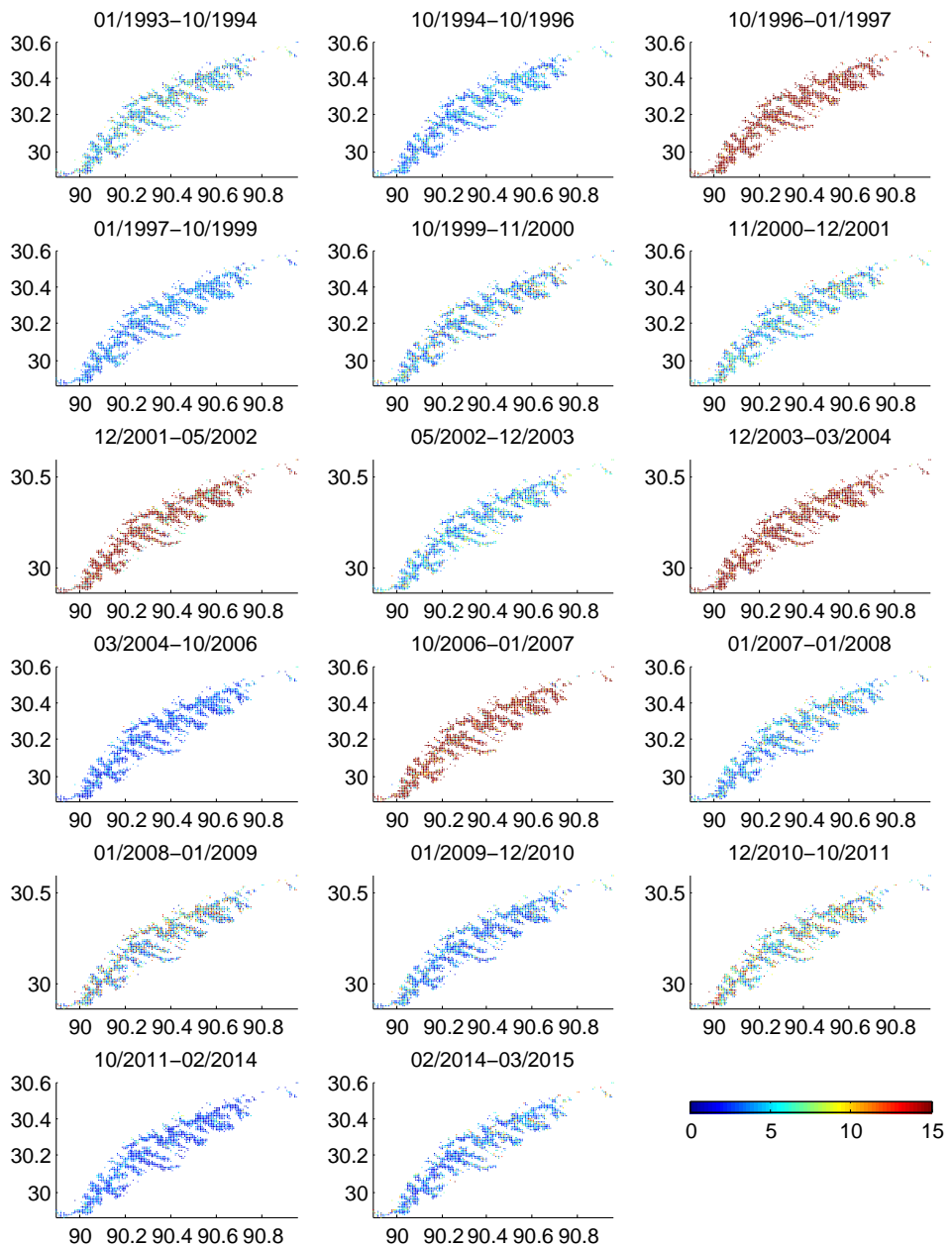


Figure 4.5: The mean surface velocities (unit: m/a) between two adjacent temporal acquisitions within the glaciated area from 1993 to 2015.

where A is the design matrix, t is the time of acquisition of a Landsat scene (unit: year), m is the number of ice surface displacement observations \underline{D} from 1993 to 2015. T_D represents the period of the periodic component of ice surface displacements. As mentioned, 17 Landsat scenes are chosen within ~ 20 years temporal coverage. Based on the number of observations, the periodic variability of ice surface displacements can be specified as the amplitude of periodic component. When fitting procedure is implemented for every pixel, T_D is set to be a flexible value from 1 year up to 20 years. The observation equations can be expressed as $\underline{D} = Ax + \underline{e}_0$. Here \underline{e}_0 represents the residuals between the linear model and the observations. Q_{DD} is the stochastic model of the observations.

Once the unknown parameters $x = [v \ a_s \ a_c \ c]^T$ (linear trend v and constant coefficient c , coefficients a_s and a_c) are used to estimate periodic ice speed with amplitude $a = \sqrt{a_s^2 + a_c^2}$, the goodness of these estimates needs to be assessed in the term of precision. The precision of estimated parameters is given by

$$Q_{\hat{x}\hat{x}} = (A^T Q_{DD}^{-1} A)^{-1} \quad (4.8)$$

Then, the precision of the adjusted observations is

$$Q_{\hat{D}\hat{D}} = A Q_{\hat{x}\hat{x}} A^T \quad (4.9)$$

and the precision of the least-squares corrections is

$$Q_{\hat{e}\hat{e}} = Q_{DD} - Q_{\hat{D}\hat{D}} \quad (4.10)$$

where the residual $\hat{e} = D - \hat{D}$ and $\hat{D} = A\hat{x}$.

In the end, we calculated a test statistic \underline{T}_q with a chi-squared distribution $\chi^2(q, \lambda)$. And \underline{T}_q can be reduced to

$$\underline{T}_q = \frac{\hat{e}_0^T Q_{DD}^{-1} \hat{e}_0}{m - n}, \quad (4.11)$$

where n is the number of unknown parameters, \hat{e}_0 is the residual between the predefined model and real displacement observations, and $q = m - n$ denotes the degrees of freedom. Through test procedure, the optimal unknown parameters are determined to describe the long term linear trend and amplitude of periodic component of ice surface displacement in the Nyainqêntanglha Range.

4.4. Results

In this section, we apply the proposed procedures to estimate the ice displacements and their variabilities using a set of Landsat scenes (in the 138/39 frame) covering the glaciated area from 1993 to 2015. In the feature tracking procedure,

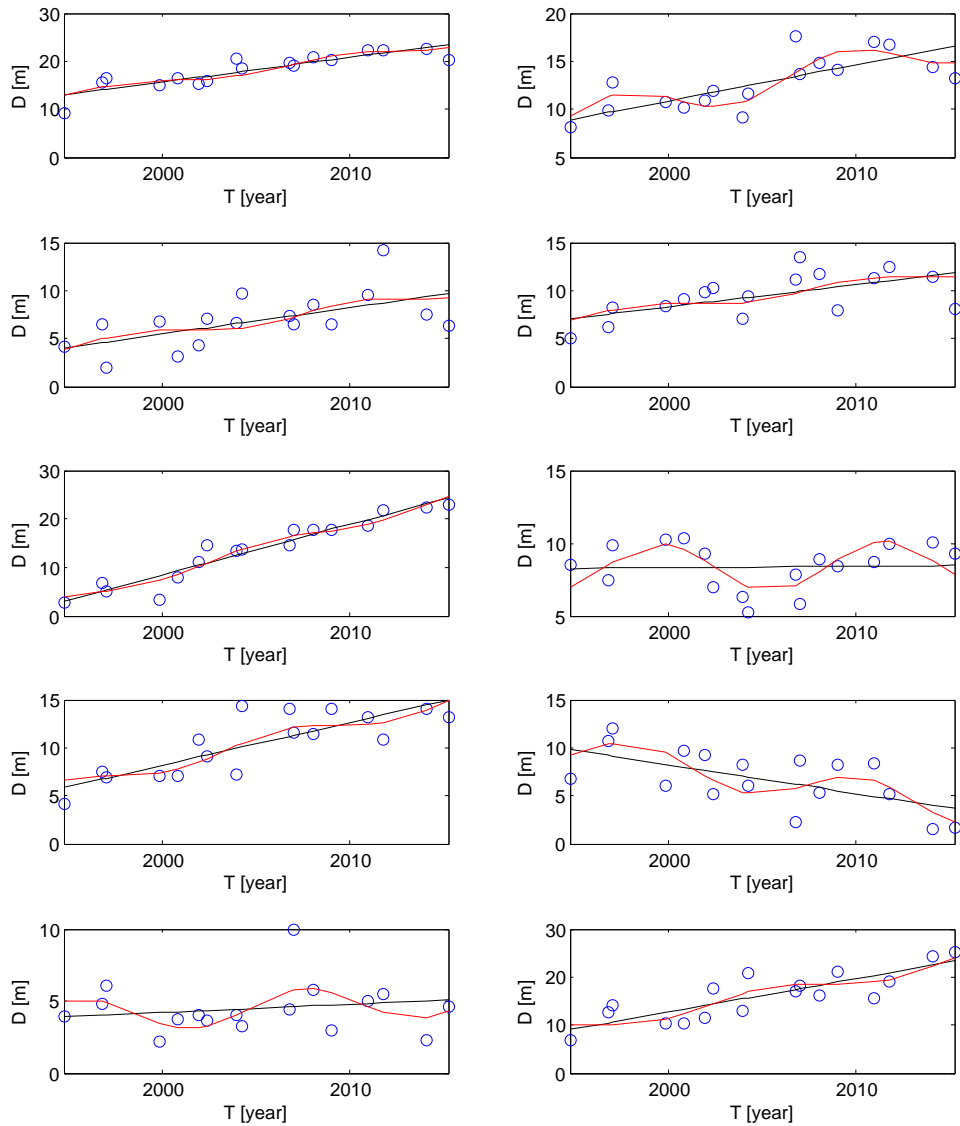


Figure 4.6: The fitting results of ice surface displacement in 10 random examples within the glaciated area from 1993 to 2015. The blue circles are the ice surface displacement observations, blue line is fitting curve and black line is the linear component of fitting.

multiple masters are selected based on the closest temporal Landsat scene between adjacent years (up to 3 years). The glaciated area is delineated according to the Randolph Glacier Inventory (see Fig. 4.2). For the 17 displacement maps (including N/S and E/W directions), ~ 2800 measurements per map within glacier outlines are derived by the feature tacking procedure. According to the filtering procedure, all the measurements are limited by using > 0.6 (median SNR) and a data range between -30 m and $+30$ m both in N/S and E/W to minimize noise and erroneous sampling. Then the filtered time series of displacements are used to assess their temporal variability (see Figs. 4.4 and 4.5).

By using the model Eq. 4.6 and 4.7, \underline{D} is a set of displacement observations at each acquisition. With this observation vector, the least squares approach is applied. Linear component (with linear trend ν) and multi-annual component (with amplitude a) are estimated for every single pixel in the time series within the glaciated area. Next, the quality of the least squares estimates is evaluated by the chi-square test statistic T_q . Fig. 4.6 shows some examples of fitting of time series for some pixels. These examples illustrate the capability of the applied procedure to fit different signals.

To analyze the spatial patterns of the linear component (with linear trend ν) and multi-annual component (with amplitude a), all the results are binned into 10 classes ($-\infty, 5500$ m], (5500 m, 5600 m], (5600 m, 5700 m], (5700 m, 5800 m], (5800 m, 5900 m], (5900 m, 6000 m], (6000 m, 6100 m], (6100 m, 6200 m], (6200 m, 6300 m], (6300 m, $+\infty$] according to the median elevations of the sampled glaciers in the Nyainqêntanglha Range (see Fig. 4.7).

The linear trend ν over the entire glaciers, i.e. including both accumulation and ablation zones, appears to have limited spatial variability over 1993–2015 (Fig. 4.8). Except for the lower parts of glacier ablation zones, e.g. in the Xibu Glacier ($\sim [5196$ m, 7086 m] of on the southern side of the Nyainqêntanglha Range), the rest of ν remains relatively consistent (~ 1 m/a) in terms of the median value for every elevation class. In other words, it shows that linear trend ν varies within a range ($\sim 0.5, \sim 1.5$) m/a in most of the glaciers, while ν of the upper part of glacier is relatively smaller than value of the lower elevated zones. The results of ν indicate that the long term linear trend of ice surface displacements seems more or less consistent, and differences are only observed when comparing the very low elevated ablation zone with the very high accumulation zone. And it seems to be that the response of glacier behaviors to the long term regional climate signal is a gradual process in terms of ice surface displacements.

The multi-annual amplitude a appears to have a larger spatial variability than the linear trend ν (see Fig. 4.8). An elevation-dependent pattern is observed for the multi-annual amplitude with larger dispersion from upper to lower area on these glaciers. Analyzing the multi-annual amplitudes at different elevations

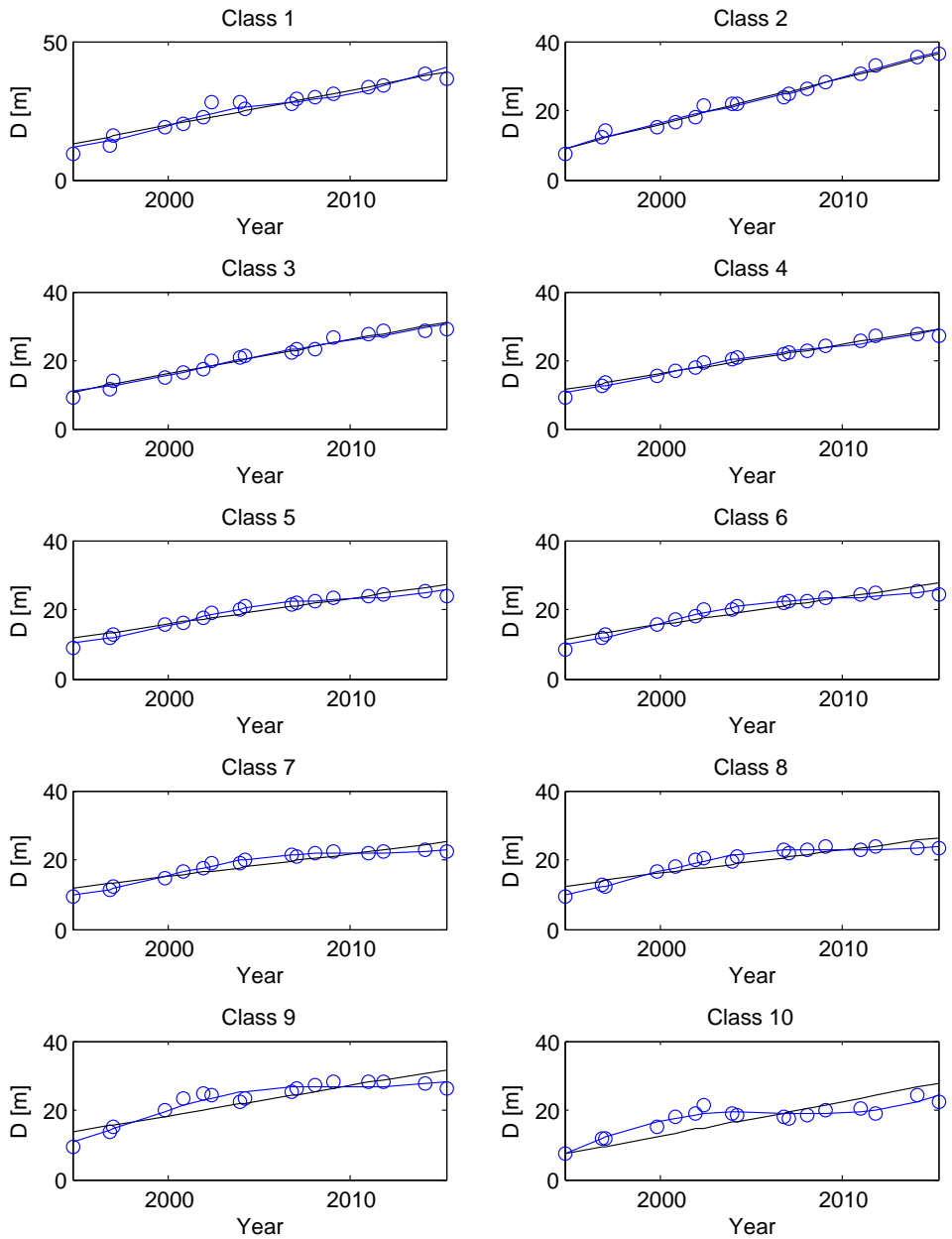


Figure 4.7: The fitting results of ice surface displacement in 10 dem-based classes within the glaciated area from 1993 to 2015. The blue circles are the ice surface displacement observations, blue line is fitting curve and black line is the linear component of fitting.

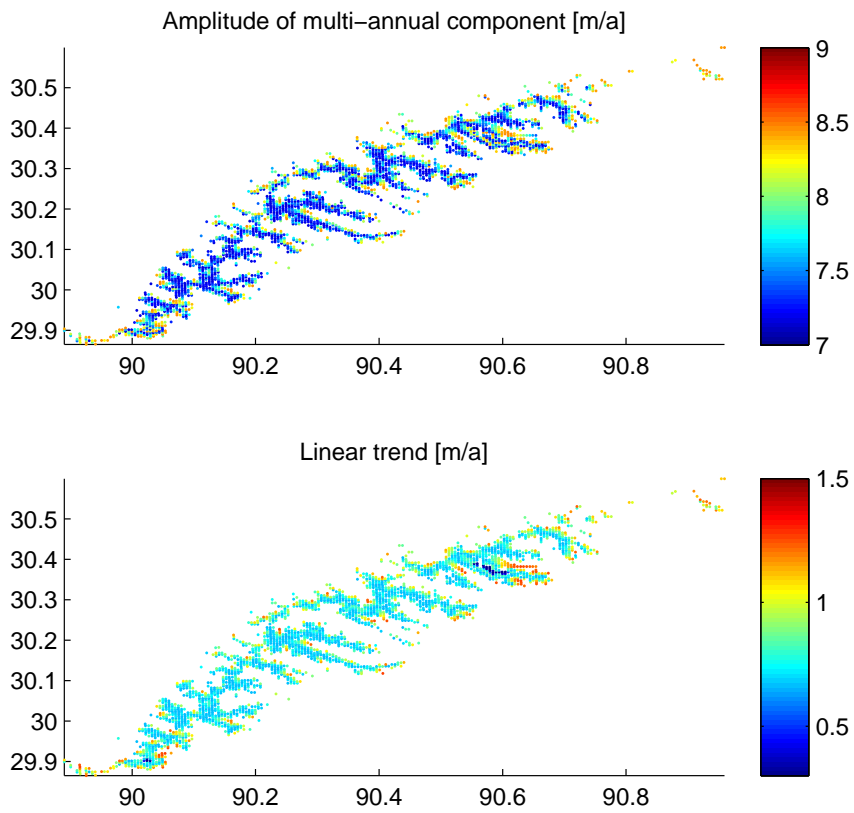


Figure 4.8: The amplitude of multi-annual component and linear trend of ice surface displacement from 1993 to 2015.

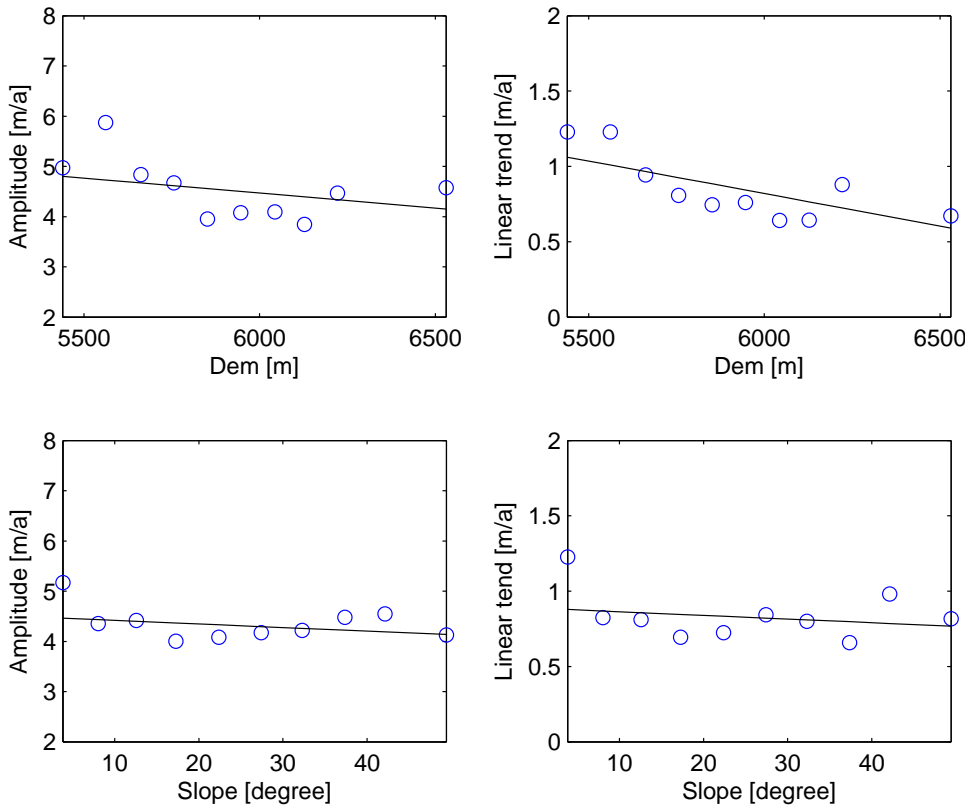


Figure 4.9: The linear trend and amplitude of multi-annual component of ice surface displacement vs surface elevation and slope classes from 1993 to 2015.

reveals varying ice flow within either the accumulation or ablation zones of the glaciers from ~ 2 m/a to ~ 10 m/a (Fig. 4.8). It is found that multi-annual amplitude decreases with the elevation. In particular, a plot shows that the multi-annual amplitude varies with elevations and slopes sampled by ASTERGDEM with lower values in glaciers at high altitudes than glaciers at lower altitudes (Fig. 4.9). The analysis indicates that the spatial variability of glacier surface displacement multi-annual amplitude seems to be more dependent on elevations and slopes in the Nyainqêntanglha Range. The results suggest that the temporal and spatial variability of ice surface displacement is related to elevations and slopes (see Figs. 4.9, 4.10 and 4.11).

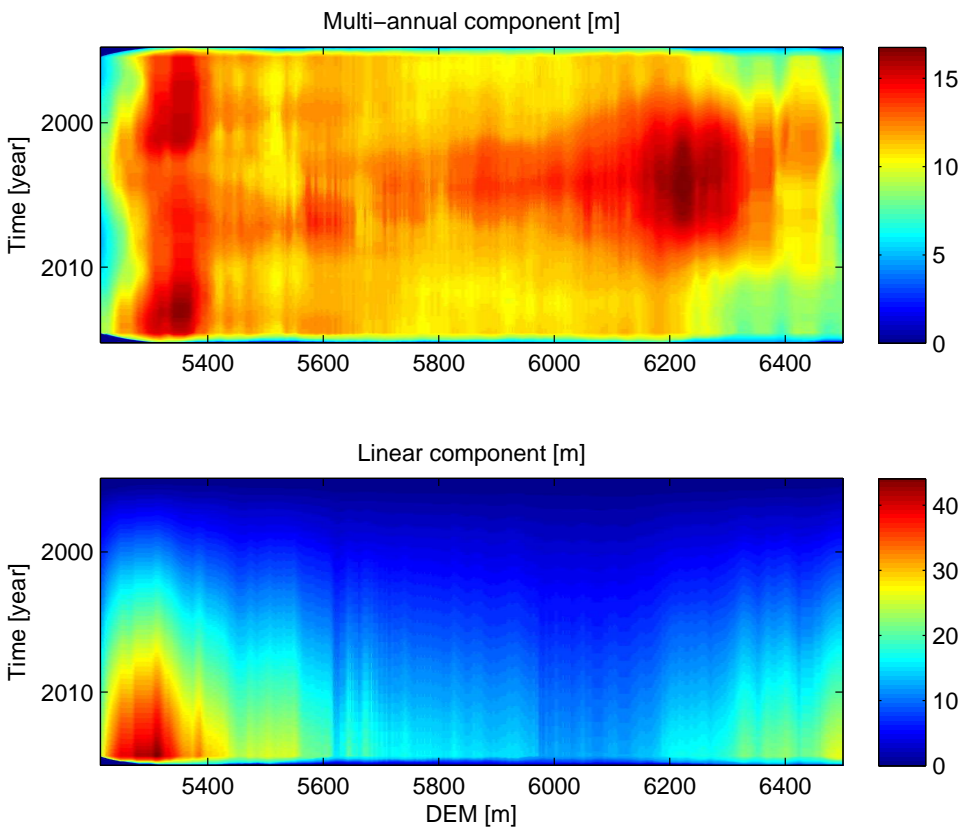


Figure 4.10: The linear component and multi-annual component of ice surface displacement with elevations from 1993 to 2015. For detailed information, see Section 4.3.3.

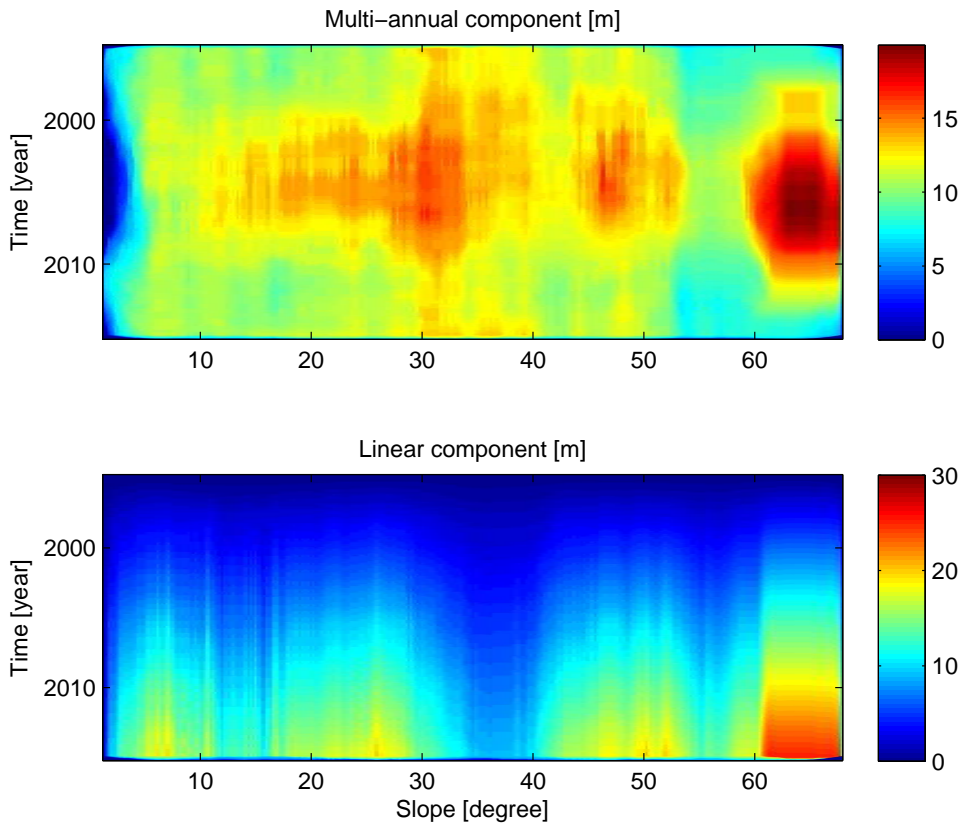


Figure 4.11: The linear component and multi-annual component of ice surface displacement with slopes from 1993 to 2015. For detailed information, see Section 4.3.3.

4.5. Discussion

The derived ice surface displacements in this study show that the combination of the COSI-Corr method and Landsat images provides meaningful estimates of surface movement in the mountainous glaciers in the Nyainqêntanglha Range. At the same time, several considerations of using COSI-Corr and Landsat imageries are also addressed regarding the quality assessment of the final displacement results. First, as Landsat satellites operate a whisk-broom scanning system, possible system errors are different from a normal push-broom system (e.g. ASTER) implemented in the COSI-Corr. The used Landsat TM images are processed at Level 1T, i.e. both radiometric and geometric corrections are applied. In addition, the cloud coverage of each individual scene should be considered as well, the larger the cloud cover, the less reliable the results are. The scenes used in this study all have cloud cover < 30%. Second, the high SNR indicate that the radiometric noise is minimized by the standard processing chain of the Landsat Level 1T product, thus the noise level on valid measurements is also reduced, which makes the correlation procedure more accurate. In other words, the lower radiometric noise of raw images results in the better correlation results by COSI-Corr. Third, there are still errors remaining in the raw displacement results (both in E/W and N/S directions) after the correlation procedure. In this study, we calculate the displacements on the stable ground. It is assumed to be out of glaciated area and follow the null hypothesis (which states that the ground does not displace temporally within the stable areas). First, ~ 2000 measurements are selected out of the glaciated area, their average slope being less than 5°. Second, the pixels are filtered out based on their SNR values being less than 0.6. The remaining pixels are applied to model the time series.

Compared with other similar glaciology works [33, 108, 117, 129], our study area (Nyainqêntanglha Range) is characterized by a more complex topographic and climatological forcing than other areas in the Qinghai-Tibetan Plateau. Due to the unique regional climate regimes in the Nyainqêntanglha Range, our first estimates of large scale ice surface displacements and variability in the mountain glaciers within this area will be useful for further studies on the response to climate forcing (see Chapter 5).

4.6. Conclusions

This study shows a first insights on the ice surface motion of the Nyainqêntanglha glaciers, where valid long term in situ-measurements are still limited. The raw ice surface displacements in (E/W and N/S directions) are obtained by using a phase correlation based feature-tracking method (COSI-Corr) with Landsat Level 1T data. Then, the post-processing (e.g. appropriate outliers detection and

displacement variability estimation) was applied to reduce noise and bias existing in the final displacement measurements on the mountainous glaciers. Consequently, we could estimate the spatial patterns and temporal variability of ice surface displacements during 1993–2015. First, the long term linear trend and multi-annual periodic component of ice surface displacements are assessed by applying a design model. This gave maps of the linear trend ν and amplitude of multi-annual component a . Then, the dependence of ν and a on elevation and slope were analyzed and the linear dependence is evaluated. All the displacement observations indicate that the dominant factor of ice flow in the studied area is different in the upper and lower zones of the observed glaciers. It is clear that these glaciers are all active, the heterogeneous spatial patterns are identified around all over the glaciers from low elevations and small slopes to high elevation and large slopes within the Nyainqêntanglha Range. In Chapter 5 we will attempt to relate the observed glacier surface flow dynamics to climate forcing.

5

Response of glacier flow to precipitation and land surface temperature, Nyainqêntanglha Range

The climatic variables are the influential factors which determine mass and energy balance of the glaciers in the Nyainqêntanglha Range, Tibetan Plateau. The impact of the fluctuation of local hydro-thermal condition on the glacier dynamics is still not well understood. In this study, the glacier response to climate has been studied by observing glacier surface displacements using Landsat image data. The linear trend and amplitude of the multi-annual component of glacier surface displacements have been related to precipitation and surface temperature. To characterize local climate forcing in the Nyainqêntanglha Range, we have used the MODIS land surface temperature and TRMM precipitation data products from 2000 to 2015. First, the temporal pattern of regional climate, i.e. the prevailing climate in different seasons is evaluated in terms of precipitation and temperature. Most of the precipitation and higher land surface temperature (both daytime and nighttime) are measured in the summer season while it is cooler and drier in the non-monsoon season. Different temporal patterns (i.e. monthly, annual and multi-yearly) of precipitation and land surface temperature have been identified. The hydro-thermal forcing of the summer-accumulation type glaciers is documented. The pre-monsoon, monsoon, post-monsoon and winter seasons have been identified depending on the temporal variability of precipitation in one full annual cycle firstly. Second, the dependence of glacier surface displacements

on precipitation and temperature has been estimated by multi-regression analysis. The time series of observed glacier surface displacements were fitted by using the period = 7.5 years. The same approach was applied to time series of TRMM and MODIS and in-situ measurements of precipitation and temperature. It implied that both the linear trend and the amplitude of the multi-annual component vary with elevation and slope. It has been found that the multi-annual component of precipitation and surface temperature has a shorter period than ice surface flow velocity. This suggested that the behavior of ice flow relates to the glacier self-adjustment in response to regional climate forcing, i.e. temperature and precipitation.

5.1. Introduction

Mountain glaciers and ice caps are considered as particularly sensitive indicators of climate change. Their contribution to the future sea level rise is projected to be one-third (about 0.07~0.17 m) of the total increase in this century [125]. Furthermore, the current increment of sea level has been estimated to be $0.41 \pm 0.08 \text{ mm a}^{-1}$ using monthly GRACE product in the period 2003–2010 [70]. Moreover, significant changes in the massive glaciers on the Tibetan Plateau have been observed by Gardelle et al. [50, 51], Kääb et al. [71], Vincent et al. [134]. These evidences indicate that mountain glaciers of different regions on the Tibetan Plateau respond to their local climatic forcing [155].

As regards glacial mechanisms, the propagation of surface melt-water into the englacial and subglacial system can contribute to the spatial and temporal variability of the glacier surface displacement [33]. On one hand, the processes determining the mass balance of upper glacier layers, i.e. precipitation, sublimation, melting (highly related to temperature changes), runoff, the erosion and sublimation of the drifting snow, also contribute to determine the pattern of surface displacements on the glaciers. On the other hand, glacier changes respond to local climate, in particular to precipitation and surface temperature. Eventually, the regional patterns of Tibetan glacier changes respond to the Indian monsoon, East-Asian monsoon and mid-latitude westerlies in some subregions of the plateau [78, 85, 87]. Specifically, some studies have found that the influence of precipitation and surface temperature, is more diversified than generally appreciated [31, 57, 68, 110, 119]. First, snow – melting on a glacier surface reduces the albedo and increases net radiation, thus inducing further melting and eventual ablation from the glacier. Second, the absorption of heat at the glacier surface will lead to increasing surface temperature which not only extends the melting period, but also reduces the accumulation on the glacier [46]. On the other hand higher surface temperature tends to increase sensible flux, while latent heat flux increases due to the presence of liquid water on the glacier surface. He et al.

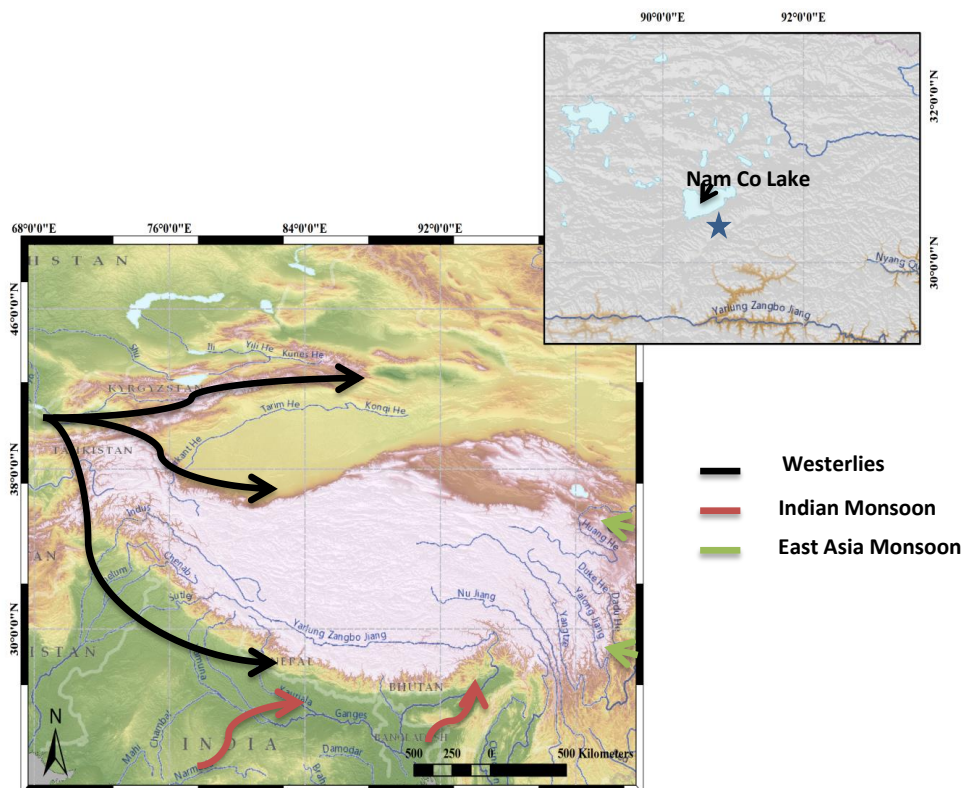


Figure 5.1: The region of interest is chosen for this patterns analysis of glacier surface displacements (Nyainqêntanglha Range) under the specific regional climate. The dominant regional atmospheric circulations are shown here.

[56], Li and Yanai [84], Ye and Wu [157] have suggested that the sensible heat flux dominates heat dissipation of the Tibetan Plateau especially before the monsoon season. This inherently heterogeneous patterns of land-atmosphere energy flows imply a significant spatial variability in the energy balance at glacier surface [15, 62, 96, 112]. For instance, no liquid precipitation and no melting occurs at lower surface temperature. At the same time, the increase of the surface albedo due to the snowcover, reduces net radiation and the total amount of heat to be dissipated as sensible and latent heat. The land surface moisture is increased by the melting process, while the sublimation and evaporation process further cool the land surface. Change in snowcover on the Tibetan Plateau weakens the land-sea thermal gradient in the winter time, induce changes in the pattern of surface temperature, heat and vapour land – atmosphere exchange, with an associated disturbance of monsoon rainfall in the successive summer season [16, 44, 55, 59].

In other words, the glacier behaviour on the TP (Tibetan Plateau) can be categorized by observing the accumulation and ablation patterns, determined by the temporal and spatial variability of the precipitation and surface temperature. In this study, the Nyainqêntanglha range, which is located in the transition area from moist to continental climate, is chosen as the region of interest (see Fig. 5.1). It is an ideal place to study the behaviour of mountain glaciers under the impact of both the summer monsoon and westerlies. However, the spatio-temporal patterns of regional climate and their changes are still not quantified due to the sparse in situ measurements in the mountain range and surroundings. Automatic Weather Stations (AWS) are scarce and confined to lower altitudes and literature documents conflicting opinions about the suitability of AWS to sample high mountain climate within this area [93, 95]. Here, we evaluate the glacier response to climate by observing the patterns of surface displacements on these mountain glaciers in response to observed patterns of precipitation and land surface temperature in different seasons. The monthly land surface temperature (LST) product from MODIS and precipitation from Tropical Rainfall Monitoring Mission (TRMM) have been used. The aim of this study is summarized follows:

- (1) characterize regional climatology in terms of surface temperature and precipitation within the Nyainqêntanglha range from monthly to multi-annual time scales.

- (2) derive the time series of mountain glacier surface displacements by using Landsat imageries and, quantify their spatial and temporal patterns.

- (3) analyze and interpret the observed temporal patterns of glacier surface displacements in response to precipitation and surface temperature.

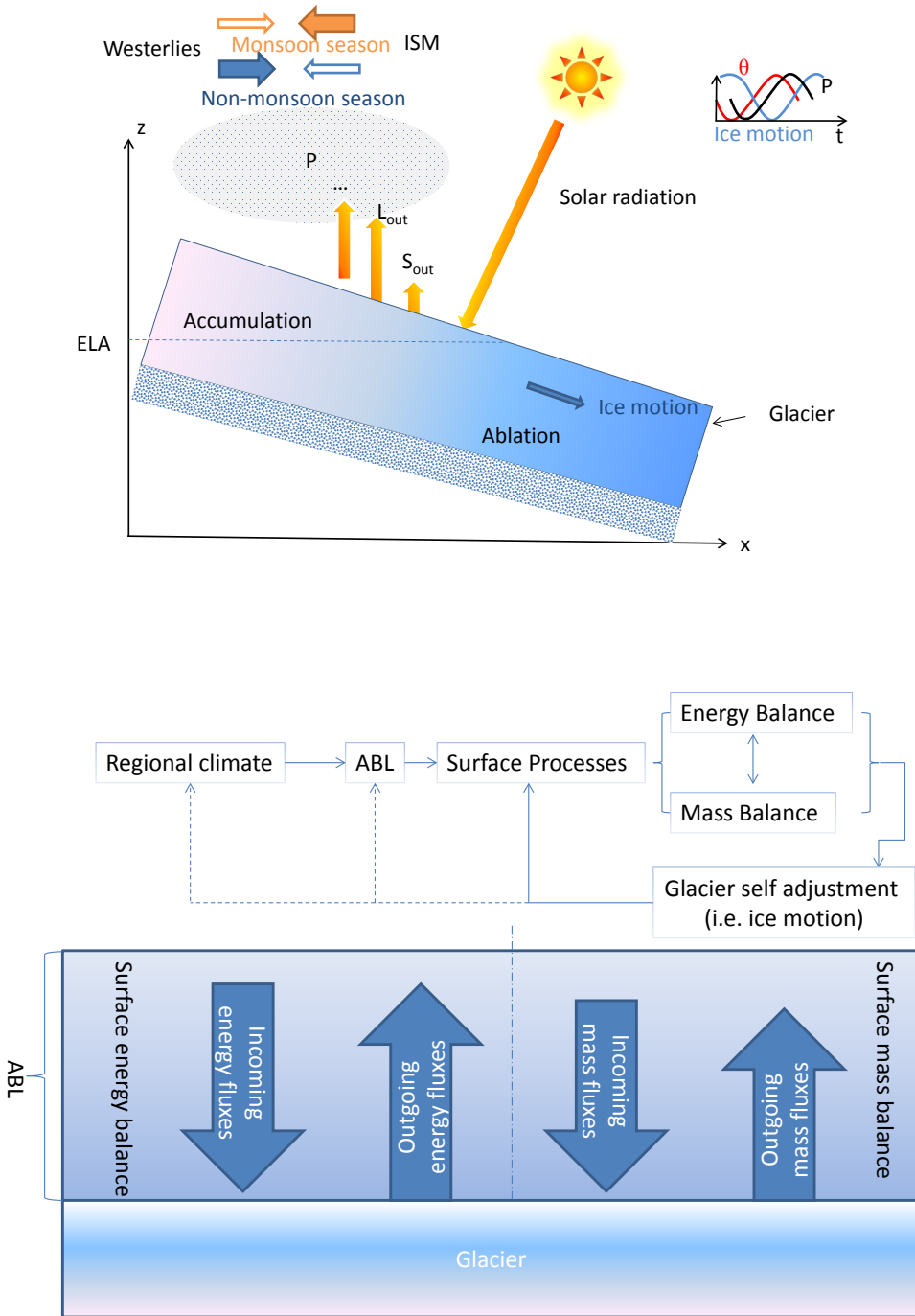


Figure 5.2: Schematic description of the glacier interacting with the regional climate. The dash line indicates the indirect relation and a solid line indicates a direct relation.

5.2. Data

5.2.1. Land surface temperature (MODIS day, night)

The monthly land surface temperature (LST) product (MOD11C3) with 0.05° resolution retrieved from Moderate Resolution Imaging Spectroradiometers (MODIS) is applied as a climatological indicator in the Nyainqêntanglha Range. The standard LST product of MODIS combines the valid data acquired by the Terra and Aqua satellites and is retrieved by the generalized split-window algorithm [114, 136]. Since Version 5 of LST MODIS, the highly increased spatial coverage of high elevation regions enables more consistent and continuous climatological studies in the region like the Tibetan Plateau. Current data products have been improved in several ways, such as the removal of temporal averaging in the 1 km daily Level-3 LST product, the reduction of cloud-contaminated LSTs in the Level-3 LST products and, the refinements in the day/night LST algorithm. The MODIS LST were evaluated against in-situ measurements at 47 validation sites including Nam Co lake (north of the Nyainqêntanglha Range) in the Tibetan Plateau. The accuracy of MODIS LST is shown to be better than 1 ± 0.5 K over 80% of cases [137].

5.2.2. Precipitation (TRMM)

In this study, the Tropical Rainfall Monitoring Mission (TRMM) 3B43 monthly post-real time product is used for precipitation analysis in the Nyainqêntanglha Range. The high-resolution precipitation data product covers the region for the period 1997-2015. from 50°N to 50°S i.e. more than one decade. The main products of the Tropical Rainfall Measuring Mission (TRMM) Multi-satellite Precipitation Analysis (TMPA) can be categorized into two parts: the near-real time products (RT) and post-real time products. Actually, the high quality passive microwave (HQ; 3B40RT), calibrated geostationary infrared (VAR; 3B41RT) and extra algorithms are applied in the TPMA/TRMM to derive better estimates of quasi-global precipitation since the production of TRMM 3B42RT, Version 6 [65]. In general, using the climatological calibration algorithm (CCA), microwave precipitation estimates from such as AMSR-E, AMSU-B and SSM/I are calibrated and integrated to increase the latitudinal coverage to $\sim 80\%$ as well as the accuracy of TRMM products. Compared with the near-real time products (RT), the major difference in the TRMM post-real time product is the calibration which is done by the TRMM Combined Instrument (TCI) merging rain gauges measurements. Since May of 2012, a significant upgrade, the novel Global Precipitation Climatology Center (GPCC) monthly dataset replacing old gauge analysis in CCA, has been implemented in the TRMM post-real time products. The resulting monthly product, which is a combination of satellite and gauge data, aggregated by three-hourly data, is the 3B43 product [64, 159].

5.2.3. Ancillary datasets

For high mountain area, the acquisition of long term and consistent meteorological observations suffers from poor accessibility and high maintenance cost of Automatic Weather Stations (AWS). For instance, there are only limited functioning on the north slope of Nyainqêntanglha Range. In this study, we have used available meteorological in-situ observations by AWS, even though the stations may not be fully representative of the entire area of interest. Satellite retrievals of precipitation and temperature provide better coverage of the Nyainqêntanglha Range for our large/regional scale study. These satellite data, specifically, the zonal averages of MODIS LST and TRMM precipitation were applied to construct the time series of surface temperature and precipitation and to analyze the response of glacier surface flow to climate forcing. This opens the possibility to extend data analysis beyond modeling glacier processes purely using in-situ measurements towards better understanding of processes at multiple temporal and spatial scales [64, 65, 106].

5.2.4. Preprocessing of MODIS and TRMM

1. The monthly MODIS and TRMM datasets were used to characterize the regional climate (i.e. annual cycle and season fluctuations). And the monthly TRMM datasets are fed to statistical analysis for monsoon temporal patterns by using non-parametric Man-Kendall (MK) approach. Climate in the area of interest during the monsoon and non-monsoon seasons was characterized based on this analysis (Section 5.5.1).

2. To estimate the differences of temperature and precipitation in the monsoon and non-monsoon seasons, the monthly MODIS and TRMM datasets are separated into 2 new datasets, i.e. monsoon and non-monsoon (Section 5.5.1); Similarly, to estimate the interaction between temperature and ice displacement, precipitation and ice displacement at the yearly time scale, the monthly MODIS and TRMM datasets are aggregated to yearly datasets on temperature and precipitation to match the timing of the ice surface displacement acquisitions (Section 5.5.2 and 5.5.3).

5.3. Analysis of monsoon temporal pattern

We have applied a statistical trend analysis, namely non-parametric Mann-Kendall (MK) [75, 91] test to the monthly TRMM 3B43 precipitation product. The MK method is based on the ranks of the measurement rather than their actual values, which is less perturbed by the distribution of the data time series or susceptible to the outliers. This method has been used to assess the significance of monotonic trends in a number of meteorological and climatological studies [76, 150].

The time series of precipitation is supposed to be $X = \{x_1, x_2, \dots, x_n\}$, in which

$n > 10$, the standardized Z is estimated as follows:

$$Z = \begin{cases} (s-1)/\sigma, & S > 0 \\ 0, & S = 0 \\ (s+1)/\sigma, & S < 0 \end{cases} \quad (5.1)$$

$$s = \sum_{k=1}^{n-1} \sum_{j=k+1}^n \text{sgn}(x_j - x_k) \quad (5.2)$$

$$\text{sgn}(x_j - x_k) = \begin{cases} 1, & x_j > x_k \\ 0, & x_j = x_k \\ -1, & x_j < x_k \end{cases} \quad (5.3)$$

If the time series of data are hypothesized as independent and identically distributed, The mean and variance of the statistic S can be given as below,

$$E(S) = 0 \quad (5.4)$$

$$V_0(S) = n(n-1)(2n+5)/18, \quad (5.5)$$

Then, the variance of S will be decreased due to the tied ranks in the dataset.

$$V_0^*(S) = \frac{1}{18} [n(n-1)(2n+5) - \sum_t t(t-1)(2t+5)] \quad (5.6)$$

Hence, the standard deviation σ is equalized to $\sqrt{V_0^*(S)}$,

$$\sigma = \sqrt{\frac{1}{18} [n(n-1)(2n+5) - \sum_t t(t-1)(2t+5)]} \quad (5.7)$$

where n is the number of observations, m is the number of group of tied ranks, each with t tied observations. The values of normally distributed statistic Z reveals that increasing ($Z > 0$) and decreasing ($Z < 0$) trend.

The Mann-Kendall-Sneyers (MKS) method has been applied to the sequentially forward u_k and backward u'_k series of the dataset as well. The inflections in the time series can be determined when the intersection between u_k and u'_k falls within the confidence interval. At the same time, an increasing trend ($u_k > 0$) or decreasing trend ($u_k < 0$) can be also determined when the points of u_k are outside the confidence interval. The temporal behavior of the series, as the stability, a significant trend and transition point, will be estimated by applying the Mann-Kendall-Sneyers (MKS) method [150]. The calculation of the statistic t_k , is calculated as follows:

$$t_k = \sum_{i=1}^k m_i (2 \leq k \leq n) \quad (5.8)$$

(m_i is the number of cases $x_i < x_j$, $j > i$) is normally distributed, with the mean and variance given by

$$\bar{t}_k = E(t_k) = \frac{k(k-1)}{4} \quad (5.9)$$

$$\overline{\sigma_{t_k}^2} = var(t_k) = \frac{k((k-1)(2k+5))}{72} \quad (5.10)$$

The normalized variable statistic u_k is the forward sequence.

$$u_k = \frac{(t_k - \bar{t}_k)}{\sqrt{var(t_k)}} \quad (5.11)$$

u'_k is calculated by applying the same method to the observations in a reversed sequence.

5.4. Response of glaciers with regional climate

5.4.1. Proposed mechanism of response

The incoming and outgoing heat fluxes determine the energy balance at the glacier surface. The energy balance drives melting, sublimation and determines the mass balance, taking into account the temporal variability of regional climate. The adjustment of the glacier in response to the surface energy balance and to the specific (at the surface) mass balance modifies glacier topography and surface flow [60, 102]. The turbulent heat fluxes at the interface of a glacier and the Atmospheric Boundary Layer (ABL) are modulated by the surface aerodynamic roughness (Chapter 3). When the temperature reaches the melting threshold, the melting rate increases with net radiation. A warming trend in regional climate tends to increase the melting rates of glacier. The hypothesis evaluated in this study is that observations of glacier surface flow can provide useful insights on glacier response to regional climate [4, 32].

The annual and multi-annual cycle of precipitation and temperature supplies mass to glaciers and removes it by e.g. melting and sublimation. We have analyzed glaciers in the Nyainqêntanglha Range interacting with regional climate characterized by using the zonal averages of precipitation (TRMM) and surface temperature (MODIS). Fig. 5.2 illustrates the schematic relation between glaciers and regional climate. It indicates that glacier dynamics respond to regional climate though the interplay of ABL and glacier surface process. This

leads to the variations of glacier energy balance and mass balance [100]. Specifically, mass changes at one location within a glacier induce mass redistribution, with the glacier becoming steeper and thicker by accumulation, while the surface field reflects the redistribution of mass towards lower elevation. Considering the possible warming or cooling by regional climate change i.e. Indian summer monsoon (ISM) and mid-latitude westerlies, the enhanced or weaker ice flow will transport ice mass to lower altitudes with changes in the velocity of surface ice flow. For instance, the precipitation is more dominant in the summer monsoon, because ISM's influence is stronger and more significant than the dry air flow by the mid-latitude westerlies. More precipitation combined with warming effect determines glacier dynamics by i.e. mass accumulation and melting during this season. In the contrast, the cooler and drier mid-latitudes westerlies become dominant in the non-monsoon season. The influence of precipitation and surface temperature on surface ice flow is reduced during this period. Therefore, measuring the glacier surface displacement is a proper proxy to assess the response of glacier to regional climate [81].

5.4.2. Estimating temporal response

Regional climate varies over multiple time scales, i.e. diurnal, seasonal, annual to even over decades scale. Glaciers respond to such time-dependent forcing through mechanism with inherent response to times which may lead to responses due to different time scales in the climate forcing signal. Here we propose to use observations of ice displacement $I(t)$ over a period of time as a measure of glacier response to regional climate forcing, as characterized by time series of precipitation $P(t)$ and surface temperature $\theta(t)$.

Estimate periodicity of observations

In this section, the study will be continued to analyze the temporal sequence of observations, precipitation (P), temperature (θ), and ice displacement (I). Regarding to temporal patterns of observations, the time series of P , θ and I can be described by the combination of a linear trend and a periodic signal. The time series of observations Y can be expressed as:

$$Y = \underbrace{G(t; c_l)}_{\text{Linear trend}} + \underbrace{F(t; A, \omega, \varphi, c_0)}_{\text{Periodic part}} \quad (5.12)$$

where Y is the sequence of observations, precipitation (P), temperature (θ), ice surface displacement (I). $G(t; c_l) = c_l t$, $F(t; A, \omega, \varphi, c_0) = \sum_{j=1}^m A_j \sin(\omega_j t + \varphi_j) + c_0$. c_l is unknown parameter of the linear trend, ω is the angular frequency of each periodic term and $T = 2\pi/\omega$ is the period, e.g., the annual ($T_1=1$ year, $\omega_1 = 2\pi/T_1$) and inter-annual ($T_2=5$ years, $\omega_2 = 2\pi/T_2$) periodic components are

presumed in the time series processing. The unknown parameters of periodic components are c_0 constant coefficient, A_j amplitude, and φ_j phase. The least squares approach is used to estimate the unknown parameters c_0 , c_I and A_j , and φ_j , the accuracy of estimated parameters is assessed as explained in Chapter 4.

Specifically, the time series of observations P, θ and I were modeled as a combination of a linear trend and periodic component.

$$P(t) = G_P(t; c_I) + F_P(t; A, \omega, \varphi, c_0) \quad (5.13)$$

$$\theta(t) = G_\theta(t; c_I) + F_\theta(t; A, \omega, \varphi, c_0) \quad (5.14)$$

$$I(t) = G_I(t; c_I) + F_I(t; A, \omega, \varphi, c_0) \quad (5.15)$$

where the periodic components are:

$$\begin{aligned} F_P &\Rightarrow A_P \sin(\omega_P t + \varphi_P) \\ F_\theta &\Rightarrow A_\theta \sin(\omega_\theta t + \varphi_\theta) \\ F_I &\Rightarrow A_I \sin(\omega_I t + \varphi_I) \end{aligned} \quad (5.16)$$

The use of a single periodic component is a constraint due to the rather long sampling interval feasible with observations of glacier surface displacement based on the analysis of Landsat images (Chapter 4). The challenge of acquiring cloud-free images combined with the long time required to capture slow surface displacements makes it very unlikely to measure displacements over a period shorter than a year, i.e. only multi-annual periodic components can be observed. The limited data record implies that the time series of observations on glacier surface flow includes less than 20 observations. Observations illustrated in Chapter 4, see e.g. Fig. 4.6, support the use of a single periodic component to describe the multi-annual variability in ice surface flow velocity. The observations P(t), $\theta(t)$ and I(t), however, show that the period of this component is not well defined and appears different in the three time series. Accordingly, we have applied a two – step approach:

- 1) Apply a Fast Fourier Transform analysis to all three time series to identify dominant periodic components;
- 2) Fit the de-trended time series with a single periodic component after estimating the period on the basis of the FFT results;

Each time series is then characterized as a combination of a linear trend, and a periodic component. The linear trend, amplitude of the periodic component have been estimated as described below.

Then three time series P , θ , and I have been represented as Eqs. 5.13, 5.14, 5.15 and 5.16. This procedure is rather approximate, since the three time series are modeled by applying a single periodic component, with some uncertainties in the estimated period of the dominant periodic component.

1. We applied the FFT analysis to different sets of MODIS, TRMM and in-situ measurements time series to detect the dominant periodic components of the time series [120, 133].

2. The possible periods were estimated by comparing the dominant periodic components of MODIS temperature, TRMM precipitation and in-situ measurements both monthly and yearly averages.

3. The FFT analysis was applied to the time series of glacier surface flow. The time series are calculated for each pixel from the total displacement in the time in-between two subsequent images.

4. The glacier surface displacement time series was fitted using different estimates of the period of the dominant component, as obtained by applying steps 1 through 3 to all three time series.

5. The linear trend and amplitude of the dominant periodic components of glacier surface displacement time series were finally obtained by using least squares fitting.

5.5. Results

5.5.1. Characterization of regional climate

In this section, the regional climate of the Nyainqêntanglha Range is characterized using satellite retrievals of precipitation and land surface temperature, i.e. time series of precipitation and land surface temperature the monthly TRMM 3B43 and the MODIS MOD11C3 data products. The high temporal variability of monsoonal precipitation was characterized by applying the Mann-Kendall-Sneyers (MKS) method the TRMM dataset.

Fig. 5.3 shows that the sequential values of the UF and UK statistics obtained with Mann-Kendall-Sneyers (MKS) method within the confidence interval of 95%. These statistics indicate that in the period 2000-2015 the monthly precipitation had a general decreasing trend between April and October. In particular, the decreasing trend is stronger in May, June, August and September. In contrast, the monthly precipitation between November to March is slightly increasing. The results in April, October, November, i.e. in the transition months between seasons show a larger variability in the inter-annual trend.

A typical Indian Summer Monsoon (ISM) sets in between late May and June (ISM onset period). The results of the MKS analysis (Fig. 5.3) imply a recent decadal pattern in the ISM influence in the Nyainqêntanglha Range. The inflec-

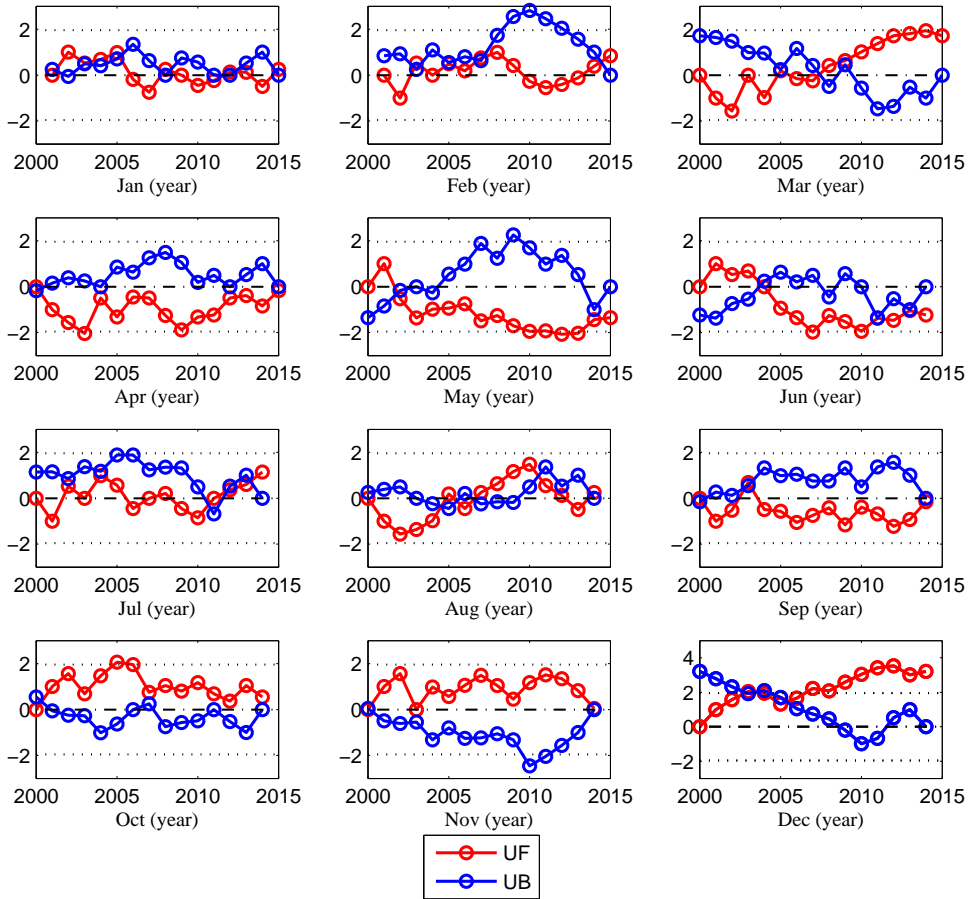


Figure 5.3: The forward (u_k , red) and backward (u'_k , blue) monthly Mann-Kendall statistics rank series of TRMM precipitation, from 2000 to 2015. The horizontal dotted lines represent the critical values corresponding to the 95% confidence interval.

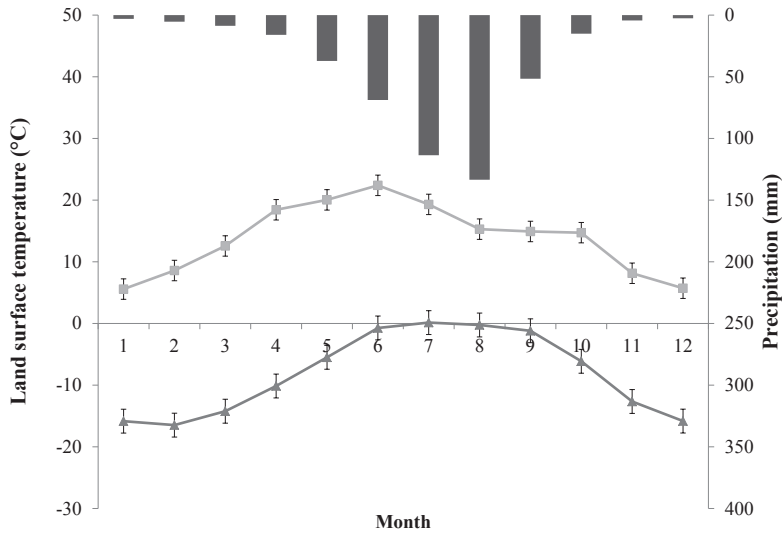


Figure 5.4: The zonally averaged TRMM precipitation (upper panel) and monthly MODIS land surface temperature (lower panel) (2000-2015) in the Nyainqêntanglha Range. The bar, the light gray curve and the dark gray curve both with error bar indicate the TRMM precipitation, MODIS land surface temperature (daytime), and MODIS land surface temperature (nighttime), respectively.

tions and trends in every month can be interpreted to reflect the strengthening or weakening of the ISM onset and multi-annual variability in the timing of ISM onset.

Combining with Figs. 5.3 and 5.4, the monthly-precipitation data indicate that the entire area of the Nyainqêntanglha Range becomes wetter starting from May, after experiencing the winter season (November – March).

The orientation of Nyainqêntanglha Range is generally from north-west to south-east, whose regional climate is found to be constrained by warm and moist air flow from ISM. However, atmospheric studies show that the ISM seems to be weaker at times within this region. Some evidence indicates that ISM is modulated by the colder and drier mid-latitude westerlies (MLW), leading to the different precipitation and temperature conditions [93, 95]. The seasonal mean of precipitation and temperature are calculated for the ground stations (Lhasa, Xainza and Baingoin) and compared with the zonal averages of TRMM precipitation and MODIS LST. The precipitation and LST of south and north side of Nyainqêntanglha Range are represented by observations the Lhasa and the average of Xainza

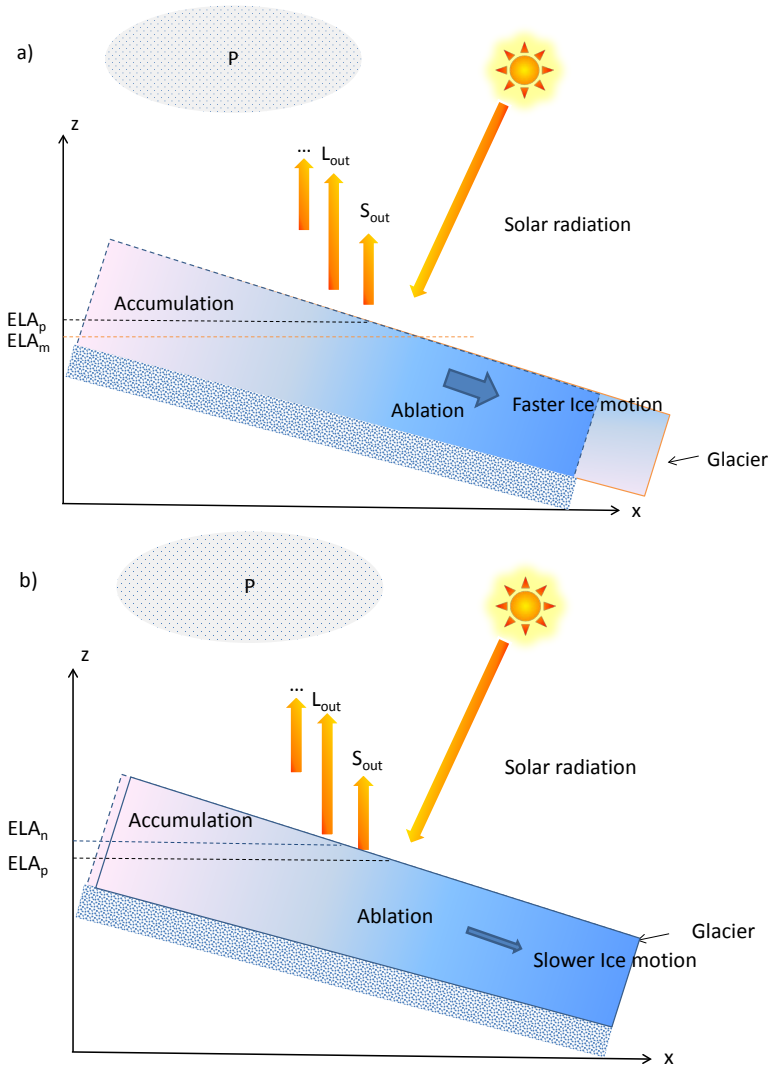


Figure 5.5: The schematic diagram shows the ice motion to the regional climate in the different seasons. (a) shows the ice motion is faster due to the simultaneous accumulation and ablation in the summer monsoon season. (b) shows the ice motion is slower due to the lower temperature and less precipitation, in turn, lower accumulation and ablation rates in the non-monsoon season. ELA_p , ELA_m , ELA_n denotes as the ELA of the previous year, the monsoon season and non-monsoon season of the current year.

Table 5.1: Mean seasonal of temperature and precipitation at the three meteorological stations for the pre-monsoon, monsoon, post-monsoon and winter seasons. Zonal averages of temperature and precipitation on the south and north sides of Nyainqêntanglha Range are represented by the records at Lhasa station and average of Xainza and Baingoin stations. Zonal averages of temperature and precipitation are derived from TRMM 3B43 monthly product and the MODIS MOD11C3 product. Note the zonal average is limited in the region, Latitude (29.47°, 31.44°), Longitude (89.41°, 91.70°).

| | | Pre-monsoon | Monsoon | Post-monsoon | Winter |
|---------------|------------------|-------------|---------|--------------|--------|
| θ (°C) | Zonal night-time | -10.20 | -1.15 | -9.00 | -16.46 |
| | Zonal day-time | 15.90 | 15.66 | 11.21 | 6.06 |
| | Zonal average | 5.70 | 14.51 | 2.21 | -10.40 |
| | Lhasa (S) | 10.16 | 16.87 | 8.07 | 2.17 |
| | Xainza (N) | 0.27 | 9.57 | -1.49 | -7.91 |
| | Baingoin (N) | -0.44 | 8.58 | -2.15 | -8.51 |
| | South side | 10.16 | 16.87 | 8.07 | 2.17 |
| North side | -0.36 | 8.59 | -2.17 | -8.43 | |
| P (mm) | Zonal average | 26.49 | 103.38 | 11.99 | 3.73 |
| | Lhasa (S) | 15.27 | 104.25 | 4.93 | 2.17 |
| | Xainza (N) | 14.53 | 78.33 | 6.88 | 1.58 |
| | Baingoin (N) | 14.29 | 73.70 | 6.35 | 2.54 |
| | South side | 15.27 | 104.25 | 4.93 | 2.17 |
| | North side | 14.41 | 76.02 | 6.62 | 2.06 |

and Baingoin stations, respectively. Higher precipitation and temperature were observed (Table 5.1) on the south side than the north side. These findings of spatial patterns of precipitation and temperature (see Table 5.1, Figs. 5.6 and 5.7) are supported by other studies [88, 160, Zhou et al.]. In other words, the latitudinal decreasing gradient of precipitation and temperature supports the weakening of the ISM within Nyainqêntanglha Range and surrounding region from south to north.

The main precipitation (the mean monthly value exceeds 50 mm) is concentrated in June, July, August, and September [160]. The monsoons dominate the distribution of the zonal moisture in this region during the summer (wet) season, while the westerlies are influential on the reduction of precipitation in the dry season. This climatological regime implies that accumulation and ablation of glaciers occur in the same summer months [95, Zhou et al.]. On the other hand, the evolution of monthly land surface temperature (both daytime and nighttime) during the year is similar with the precipitation, both higher in summer. The zonal average of mean monthly land surface temperature is higher

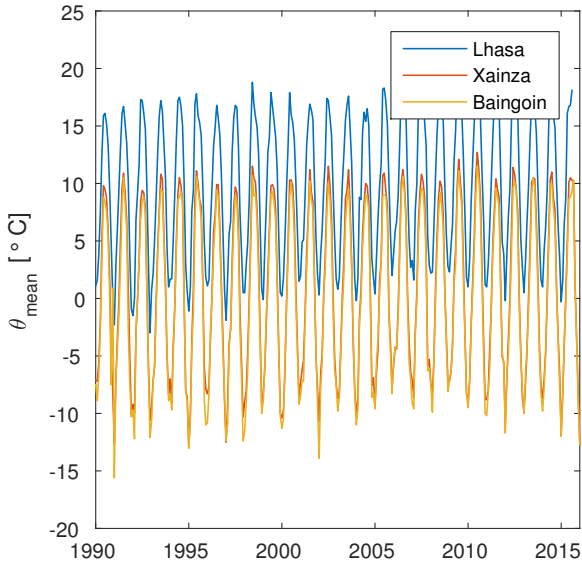


Figure 5.6: The recorded time series of air temperature at the weather stations Lhasa (blue), Xainza (red), and Baingoin (yellow) (1990-2015) neighboring the Nyainqêntanglha Range

than zero during daytime in the entire year, while the night-time land surface temperature is close to zero in June, July, August and September, i.e. the same months with high precipitation. There is about 10°C differences between daytime land surface temperatures and nighttime land surface temperatures. These results suggest that refreezing on the glacier surface and mass accumulation may occur during the night even in the summer season. This summer accumulation regime is contrary to other winter accumulation glaciers [155]. The statistics in Table 5.1 mean there is a clear separation of the summer monsoon season from non-monsoon season. Second, the yearly evolution of temperature can further give specific seasonal patterns related to the ISM influence combined with precipitation in the Nyainqêntanglha Range.

Recent in-situ measurements at sites surrounding the Nyainqêntanglha Range [74] gave similar indications to our findings on satellite-based observations. There is only a small proportion of mean annual precipitation measured in the winter season (November - March) compared to that in the summer season (around 90%), according to the records in the meteorological stations Shengzha, Bange, Dangxiong, Lhasa (Table. 5.1). Regional climate features remain dominant, even though the observations are slightly different on the two sides of the Nyainqêntanglha Range. The average of the annual precipitation was about 50.6 mm in the last decades. Due to the weakening of the monsoons and strengthening of

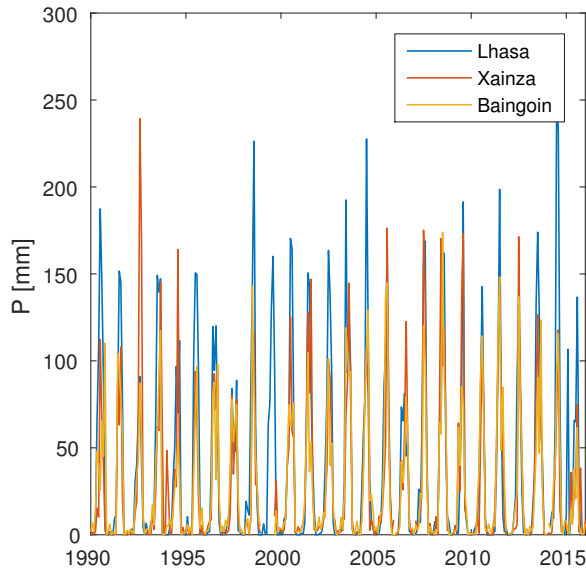


Figure 5.7: The recorded time series of precipitation at the weather stations Lhasa (blue), Xainza (red), and Baingoin (yellow) (1990-2015) neighboring the Nyainqêntanglha Range

the westerlies, the increment of temperature in the north side of the Nyainqêntanglha Range was higher than in the south side (see Fig. 5.6 and Fig. 5.7), while the general trend of precipitation is gradually decreasing according to observations [74]. Changes of glaciers have also been measured in terms of the changes in glacier area, length, mass balance [155]. Most of the measured glaciers revealed a retreat tendency during the last decades. The temporal variation of the precipitation are supposed to interact with the observed changes in the glaciers of this area. Therefore, the spatial and temporal patterns related to the ISM influence need be characterized better [160]. Hereafter, the pre-monsoon season is considered from March to May, the summer from June to September, then post-monsoon season from October to November, and the winter season is a relatively drier and cold period from December to February.

5.5.2. Temporal patterns in precipitation and temperature

In situ, long term meteorological data is limited in this region, even though some of the latest automatic weather stations have been installed since 2005 to provide the data required to monitor cryospheric and hydrological processes. The temporal variability of precipitation and temperature has been characterized first by analyzing the time series of air temperature and precipitation observed at the stations: Lhasa (south side of Nyainqêntanglha Range), Xainza and Baingoin

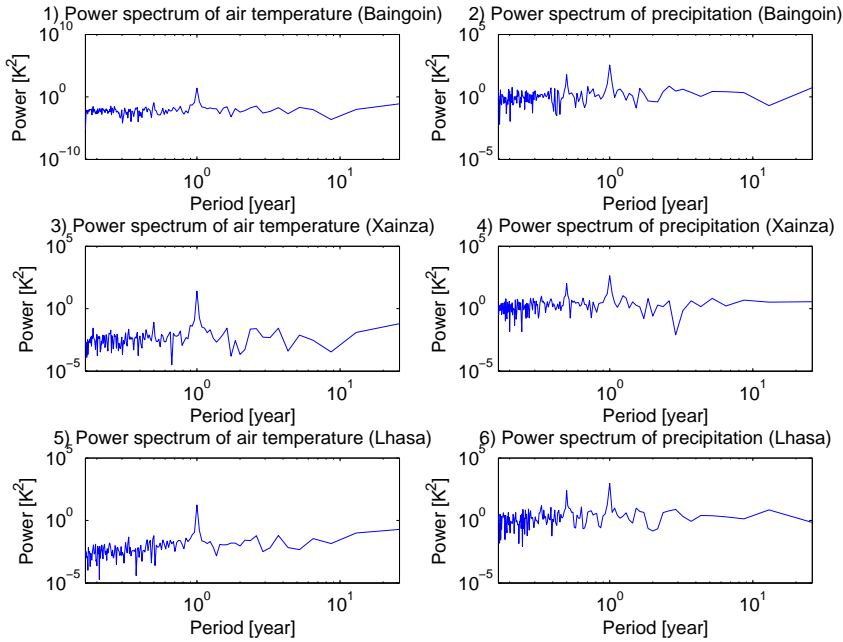


Figure 5.8: Power spectrum of air temperature and precipitations time series at the weather station Baingoin Xainza and Lhasa neighboring the Nyainqêntanglha Range. 1), 3) and 5) are the power spectra of air temperature of Baingoin Xainza and Lhasa; 2), 4) and 6) are the power spectra of precipitation of Baingoin Xainza and Lhasa.

(north side of Nyainqêntanglha Range). The detailed information from these stations is summarized in Table. 5.1 and compared with the zonal averages of surface temperature and precipitation. Time series analysis has been applied to these observations to capture differences and similarities in the temporal signals.

The method has been described in Section 5.4.2. First, the power spectrum of monthly TRMM and MODIS LST and in-situ measurements at three AWS stations Baingoin, Xainza, Lhasa neighboring the Nyainqêntanglha Range has been estimated by applying a Fast Fourier Transform analysis. The ground-based signals (see Fig.5.8) are dominated, as expected, by the annual component, but multiple multi-annual components (from 3 years up to 7 or 8 years) are present as well. The monthly MODIS and TRMM signals are dominated by the annual component as well (see Fig. 5.9), and similar multi-annual components are present i.e. with periods between 2 and 4 years. Monthly TRMM and MODIS LST time series were fitted using the annual component only (see Fig. 5.10): the residuals show a large inter-annual variability, thus confirming the results of the FFT analysis. The processes determining the response of glaciers to temporal variability lead

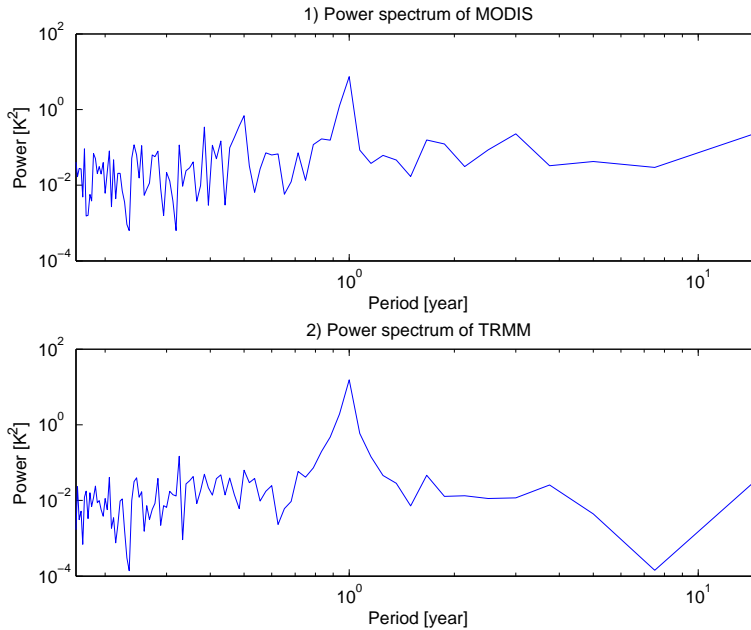


Figure 5.9: Power spectrum of zonal averaged monthly temperature and precipitation time series. Zonal averages of temperature and precipitation are derived from TRMM 3B43 monthly product and the MODIS MOD11C3 product. Note the zonal average is limited in the region, Latitude (29.47°, 31.44°), Longitude (89.41 °, 91.70°).

to rather long response times, so the multi – annual components are more likely to appear in response signals such as the glacier surface flow velocity.

5.5.3. The interaction of ice flow with regional climate

As regards the temporal scale, the response of glacier with regional climate is expected to appear as multi-annual variability of accumulation and ablation. For shorter time scales (i.e. the annual cycle), accumulation and ablation occur simultaneously in the summer monsoon season. The interaction of glaciers with multi-annual climate variability can be captured by observing variables such as surface ice displacement in wintertime (see Chapter 4). In general, ice flow temporal patterns are coupled with diverse factors such as mass input (i.e. precipitation), temperature-induced melting, ice geometry, ice creep features. For instance, ice mass is ablated by melting and sublimation at the glacier surface [60]. The radiation and turbulent heat fluxes at the interface between ABL and glacier surface govern the process of melting and sublimation. The melting rate of glaciers can be accelerated under a regional warming trend [4, 32].

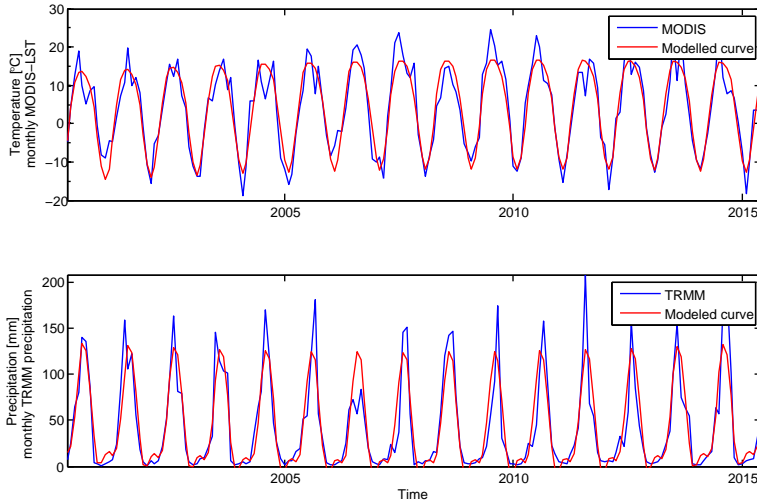


Figure 5.10: Modeled time series of zonal averages (Nyainqêntanglha Range) of monthly MODIS LST and TRMM precipitation (2000-2015) by using the annual component only.

Our assumption is that the combined influence of ISM and MLW determines seasonal, annual and multi-annual components of in-situ and satellite based observations of precipitation and temperature. The monthly in-situ observations P and θ (Figs. 5.6, 5.7 and 5.8) are clearly dominated by the yearly cycle, but multi-annual variability is also clearly observable. The amplitude of multi-annual component of aggregated yearly TRMM and MODIS in the monsoon season estimated by using FFT analysis are shown in Fig. 5.15. There are several multi-annual components, and the dominant component has a period of about 4 years.

As explained in Chapter 4, we used retrieval of ice surface displacement over subsequent sampling intervals of approximately 1 year from 2000 to 2015. Before analyzing the time series of glacier surface displacements, we applied multi-linear regression analysis and used seasonal P (TRMM) and θ (MODIS LST) in each year to characterize regional climate. The TRMM and MODIS satellite data products were used because of their spatial coverage, since the three stations mentioned above were considered insufficient to capture spatial variability across the Nyainqêntanglha Range. The spatial and temporal coverage of the retrievals on ice surface displacements have been detailed in Chapter 4. Preliminarily we evaluated the correlation of annual ice displacement with the seasonal P and θ . Firstly, separately with each variable, then together by multi-linear regression analysis.

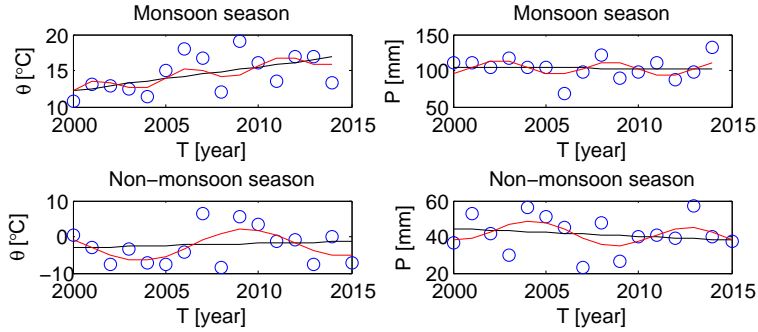


Figure 5.11: Modeled time series of zonal averages of aggregated yearly MODIS LST and TRMM precipitation (2000-2015) both for monsoon and non-monsoon season neighboring the Nyain-qêntanglha Range. The multi-annual patterns are identified by using least squares fitting procedures.

Glacier surface displacement is clearly more correlated with P and LST in the monsoon season (see Fig. 5.12 and 5.13). Correlation (R^2) between ice flow and P , θ was in the range between 0 and 0.8 with many occurrences in the range between 0.1 and 0.3. To assess spatial patterns of these correlations and possible dependency on elevation (H), the ice surface displacements are divided into ten classes ($-\infty$, 5500 m], (5500 m, 5600 m], (5600 m, 5700 m], (5700 m, 5800 m], (5800 m, 5900 m], (5900 m, 6000 m], (6000 m, 6100 m], (6100 m, 6200 m], (6200 m, 6300 m], (6300 m, $+\infty$). A threshold ($R^2 > 0.5$) is set to derive the partition of significant influence of P or θ . The sites with $R^2 > 0.5$ occupied a small fraction of the study area. There are slightly higher R^2 concentrated in the monsoon season than non-monsoon season (see Fig. 5.12 and 5.13).

5.5.4. Estimating the trend and amplitude of ice surface flow

Taking into account the complexity of processes determining the interaction of ice surface flow to regional climate, including the coupling between surface flow and deeper ice deformation / basal sliding, we evaluated the linear trend and amplitude of surface flow in the response of climate forcing. The linear trend and amplitude can be regarded as approximate indicators of glacier response to regional climate.

As mentioned in the sections above, the precipitation coupled with temperature in principle may lead to observable responses during readjustment of a glacier to variations in the temporal distribution of accumulation and ablation over temporal scales of one year or longer. In this section, the linear trend and amplitude of periodic components of ice surface displacement time series in

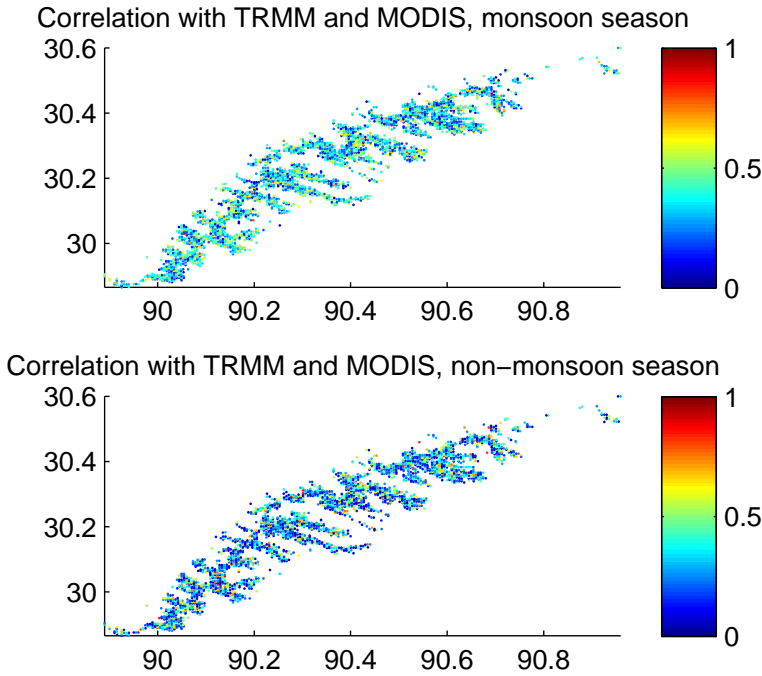


Figure 5.12: The correlation of ice flow with TRMM precipitation and MODIS LST (2000-2015) both for monsoon and non-monsoon seasons, Nyainqêntanglha Range.

response of precipitation and surface temperature are estimated by using the methodology in Section 5.4.2.

First, we evaluate the signals in the glacier surface displacement time series by applying FFT analysis to a few samples (see Fig. 5.16). Then, the FFT analysis was applied to all the glacier surface displacement pixel-wise time series. The results show that surface glacier flow signal is dominated by a multi-annual component with a period = 7.5 years. Combined with the results of previous analysis of temporal patterns in the regional precipitation and temperature, this indicates that ice flow responds to the regional climate in an indirect way by responding to faster components, i.e. with shorter periods, in the climate forcing. The FFT analysis of P and θ in the monsoon season (Fig. 5.15) clearly shows that the component with period = 7.5 years is smaller than the components with shorter periods. A single periodic component with period = 7.5 years captures well the interannual variability in glacier surface flow (Fig. 5.16). The period = 7.5 years was

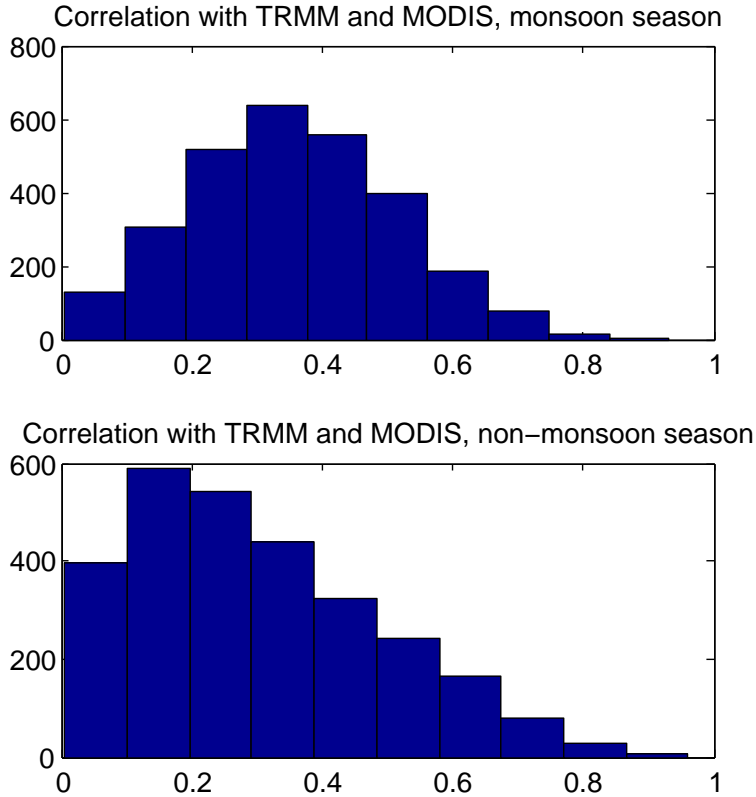


Figure 5.13: The histogram of correlation of ice flow to TRMM precipitation and MODIS LST (2000-2015) both for monsoon and non-monsoon seasons neighboring the Nyainqêntanglha Range, respectively.

chosen to fit the glacier surface displacement time series and assess the linear trend and amplitude of the multi-annual component (see Fig. 5.17).

The elevation of the study area ranges from lower than 5500 m to higher than 6300 m. The results indicate that both the linear trend and amplitude of periodic component distribute heterogeneously and do not have a clear relationship with either elevation, although larger values of trend and amplitude seem more frequent at lower elevation (Fig. 5.17).

Compared with the monsoon season, lower land surface temperature and less precipitation are observed in non-monsoon seasons (see Fig. 5.3). Any variations of precipitation and temperature, such as temporal variability, will result in the response of glaciers at different locations diversely (i.e. altitudinal pattern). All these impacts can be accumulated from monsoon season to non-monsoon

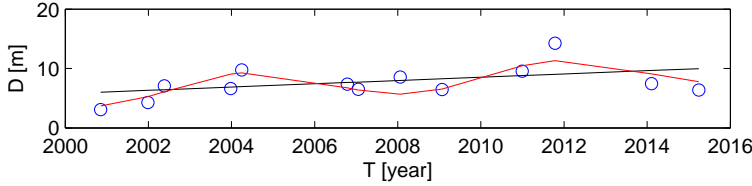


Figure 5.14: An example of the fitted time series of ice flow (2000-2015) within the Nyainqêntanglha Range.

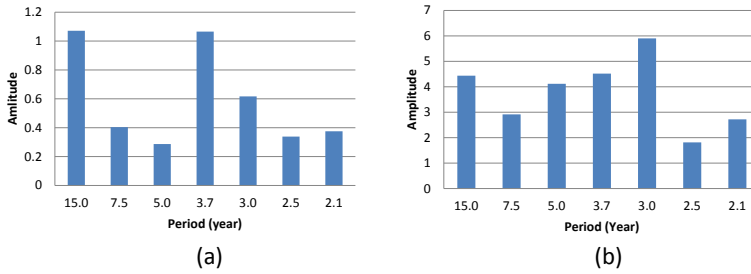


Figure 5.15: Amplitude of MODIS LST and TRMM precipitation time series in the monsoon season. a) MODIS LST in the monsoon season; b) TRMM in the monsoon season.

season. It leads to the different temporal patterns (period) and linear trend and amplitude of periodic component of glacier surface displacement times series. According to Cuffey and Paterson [32], the response time of glaciers to precipitation and temperature should be in the range from 3 up to tens of years scale.

5.6. Conclusions

In this research, time series analysis is used to estimate the response of glacier ice flow to regional climate in terms of precipitation and temperature within the Nyainqêntanglha Range. First, the temporal pattern of regional climate is assessed in terms of precipitation and temperature by MKS analysis. The prevailing climate is evaluated in terms of precipitations and land surface temperatures, given the scarcity of meteorological stations. Most of the precipitation and higher land surface temperature (both daytime and nighttime) are measured in the summer season while it is cooler and drier in the non-monsoon season. This implies that both accumulation and ablation occur in summer [160, 163]. Second, the statistical dependence of ice flow on precipitation and temperature was estimated by multi-regression analysis. The linear trend and amplitude of multi-annual component of glacier surface displacement times series was evaluated by

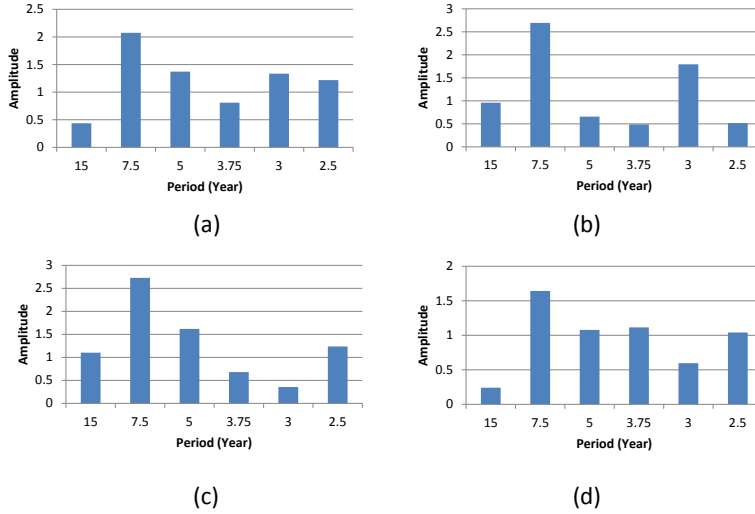


Figure 5.16: Examples of the amplitude of periodic component of glacier surface displacement time series (2000-2015) by FFT analysis in the Nyainqêntanglha Range.

using FFT analysis combined with least squares approach. Applying FFT analysis and least squares approach to precipitation, temperature and glacier surface displacement times series, the temporal patterns in each signal were captured and interpreted. These findings imply that satellite based feature tracking method can be applied to construct long term time series of ice flows and capture interactions with regional climate variables in this region. Further application of this approach will help to understand the glacier dynamics in response to the regional climate.

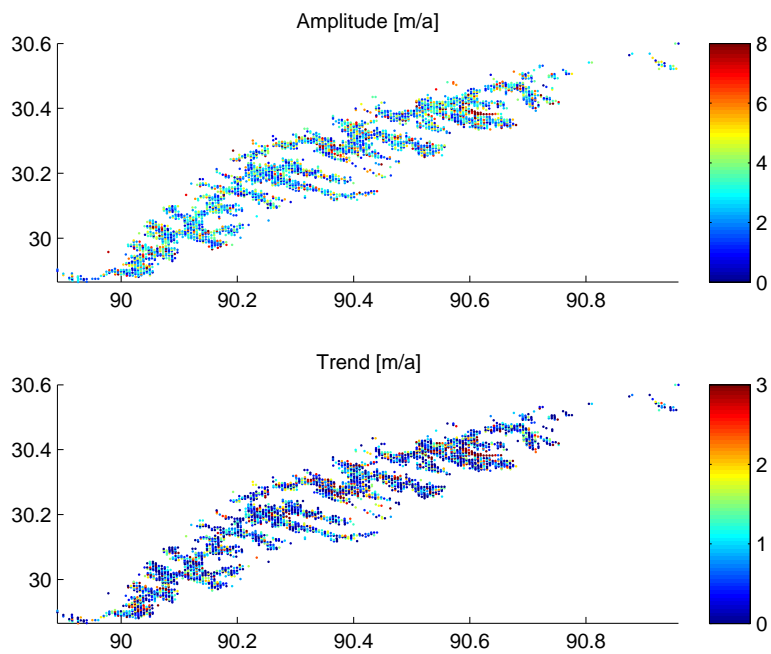


Figure 5.17: The trend and amplitude of multi-annual component of ice flow derived by using the optimized period=7.5 years though combined FFT analysis and non-linear least squares approach.



6

Conclusions and future work

This dissertation describes remote sensing observations of two glacier properties:

- a) The surface roughness;
- b) The ice velocity of glacier surface flow;

This study focused on the Nyainqêntanglha Range on the Tibetan Plateau.

Section 6.1 explains how and what extent the research questions detailed in Chapter 1 were addressed.

Section 6.2 outlines recommendations for further research.

6.1. Conclusions

Glaciers on the Tibetan Plateau are large water reservoirs, and good indicator of climate variability. The glacier is driven by the surface energy balance, which determines sublimation, and melting, and evaporation and is modulated by the glacier surface properties, i.e. surface roughness, glacier displacements, and absorbed energy for melting process. Across the plateau glaciers respond to different atmospheric forcing due to the relative weight of the mid-latitude westerlies and the summer monsoon. Mass input in a glacier accumulation zone and mass removal in the ablation zone drive the glacier surface flow. The heat and mass exchange between glacier and atmosphere are modulated by the surface roughness.

This reasoning led to this study, all the datasets were used here:

- 1) satellite altimetry was applied to estimate glacier surface roughness;
- 2) appropriate spatial resolution spaceborne optical images were applied to estimate and map the ice velocity of glacier surface flow;

3) satellite data products on precipitation and land surface temperature were applied to characterize climate forcing.

The study focused on the Nyainqêntanglha Range, which is located on the Tibetan Plateau in the transition area between mid-latitude westerlies and monsoon climate.

In Chapter 1 the following research questions were started:

1. Is it feasible to retrieve surface properties from satellite laser altimetry data over the Tibetan Plateau?

2. How should glacier surface displacement and mean velocity of Tibetan glaciers be estimated?

3. Does glacier surface displacement of Tibetan glaciers respond to climate variability?

Ad. 1 Glaciers in the Tibetan mountains are expected to be sensitive to turbulent sensible and latent heat fluxes. One of the most significant factors of the energy exchange between the atmospheric boundary layer and glacier is the roughness of the glacier surface. The aerodynamic roughness of a complex surface like a glacier is related to its geometric characteristics at multiple spatial scales. Methods to parameterize this roughness for glaciers surface were applied in the remote regions of TP. In this study a two-stage approach was applied. First, the capability of return waveforms to characterize TP landscapes was evaluated. Extraction of parameters of waveforms measured by the ICESat/GLAS laser system from February, 2003 to November, 2004 was evaluated by analyzing data along several tracks across glaciers in the Nyainqêntanglha range. Surface features, namely roughness, slope and elevation were retrieved independently from ASTER GDEM. The response of GLAS waveforms to these glacier surface features has been documented by statistics on full waveform parameters, namely number of modes, width of the full waveform and elevation. These statistics show that the GLAS waveforms are related to the surface geometric features and useful to parameterize the surface aerodynamic roughness. Consequently, the retrieved waveform can be explained by the terrain characteristics. In our study area, roughness and slope of the surface can contribute several meters to even several tens of meters to the pulse shape. Next, the relationship between surface slope and roughness was derived first theoretically, then using the ASTER GDEM surface features and the observed GLAS waveform parameters. The later delivered the relationship between terrain characteristics and waveform parameters required to parameterize the surface aerodynamic roughness.

Ad. 2 The glacier surface flow responds to changes in accumulation and ablation and through that, to regional climate, but must be mapped and monitored over long periods of time. We monitored the ice surface displacement of the glaciers in the entire Nyainqêntanglha Range over nearly two decades from 1993

to 2015 by applying a feature-tracking method to multi-temporal Landsat image data. Suitable images could only be retrieved in the non-monsoon season and were spaced by about one year, so that our estimates were approximately yearly values. Post-processing was applied to detect outliers, taking into account estimated spatial variability, towards higher quality of retrieved surface displacements. It reduces the bias existing in the final displacement measurements on the mountainous glaciers. The precision of ice displacement was evaluated by using measurements on the relative stable ground outside glaciers. Through the time series analysis of ice surface displacements, we found that the observations could be represented by a combination of a linear component and multi-annual component. This applied especially to the ablation zone of observed glaciers. The multi-annual component could be represented by a single periodic component with a period of multiple years. In practice, we estimated and mapped the linear trend ν and the amplitude of multi-annual component a . By capturing their spatial distributions we could evaluate their dependence on both elevation and slope. The observed glaciers are active, as documented by the linear trend and amplitude of multi-annual component across the entire range of elevation and slope. The analysis indicates that the spatial variability of glacier multi-annual amplitude seems to be more dependent on elevations and slope than the linear trend in the Nyainqêntanglha Range. The study demonstrated that observations of ice surface displacement retrieved by optical image data provide useful insight on the glacier dynamics in the Nyainqêntanglha Range.

Ad.3 In this study, the regional climate has been characterized using TRMM precipitation and the MODIS land surface temperature data products, while the local glacier response to regional climate has been characterized using the period, linear trend and amplitude of the periodic component of glacier surface flow. The analysis of monthly precipitation and land surface temperature led to define seasons as they occur on the Tibetan Plateau. Most important for glaciers mass balance is the summer monsoon season when both high precipitation and high surface temperature occur. The statistical dependency of ice flow on precipitation and temperature was estimated by multi-regression analysis. According to the interaction between regional climate (precipitation and temperature) and glaciers, the linear trend and amplitude of periodic component of glacier surface displacement times series was evaluated by using FFT analysis combined with the least squares approach. Applying FFT analysis and least squares approach to regional climate forcing (precipitation and temperature) and ice flow in terms of surface displacement times series, the temporal patterns of ice flow are estimated. It indicates that the behavior of ice flow relates the patterns of glacier self-adjustment induced by regional climate forcing (temperature and precipitation). These findings imply that satellite based feature tracking method is capa-

ble to establish long term time series of ice flows and estimate interactions with regional climate variables in this region.

6.2. Future work

The understanding of the physical relationship between glaciers and regional climate is essential to project the response of Tibetan glaciers to global climate. The surface processes, i.e. melting, sublimation and evaporation of these glaciers link the glacier mass balance with atmospheric boundary layer. Normally, the accumulation and ablation processes occur in different seasons on the continental and temperate glaciers. On the Tibetan Plateau both precipitation and temperature vary with different timing and are determined by moisture and heat transfer at continental scale. That will affect the regime of glacier mass balance, i.e. accumulation and ablation of glacier occur at the same time in summer. These processes need to be understood better across spatial and temporal scales. Recent modelling and monitoring research has been initiated and should be pursued further. This study demonstrates the interest of integrating remote sensing observations on roughness, glacier surface displacement, glacier elevation changes, surface temperature, and precipitation to understand glacier surface processes and glacier response to climate. Such studies could be extended to other areas on the Tibetan Plateau using new data, e.g. satellite altimetry by ICESat-2 and CryoSat, Sentinel-2 multi-spectral images and Sentinel-3 land surface temperature. Such data would allow to extend the temporal coverage of observations and improve current understanding of spatial patterns, trends and inter-annual variability. Approach in data analysis should also be improved, taking into account the challenges related to the complex terrain in some areas on the Tibetan Plateau. Better and extended data analysis will improve the accuracy of current retrievals. Overall, better accuracy will deliver new insights on the changes in Tibetan glaciers and their role in regional water security.

Curriculum Vitæ

Junchao Shi

Junchao Shi was born in Henan Province in China on June 28th, 1984. He focused on Hydrology and Water Resources for the master study at Hohai University in Nanjing. In 2009, he was accepted as a PhD student at Delft University of Technology, supervised by Prof. dr. Massimo Menenti, and financially supported by a scholarship from Chinese Scholarship Council (CSC). During his PhD, he focused on observing the glacier surface properties by using laser and optical remote sensing techniques. In this study, he chose one of the most significant glaciated areas, Nyainqêntanglha Range, as the study area. It was transition zone of continental and maritime climate in the Southern of Tibetan Plateau. He derived these glacial observations based on full waveform analysis of ICESat/GLAS products, features tracking method for optical images and time series analysis. In particular, the surface characteristics of glaciers were estimated by full waveform information of laser altimetry. The main ice flow properties are explored by surface features tracking method and time series analysis. From 2014, he worked as researcher at TU Delft on TIGER initiative and TEP- hydrology projects funded by ESA. They aimed to promote the use of Earth Observation (EO) data on water resource related issues. The responsibility of TU Delft within TIGER initiative was mainly about supplying the necessary cooperation and supervision on water resources related issues as well as remote sensing techniques for African scientists or collaborators. TEP-hydrology was more dedicated to develop information platform integrating both ESA remote sensing products and optimized hydrology modeling approach for the end users.



List of Publications

7. Shi, J. C., et al. (2013). Parameterization of Surface Roughness Based on ICESat/GLAS Full Waveforms: A Case Study on the Tibetan Plateau. *Journal of Hydrometeorology* 14(4): 1278- 1292.
6. J. Shi, M. Menenti, Monitoring recent variations of the surface displacements of eight Nyainqêntanglha glaciers. *Hydrol. Earth Syst. Sci. Discuss.* 11(2): 1555-1581.
5. Junchao Shi, Massimo Menenti, Roderik Lindenbergh. Morphological characteristics detection on the Tibetan glaciers using ICESat data. In CAHMDA IV- The Fourth International Workshop on Catchment-scale Hydrological Modeling and Data Assimilation, 2010, Lhasa, China.
4. Junchao Shi, Ling Chang. Surface deformation of alpine terrain derived by PS-InSAR technique on the Siachen Glacier. In Fringe workshop ESA, 2011, Frascati, Italy.
3. Junchao Shi, Massimo Menenti, Roderik Lindenbergh. Surface deformation of alpine terrain derived by PS-InSAR technique on the Siachen Glacier. In European Geosciences Union General Assembly 2012, Vienna, Austria.
2. Junchao Shi, Massimo Menenti, Roderik Lindenbergh. Evaluating ICESat full waveforms over the part of Nyainqêntanglha Mountain Range, The Tibetan Plateau. IEEE International Geoscience and Remote Sensing Symposium (IGARSS), 22-27 July, 2012, Munich, Germany.
1. Junchao Shi, Massimo Menenti. Monitoring recent acceleration of the shrinkage on the polythermal glaciers – a case study in the Nyainqêntanglha Mountains. IEEE International Geoscience and Remote Sensing Symposium (IGARSS), 21-26 July, 2013, Melbourne, Australia.



References

- [1] Abshire, J., Ketchum, E., Afzal, R., Millar, P., and Sun, X. (2000). The geoscience laser altimeter system (GLAS) for the ICESat mission. pages 602–603. IEEE.
- [2] Abshire, J., Sun, X., Riris, H., Sirota, J., McGarry, J., Palm, S., Yi, D., and Liiva, P. (2005). Geoscience Laser Altimeter System (GLAS) on the ICESat mission: On-orbit measurement performance. *Geophysical Research Letters*, 32(21).
- [3] Abshire, J., Sun, X., Riris, H., Sirota, M., McGarry, J., Palm, S., Ketchum, E., and Follas, R. (2003). Geoscience laser altimeter system (GLAS) on the ICESat mission: pre-launch and on-orbit measurement performance. In *Geoscience and Remote Sensing Symposium, 2003. IGARSS'03. Proceedings. 2003 IEEE International*, volume 3, pages 1534–1536. IEEE.
- [4] Ageta, Y. and Fujita, K. (1996). Characteristics of mass balance of summer-accumulation type glaciers in the Himalayas and Tibetan Plateau. *Zeitschrift für Gletscherkunde und Glazialgeologie*, 32(PART 2):61–65.
- [5] Aizen, V. B., Aizen, E. M., and Nikitin, S. A. (2002). Glacier regime on the northern slope of the Himalaya (Xixibangma glaciers). *Quaternary International*, 97–98:27–39.
- [6] Andreas, E. L. (1987). A theory for the scalar roughness and the scalar transfer coefficients over snow and sea ice. *Boundary-Layer Meteorology*, 38(1-2):159–184.
- [7] Andreas, E. L. (2002). Parameterizing Scalar Transfer over Snow and Ice: A Review. *Journal of Hydrometeorology*, 3(4):417–432.
- [8] Arya, S. P. S. (1973). Contribution of form drag on pressure ridges to the air stress on Arctic ice. *Journal of Geophysical Research*, 78(30):7092–7099.
- [9] Arya, S. P. S. (1975). A drag partition theory for determining the large-scale roughness parameter and wind stress on the Arctic pack ice. *Journal of Geophysical Research*, 80(24):3447–3454.

- [10] Arya, S. P. S. (1977). Suggested Revisions to Certain Boundary Layer Parameterization Schemes Used in Atmospheric Circulation Models. *Monthly Weather Review*, 105:215.
- [11] Baarda, W. (1968). *A testing procedure for use in geodetic networks*, volume 5 of *Publications on Geodesy*. Netherlands Geodetic Commission, Delft, second edition.
- [12] Baarda, W. (1976). Reliability and precision of networks. In *VIIIth International Course for Engineering Surveys of high precision*, pages 1–11, Darmstadt, Germany.
- [13] Baarda, W. (1977). Measures for the accuracy of geodetic networks. In *International symposium in Optimization of Design and Computation of Control Networks*, pages 1–26, Sopron, Hungary. IAG.
- [14] Baarda, W. (1979). Mathematical models. *European Organization for Experimental Photogrammetric Research*, 11:73–101.
- [15] Bao, Q., Yang, J., Liu, Y., Wu, G., and Wang, B. (2010). Roles of Anomalous Tibetan Plateau Warming on the Severe 2008 Winter Storm in Central-Southern China. *Monthly Weather Review*, 138(6):2375–2384.
- [16] Berthier, E. (2007). Remote sensing estimates of glacier mass balances in the Himachal Pradesh (Western Himalaya, India). *Remote Sens. Environ.*, 108:327–338.
- [17] Bindschadler, R. A. and Scambos, T. A. (1991). Satellite-Image-Derived Velocity Field of an Antarctic Ice Stream. *Science*, 252(5003):242–246.
- [18] Bolch, T., Pieczonka, T., and Benn, D. I. (2011). Multi-decadal mass loss of glaciers in the Everest area (Nepal Himalaya) derived from stereo imagery. *The Cryosphere*, 5(2):349–358.
- [19] Bolch, T., Yao, T., Kang, S., Buchroithner, M. F., Scherer, D., Maussion, F., Huintjes, E., and Schneider, C. (2010). A glacier inventory for the western Nyainqentanglha Range and Nam Co Basin, Tibet, and glacier changes 1976–2009. *The Cryosphere*, 4:429–467.
- [20] Bolin, B. (1950). On the Influence of the Earth's Orography on the General Character of the Westerlies. *Tellus*, 2(3):184–195.
- [21] Bothe, O., Fraedrich, K., and Zhu, X. (2011). Large-scale circulations and Tibetan Plateau summer drought and wetness in a high-resolution climate model. *International Journal of Climatology*, 31(6):832–846.

- [22] Broccoli, A. J. and Manabe, S. (1992). The Effects of Orography on Midlatitude Northern Hemisphere Dry Climates. *Journal of Climate*, 5(11):1181–1201.
- [23] Brock, B. W., Willis, I. C., Sharp, M. J., and Arnold, N. S. (2000). Modelling seasonal and spatial variations in the surface energy balance of Haut Glacier d’Arolla, Switzerland. *Annals of Glaciology*, 31(1):53–62.
- [24] Brock, B. W., Willis, I. C., and Shaw, M. J. (2006). Measurement and parameterization of aerodynamic roughness length variations at Haut Glacier d’Arolla, Switzerland. *Journal of Glaciology*, 52(177):281–297.
- [25] Budd, W. F. and Carter, D. B. (1971). An analysis of the relation between the surface and bedrock profiles of ice caps. *Journal of Glaciology*, 10:197–209.
- [26] Burrough, P., McDonnell, R., Burrough, P., and McDonnell, R. (1998). *Principles of geographical information systems*, volume 333. Oxford University Press Oxford.
- [27] Caidong, C. and Asgeir, S. (2010). Modelled mass balance of Xibu glacier, Tibetan Plateau: sensitivity to climate change. *Journal of Glaciology*, 56:235–248(14).
- [28] Chander, G., Markham, B. L., and Helder, D. L. (2009). Summary of current radiometric calibration coefficients for Landsat MSS, TM, ETM+, and EO-1 ALI sensors. *Remote Sensing of Environment*, 113(5):893–903.
- [29] Chang, L. and Hanssen, R. (2015). A Probabilistic Approach for InSAR Time-Series Postprocessing. *IEEE Transactions on Geoscience and Remote Sensing*, 54(1):421–430.
- [30] Charney, J. G. and Eliassen, A. (1949). A Numerical Method for Predicting the Perturbations of the Middle Latitude Westerlies. *Tellus*, 1(2):38–54.
- [31] Copland, L., Pope, S., Bishop, M. P., Jr., J. F. S., Clendon, P., Bush, A., Kamp, U., Seong, Y. B., and Owen, L. A. (2009). Glacier velocities across the central Karakoram. *Annals of Glaciology*, 50:41–49.
- [32] Cuffey, K. and Paterson, W. S. B. (2010). *The Physics of Glaciers*. Academic Press.
- [33] Dehecq, A., Gourmelen, N., and Trouve, E. (2015). Deriving large-scale glacier velocities from a complete satellite archive: Application to the Pamir-Karakoram-Himalaya. *Remote Sensing of Environment*, 162(0):55 – 66.

- [34] Denby, B. and Greuell, W. (2000). The use of bulk and profile methods for determining surface heat fluxes in the presence of glacier winds. *Journal of Glaciology*, 46(154):445–452.
- [35] Denby, B. and Smeets, C. J. P. P. (2000). Derivation of Turbulent Flux Profiles and Roughness Lengths from Katabatic Flow Dynamics. *Journal of Applied Meteorology*, 39(9):1601–1612.
- [36] Denby, B. and Snellen, H. (2002). A comparison of surface renewal theory with the observed roughness length for temperature on a melting glacier surface. *Boundary-Layer Meteorology*, 103(3):459–468.
- [37] DeVries (2003). Effective aerodynamic roughness estimated from airborne laser altimeter measurements of surface features. *International Journal of Remote Sensing*, 24:1545–1558.
- [38] Ding, Y. and Chan, J. C. L. (2005). The East Asian summer monsoon: an overview. *Meteorology and Atmospheric Physics*, 89(1-4):117–142.
- [39] Ding, Y., Liu, S., Li, J., and Shangguan, D. (2006). The retreat of glaciers in response to recent climate warming in western China. *Annals of Glaciology*, 43(1):97–105.
- [40] Doake, C. and Vaughan, D. (1991). Rapid disintegration of the Wordie Ice Shelf in response to atmospheric warming. *Nature*, 350(6316):328–330.
- [41] Duan, A. and Wu, G. (2008). Weakening Trend in the Atmospheric Heat Source over the Tibetan Plateau during Recent Decades. Part I: Observations. *Journal of Climate*, 21(13):3149–3164.
- [42] Duan, K., Yao, T., and Thompson, L. G. (2006). Response of monsoon precipitation in the Himalayas to global warming. *Journal of Geophysical Research: Atmospheres*, 111(D19).
- [43] Duong, H., Lindenbergh, R., Pfeifer, N., and Vosselman, G. (2009). ICE-Sat full-waveform altimetry compared to airborne LASER scanning altimetry over the Netherlands. *IEEE Transactions on Geoscience and Remote Sensing*, 47(10):3365–3378.
- [44] Fasullo, J. (2004). A stratified diagnosis of the Indian Monsoon—Eurasian snow cover relationship. *Journal of Climate*, 17(5):1110–1122.
- [45] Fujisada, H., Bailey, G., Kelly, G., Hara, S., and Abrams, M. (2005). ASTER DEM performance. *IEEE Transactions on Geoscience and Remote Sensing*, 43(12):2707–2714.

- [46] Fujita, K. (2008). Effect of precipitation seasonality on climatic sensitivity of glacier mass balance. *Earth and Planetary Science Letters*, 276(1-2):14–19.
- [47] Fujita, K. and Ageta, Y. (2000). Effect of summer accumulation on glacier mass balance on the Tibetan Plateau revealed by mass-balance model. *Journal of Glaciology*, 46(153):244–252.
- [48] Fujita, K., Ohta, T., and Ageta, Y. (2007). Characteristics and climatic sensitivities of runoff from a cold-type glacier on the Tibetan Plateau. *Hydrological Processes*, 21(21):2882–2891.
- [49] Fujita, K., Seko, K., et al. (1996). Superimposed ice in glacier mass balance on the Tibetan Plateau. *Journal of Glaciology*, 42(142):454–460.
- [50] Gardelle, J., Berthier, E., and Arnaud, Y. (2012). Slight mass gain of Karakoram glaciers in the early 21st century. *Nature Geoscience*, 5:322–325.
- [51] Gardelle, J., Berthier, E., Arnaud, Y., and Kääb, A. (2013). Region-wide glacier mass balances over the Pamir-Karakoram-Himalaya during 1999–2011. *The Cryosphere*, 7(4):1263–1286.
- [52] Gardner, C. (1982). Target signatures for laser altimeters: an analysis. *Applied optics*, 21(3):448–453.
- [53] Gardner, C. (1992). Ranging performance of satellite laser altimeters. *IEEE Transactions on Geoscience and Remote Sensing*, 30(5):1061–1072.
- [54] Garratt, J. (1992). *The atmospheric boundary layer*. Cambridge University Press.
- [55] Hahn, D. G. and Shukla, J. (1976). An Apparent Relationship between Eurasian Snow Cover and Indian Monsoon Rainfall. *Journal of the Atmospheric Sciences*, 33(12):2461–2462.
- [56] He, H., McGinnis, J. W., Song, Z., and Yanai, M. (1987). Onset of the Asian Summer Monsoon in 1979 and the Effect of the Tibetan Plateau. *Monthly Weather Review*, 115(9):1966–1995.
- [57] Hewitt, K. (2011). Glacier change, concentration, and elevation effects in the Karakoram Himalaya, Upper Indus Basin. *Mount. Res. Dev.*, 31:188–200.
- [58] Hock, R. and Holmgren, B. (1996). Some aspects of energy balance and ablation of storglaciären, northern sweden. *Geografiska Annaler. Series A, Physical Geography*, 78(2/3):121–131.

- [59] Hoell, A., Barlow, M., and Saini, R. (2012). The Leading Pattern of Intraseasonal and Interannual Indian Ocean Precipitation Variability and Its Relationship with Asian Circulation during the Boreal Cold Season. *Journal of Climate*, 25(21):7509–7526.
- [60] Hooke, R. L. (2005). *Principles of glacier mechanics*. Cambridge University Press.
- [61] Hsu, H.-H. and Liu, X. (2003a). Relationship between the Tibetan Plateau heating and East Asian summer monsoon rainfall. *Geophysical Research Letters*, 30(20):2066–.
- [62] Hsu, H.-H. and Liu, X. (2003b). Relationship between the Tibetan Plateau heating and East Asian summer monsoon rainfall. *Geophysical Research Letters*, 30(20):2066.
- [63] Huang, M. (1990). On the temperature distribution of glaciers in China. *Journal of Glaciology*, 36(123):210–216.
- [64] Huffman, G. J., Adler, R. F., Bolvin, D. T., and Nelkin, E. J. (2010). The TRMM Multi-Satellite Precipitation Analysis (TMPA). pages 3–22. Springer Netherlands.
- [65] Huffman, G. J., Bolvin, D. T., Nelkin, E. J., Wolff, D. B., Adler, R. F., Gu, G., Hong, Y., Bowman, K. P., and Stocker, E. F. (2007). The TRMM Multi-satellite Precipitation Analysis (TMPA): Quasi-Global, Multiyear, Combined-Sensor Precipitation Estimates at Fine Scales. *Journal of Hydrometeorology*, 8(1):38–55.
- [66] Hutter, K. (1982). A mathematical model of polythermal glaciers and ice sheets. *Geophysical & Astrophysical Fluid Dynamics*, 21(3-4):201–224.
- [67] Hutter, K., Blatter, H., and Funk, M. (1988). A model computation of moisture content in polythermal glaciers. *Journal of Geophysical Research*, 93(B10):12205–12,214.
- [68] Immerzeel, W., Droogers, P., de Jong, S., and Bierkens, M. (2009). Large-scale monitoring of snow cover and runoff simulation in Himalayan river basins using remote sensing. *Remote Sensing of Environment*, 113(1):40–49.
- [69] Irvine-Fynn, T. D. L., Hodson, A. J., Moorman, B. J., Vatne, G., and Hubbard, A. L. (2011). Polythermal Glacier Hydrology: A Review. *Reviews of Geophysics*, 49(4):RG4002.

- [70] Jacob, T., Wahr, J., Pfeffer, W. T., and Swenson, S. (2012). Recent contributions of glaciers and ice caps to sea level rise. *Nature*, 482:514–518.
- [71] Kääb, A., Berthier, E., Nuth, C., Gardelle, J., and Arnaud, Y. (2012). Contrasting patterns of early twenty-first-century glacier mass change in the Himalayas. *Nature*, 488(7412):495–498.
- [72] Kang, S., Chen, F., et al. (2007a). Glacier retreating dramatically on Mt. Nyainqêntanglha during the last 40 years. *J. Glaciol. Geocryol.*, 29(6):869–873.
- [73] Kang, S., Chen, F., et al. (2007b). Glacier retreating dramatically on mt. Nyainqêntanglha during the last 40 years. *Journal of Glaciology and Geocryology*, 29(6):869–873.
- [74] Kang, S., Chen, F., et al. (2009). Early onset of rainy season suppresses glacier melt: A case study on Zhadang glacier, Tibetan Plateau. *Journal of Glaciology*, 55(192):755–758.
- [75] Kendall, M. G. and Stuart, A. (1977). *The Advanced Theory of Statistics: Distribution theory*. Macmillan.
- [76] Khaliq, M. N., Ouarda, T. B. M. J., Gachon, P., and Sushama, L. (2008). Temporal evolution of low-flow regimes in Canadian rivers. *Water Resources Research*, 44(8).
- [77] Kwok, R., Cunningham, G., Zwally, H., and Yi, D. (2006). ICESat over Arctic sea ice: Interpretation of altimetric and reflectivity profiles. *Journal of Geophysical Research*, 111(C6):C06006.
- [78] Kwon, M., Jhun, J.-G., and Ha, K.-J. (2007). Decadal change in east Asian summer monsoon circulation in the mid-1990s. *Geophysical Research Letters*, 34(21):n/a–n/a.
- [79] Lee, D., Storey, J., Choate, M., and Hayes, R. (2004). Four years of Landsat-7 on-orbit geometric calibration and performance. *IEEE Transactions on Geoscience and Remote Sensing*, 42(12):2786–2795.
- [80] Lei, Y., Yao, T., Bird, B. W., Yang, K., Zhai, J., and Sheng, Y. (2013). Coherent lake growth on the central tibetan plateau since the 1970s: Characterization and attribution. *Journal of Hydrology*, 483:61–67.
- [81] Lenaerts, J. T. M. (2013). *Drifting snow climate of the Antarctic and Greenland ice sheets*. PhD thesis, Utrecht University.

- [82] Leprince, S., Barbot, S., Ayoub, F., and Avouac, J.-P. (2007). Automatic and precise orthorectification, coregistration, and subpixel correlation of satellite images, application to ground deformation measurements. *IEEE Transactions on Geoscience and Remote Sensing*, 45(6):1529–1558.
- [83] Leprince, S., Muse, P., and Avouac, J.-P. (2008). In-Flight CCD Distortion Calibration for Pushbroom Satellites Based on Subpixel Correlation. *IEEE Transactions on Geoscience and Remote Sensing*, 46(9):2675–2683.
- [84] Li, C. and Yanai, M. (1996). The Onset and Interannual Variability of the Asian Summer Monsoon in Relation to Land–Sea Thermal Contrast. *Journal of Climate*, 9(2):358–375.
- [85] Li, J., Wu, Z., Jiang, Z., and He, J. (2010). Can Global Warming Strengthen the East Asian Summer Monsoon? *Journal of Climate*, 23(24):6696–6705.
- [86] Li, X., Cheng, G., Jin, H., Kang, E., Che, T., Jin, R., Wu, L., Nan, Z., Wang, J., and Shen, Y. (2008). Cryospheric change in China. *Global and Planetary Change*, 62(3-4):210–218. cited By 111.
- [87] Lin, H. (2009). Global Extratropical Response to Diabatic Heating Variability of the Asian Summer Monsoon. *Journal of the Atmospheric Sciences*, 66(9):2697–2713.
- [88] Liu, Y., Wu, G., Hong, J., Dong, B., Duan, A., Bao, Q., and Zhou, L. (2012). Revisiting Asian monsoon formation and change associated with Tibetan Plateau forcing: II. Change. *Climate Dynamics*, 39(5):1183–1195.
- [89] Lucchitta, B. and Ferguson, H. (1986). Antarctica: Measuring glacier velocity from satellite images. *Science*, 234(4780):1105–1108.
- [90] Manabe, S. and Broccoli, A. J. (1990). Mountains and Arid Climates of Middle Latitudes. *Science*, 247(4939):192–195.
- [91] Mann, H. B. (1945). Nonparametric tests against trend. *Econometrica*, 13(3):245–259.
- [92] Markham, B., Storey, J., Williams, D. L., and Irons, J. (2004). Landsat sensor performance: history and current status. *IEEE Transactions on Geoscience and Remote Sensing*, 42(12).
- [93] Maussion, F., Scherer, D., Mölg, T., Collier, E., Curio, J., and Finkelburg, R. (2013). Precipitation Seasonality and Variability over the Tibetan Plateau as Resolved by the High Asia Reanalysis*. *Journal of Climate*, 27(5):1910–1927.

- [94] Menenti, M. and Ritchie, J. C. (1994). Estimation of effective aerodynamic roughness of Walnut Gulch watershed with laser altimeter measurements. *Water Resources Research*, 30(5):1329–1337.
- [95] Mölg, T., Maussion, F., and Scherer, D. (2014). Mid-latitude westerlies as a driver of glacier variability in monsoonal High Asia. *Nature Climate Change*, 4(1):68–73.
- [96] Mölg, T., Maussion, F., Yang, W., and Scherer, D. (2012a). The footprint of Asian monsoon dynamics in the mass and energy balance of a Tibetan glacier. *The Cryosphere*, 6(6):1445–1461.
- [97] Mölg, T., Maussion, F., Yang, W., and Scherer, D. (2012b). The footprint of Asian monsoon dynamics in the mass and energy balance of a Tibetan glacier. *The Cryosphere*, 6(6):1445–1461.
- [98] Munro, D. (1989). Surface roughness and bulk heat transfer on a glacier: comparison with eddy correlation. *Journal of Glaciology*, 35(121).
- [99] Obukhov, A. M. (1971). Turbulence in an atmosphere with a non-uniform temperature. *Boundary-Layer Meteorology*, 2(1):7–29.
- [100] Oerlemans, J. (1993). Modelling of glacier mass balance. *Ice in the Climate System (Peltier, WR, ed.)*. NATO ASI Series I, 12:101–116.
- [101] Oerlemans, J. (2000). Analysis of a 3 year meteorological record from the ablation zone of Morteratschgletscher, Switzerland: energy and mass balance. *Journal of Glaciology*, 46:571–579.
- [102] Oerlemans, J. and Fortuin, J. (1992). Sensitivity of glaciers and small ice caps to greenhouse warming. *Science*, 258(5079):115.
- [103] Oke, T. (1987). *Boundary layer climates*. Routledge Press.
- [104] Pfeffer, W., Arendt, A., Bliss, A., Bolch, T., Cogley, J., Gardner, A., Hagen, J.-O., Hock, R., Kaser, G., Kienholz, C., Miles, E., Moholdt, G., M'ölg, N., Paul, F., Radić, V., Rastner, P., Raup, B., Rich, J., Sharp, M., Andreassen, L., Bajracharya, S., Barrand, N., Beedle, M., Berthier, E., Bhambri, R., Brown, I., Burgess, D., Burgess, E., Cawkwell, F., Chinn, T., Copland, L., Cullen, N., Davies, B., De Angelis, H., Fountain, A., Frey, H., Giffen, B., Glasser, N., Gurney, S., Hagg, W., Hall, D., Haritashya, U., Hartmann, G., Herreid, S., Howat, I., Jiskoot, H., Khromova, T., Klein, A., Kohler, J., K'önig, M., Krieger, D., Kutuzov, S., Lavrentiev, I., Le Bris, R., Li, X., Manley, W., Mayer, C., Menounos, B., Mercer, A., Mool, P., Negrete, A., Nosenko, G., Nuth, C., Osmonov, A., Pettersson, R., Racoviteanu,

- A., Ranzi, R., Sarikaya, M., Schneider, C., Sigurdsson, O., Sirguey, P., Stokes, C., Wheate, R., Wolken, G., Wu, L., and Wyatt, F. (2014). The Randolph Glacier Inventory: A globally complete inventory of glaciers. *Journal of Glaciology*, 60(221):537–552.
- [105] Pieczonka, T., Bolch, T., Junfeng, W., and Shiyin, L. (2013). Heterogeneous mass loss of glaciers in the aksu-tarim catchment (central tien shan) revealed by 1976 kh-9 hexagon and 2009 spot-5 stereo imagery. *Remote Sensing of Environment*, 130:233 – 244.
- [106] Pu, Z., Xu, L., and Salomonson, V. V. (2007). MODIS/Terra observed seasonal variations of snow cover over the Tibetan Plateau. *Geophysical Research Letters*, 34(6).
- [107] Qin, J., Yang, K., Liang, S., and Guo, X. (2009). The altitudinal dependence of recent rapid warming over the Tibetan Plateau. *Climatic Change*, 97(1-2):321–327.
- [108] Quincey, D., Copland, L., Mayer, C., Bishop, M., Luckman, A., and Belo, M. (2009a). Ice velocity and climate variations for Baltoro Glacier, Pakistan. *Journal of Glaciology*, 55(194):1061–1071.
- [109] Quincey, D., Luckman, A., and Benn, D. (2009b). Quantification of Everest region glacier velocities between 1992 and 2002, using satellite radar interferometry and feature tracking. *Journal of Glaciology*, 55(192):596–606.
- [110] Quincey, D. J., Braun, M., Glasser, N. F., Bishop, M. P., Hewitt, K., and Luckman, A. (2011). Karakoram glacier surge dynamics. *Geophysical Research Letters*, 38(18):L18504.
- [111] Rangwala, I. and Miller, J. (2012). Climate change in mountains: a review of elevation-dependent warming and its possible causes. *Climatic Change*, 114(3-4):527–547–.
- [112] Reiter, E. R. and Gao, D.-Y. (1982). Heating of the Tibet Plateau and Movements of the South Asian High During Spring. *Monthly Weather Review*, 110(11):1694–1711.
- [113] Rupper, S. and Roe, G. (2008). Glacier Changes and Regional Climate: A Mass and Energy Balance Approach*. *Journal of Climate*, 21(20):5384–5401.
- [114] Salomonson, V., Barnes, W., Maymon, P., Montgomery, H., and Ostrow, H. (1989). MODIS: advanced facility instrument for studies of the Earth as a system. *IEEE Transactions on Geoscience and Remote Sensing*, 27(2):145–153.

- [115] Scambos, T. A., Dutkiewicz, M. J., Wilson, J. C., and Bindschadler, R. A. (1992). Application of image cross-correlation to the measurement of glacier velocity using satellite image data. *Remote Sensing of Environment*, 42(3):177–186.
- [116] Scherler, D., Bookhagen, B., and Strecker, M. R. (2011). Spatially variable response of Himalayan glaciers to climate change affected by debris cover. *Nature Geoscience*, 4:156–159.
- [117] Scherler, D., Leprince, S., and Strecker, M. R. (2008). Glacier-surface velocities in alpine terrain from optical satellite imagery—accuracy improvement and quality assessment. *Remote Sensing of Environment*, 112(10):3806–3819.
- [118] Scherler, D. and Strecker, M. (2012). Large surface velocity fluctuations of Biafo Glacier, central Karakoram, at high spatial and temporal resolution from optical satellite images. *Journal of Glaciology*, 58(209):569–580.
- [119] Shaman, J. and Tziperman, E. (2005). The Effect of ENSO on Tibetan Plateau Snow Depth: A Stationary Wave Teleconnection Mechanism and Implications for the South Asian Monsoons. *Journal of Climate*, 18(12):2067–2079.
- [120] Shang, H., Jia, L., and Menenti, M. (2016). Modeling and Reconstruction of Time Series of Passive Microwave Data by Discrete Fourier Transform Guided Filtering and Harmonic Analysis. *Remote Sensing*, 8(11):970.
- [121] Shi, Y. and Liu, S. (2000). Estimation on the response of glaciers in China to the global warming in the 21st century. *Chinese Science Bulletin*, 45(7):668–672.
- [122] Shi, Y. F., Liu, C. H., et al. (2009). The Glacier Inventory of China. *Annals of Glaciology*, 50(53):1–4.
- [123] Shukla, J. (1984). Predictability of Time Averages: Part II: The Influence of the Boundary Forcings. *Topics in Atmospheric and Oceanographic Sciences*, pages 155–206. Springer Berlin Heidelberg.
- [124] Shukla, J. and Mooley, D. A. (1987). Empirical Prediction of the Summer Monsoon Rainfall over India. *Monthly Weather Review*, 115(3):695–704.
- [125] Solomon, S., Qin, D., Manning, M., Chen, Z., Marquis, M., Averyt, K., Tignor, M., and (eds.), H. M. (2007). *Fourth Assessment Report: Climate Change 2007: Working Group I Report: The Physical Science Basis*. Cambridge University Press.

- [126] Storey, J. and Choate, M. (2004). Landsat-5 bumper-mode geometric correction. *IEEE Transactions on Geoscience and Remote Sensing*, 42(12):2695–2703.
- [127] Stull, R. B. (2009). *An introduction to boundary layer meteorology*. Springer.
- [128] Su, Z., Schmugge, T., Kustas, W. P., and Massman, W. J. (2001). An evaluation of two models for estimation of the roughness height for heat transfer between the land surface and the atmosphere. *Journal of Applied Meteorology*, 40(11):1933–1951.
- [129] T. Heid and A. Käab (2012). Evaluation of existing image matching methods for deriving glacier surface displacements globally from optical satellite imagery. *Remote Sensing of Environment*, 118(0):339–355.
- [130] Toutin, T. and Cheng, P. (2001). DEM generation with ASTER stereo data. *Earth Observation Magazine*, 10(6):10–13.
- [131] Trenberth, K. E., Fasullo, J. T., and Mackaro, J. (2011). Atmospheric moisture transports from ocean to land and global energy flows in reanalyses. *Journal of Climate*, 24(18):4907–4924.
- [132] Van der Veen, C., Ahn, Y., Csatho, B., Mosley-Thompson, E., and Krabill, W. (2009). Surface roughness over the northern half of the Greenland Ice Sheet from airborne laser altimetry. *Journal of Geophysical Research*, 114(F1):F01001.
- [133] van Hoek, M., Jia, L., Zhou, J., Zheng, C., and Menenti, M. (2016). Early drought detection by spectral analysis of satellite time series of precipitation and normalized difference vegetation index (NDVI). *Remote Sensing*, 8(5):422.
- [134] Vincent, C., Ramanathan, A., Wagnon, P., Dobhal, D. P., Linda, A., Berthier, E., Sharma, P., Arnaud, Y., Azam, M. F., Jose, P. G., and Gardelle, J. (2013). Balanced conditions or slight mass gain of glaciers in the Lahaul and Spiti region (northern India, Himalaya) during the nineties preceded recent mass loss. *The Cryosphere*, 7(2):569–582.
- [135] Vogelmann, J. E., Helder, D., Morfitt, R., Choate, M. J., Merchant, J. W., and Bulley, H. (2001). Effects of Landsat 5 Thematic Mapper and Landsat 7 Enhanced Thematic Mapper Plus radiometric and geometric calibrations and corrections on landscape characterization. *Remote Sensing of Environment*, 78(1–2):55–70.

- [136] Wan, Z. (1996). A generalized split-window algorithm for retrieving land-surface temperature from space. *IEEE Transactions on Geoscience and Remote Sensing*, 34(4):892–905.
- [137] Wan, Z. (2008). New refinements and validation of the MODIS Land-Surface Temperature/Emissivity products. *Remote Sensing of Environment*, 112(1):59–74.
- [138] Wang, B., Bao, Q., Hoskins, B., Wu, G., and Liu, Y. (2008a). Tibetan Plateau warming and precipitation changes in East Asia. *Geophysical Research Letters*, 35(14):L14702.
- [139] Wang, B., Lee, J.-Y., Kang, I.-S., Shukla, J., Kug, J.-S., Kumar, A., Schemm, J., Luo, J.-J., Yamagata, T., and Park, C.-K. (2008b). How accurately do coupled climate models predict the leading modes of Asian-Australian monsoon interannual variability? *Climate Dynamics*, 30(6):605–619.
- [140] Wang, J., Zhu, L., Wang, Y., Ju, J., Xie, M., and Daut, G. (2010). Comparisons between the Chemical Compositions of Lake Water, Inflowing River Water, and Lake Sediment in Nam Co, Central Tibetan Plateau, China and their Controlling Mechanisms. *Journal of Great Lakes Research*, 36(4):587–595.
- [141] Wang, X., Gong, P., Zhao, Y., Xu, Y., Cheng, X., Niu, Z., Luo, Z., Huang, H., Sun, F., and Li, X. (2013). Water-level changes in China's large lakes determined from ICESat/GLAS data. *Remote Sensing of Environment*, 132:131–144.
- [142] Wang, Z. and Yang, H. (1992). Characteristics of the distribution of glaciers in China. *Annals of Glaciology*, 16:17–20.
- [143] Williams, D. L., Goward, S., and Arvidson, T. (2006). Landsat. *Photogrammetric Engineering & Remote Sensing*, 72(10):1171–1178.
- [144] Wu, G., Liu, Y., Zhang, Q., Duan, A., Wang, T., Wan, R., Liu, X., Li, W., Wang, Z., and Liang, X. (2007). The Influence of Mechanical and Thermal Forcing by the Tibetan Plateau on Asian Climate. *Journal of Hydrometeorology*, 8(4):770–789.
- [Wu et al.] Wu, H., Wang, N., Jiang, X., and Guo, Z. Variations in water level and glacier mass balance in Nam Co lake, Nyainqentanglha range, Tibetan Plateau, based on ICESat data for 2003-09. *Annals of Glaciology*, 55(66):239–247.
- [145] Wu, Z., Li, J., Jiang, Z., and Ma, T. (2012). Modulation of the Tibetan Plateau Snow Cover on the ENSO Teleconnections: From the East Asian Summer Monsoon Perspective. *Journal of Climate*, 25(7):2481–2489.

- [146] Wulder, M. A., White, J. C., Goward, S. N., Masek, J. G., Irons, J. R., Herold, M., Cohen, W. B., Loveland, T. R., and Woodcock, C. E. (2008). Landsat continuity: Issues and opportunities for land cover monitoring. *Remote Sensing of Environment*, 112(3):955–969.
- [147] Yamaguchi, Y., Kahle, A., Tsu, H., Kawakami, T., and Pniel, M. (1998). Overview of advanced spaceborne thermal emission and reflection radiometer (ASTER). *IEEE Transactions on Geoscience and Remote Sensing*, 36(4):1062–1071.
- [148] Yang, K., Guo, X., He, J., Qin, J., and Koike, T. (2010a). On the Climatology and Trend of the Atmospheric Heat Source over the Tibetan Plateau: An Experiments-Supported Revisit. *Journal of Climate*, 24(5):1525–1541.
- [149] Yang, K., Wu, H., Qin, J., Lin, C., Tang, W., and Chen, Y. (2014). Recent climate changes over the Tibetan Plateau and their impacts on energy and water cycle: A review. *Global and Planetary Change*, 112(0):79 – 91.
- [150] Yang, S. L., Liu, Z., Dai, S. B., Gao, Z. X., Zhang, J., Wang, H. J., Luo, X. X., Wu, C. S., and Zhang, Z. (2010b). Temporal variations in water resources in the Yangtze River (Changjiang) over the Industrial Period based on reconstruction of missing monthly discharges. *Water Resources Research*, 46(10).
- [151] Yang, W., Yao, T., Guo, X., Zhu, M., Li, S., and Kattel, D. B. (2013). Mass balance of a maritime glacier on the southeast Tibetan Plateau and its climatic sensitivity. *Journal of Geophysical Research: Atmospheres*, 118(17):9579–9594.
- [152] Yao, T., Masson-Delmotte, V., Gao, J., Yu, W., Yang, X., Risi, C., Sturm, C., Werner, M., Zhao, H., He, Y., Ren, W., Tian, L., Shi, C., and Hou, S. (2013). A review of climatic controls on $\delta^{18}O$ in precipitation over the Tibetan Plateau: Observations and simulations. *Reviews of Geophysics*, 51(4):2012RG000427.
- [153] Yao, T., Pu, J., Lu, A., Wang, Y., and Yu, W. (2007a). Recent glacial retreat and its impact on hydrological processes on the Tibetan Plateau, China, and surrounding regions. *Arctic, Antarctic, and Alpine Research*, 39(4):642–650.
- [154] Yao, T., Pu, J., Lu, A., Wang, Y., and Yu, W. (2007b). Recent glacial retreat and its impact on hydrological processes on the Tibetan Plateau, China, and surrounding regions. *Arctic, Antarctic, and Alpine Research*, 39:642–650.
- [155] Yao, T., Thompson, L., Yang, W., Yu, W., Gao, Y., Guo, X., Yang, X., Duan, K., Zhao, H., Xu, B., Pu, J., Lu, A., Xiang, Y., Kattel, D. B., and Joswiak, D. (2012). Different glacier status with atmospheric circulations in Tibetan Plateau and surroundings. *Nature Climate Change*, 2(9):663–667.

- [156] Ye, D. (1981). Some Characteristics of the Summer Circulation Over the Qinghai-Xizang (Tibet) Plateau and Its Neighborhood. *Bulletin of the American Meteorological Society*, 62(1):14–19.
- [157] Ye, D. and Wu, G. (1998). The role of the heat source of the Tibetan Plateau in the general circulation. *Meteorology and Atmospheric Physics*, 67(1-4):181–198.
- [158] Yi, D. H., Zwally, H. J., et al. (2005). ICESat measurement of Greenland ice sheet surface slope and roughness. *Annals of Glaciology*, 42:83–89.
- [159] Yong, B., Liu, D., Gourley, J. J., Tian, Y., Huffman, G. J., Ren, L., and Hong, Y. (2015). Global view of real-time TRMM multisatellite precipitation analysis: implications for its successor global precipitation measurement mission. *Bulletin of the American Meteorological Society*, 96(2):283–296.
- [160] Yu, W., Yao, T., Kang, S., Pu, J., Yang, W., Gao, T., Zhao, H., Zhou, H., Li, S., Wang, W., and Ma, L. (2013). Different region climate regimes and topography affect the changes in area and mass balance of glaciers on the north and south slopes of the same glacierized massif (the West Nyainqentanglha Range, Tibetan Plateau). *Journal of Hydrology*, 495:64–73.
- [161] Yuan, C., Tozuka, T., Miyasaka, T., and Yamagata, T. (2009). Respective influences of IOD and ENSO on the Tibetan snow cover in early winter. *Climate Dynamics*, 33(4):509–520–.
- [162] Zhang, B., Wu, Y., Zhu, L., Wang, J., Li, J., and Chen, D. (2011). Estimation and trend detection of water storage at Nam Co Lake, central Tibetan Plateau. *Journal of Hydrology*, 405(1–2):161–170.
- [163] Zhang, G., Kang, S., Fujita, K., Huintjes, E., Xu, J., Yamazaki, T., Haginoya, S., Wei, Y., Scherer, D., Schneider, C., and Yao, T. (2013). Energy and mass balance of Zhadang glacier surface, central Tibetan Plateau. *Journal of Glaciology*, 59(213):137–148.
- [164] Zhang, G., Xie, H., Yao, T., Liang, T., and Kang, S. (2012). Snow cover dynamics of four lake basins over tibetan plateau using time series MODIS data (2001–2010). *Water Resources Research*, 48(10):W10529.
- [Zhou et al.] Zhou, S., Kang, S., Chen, F., and Joswiak, D. R. Water balance observations reveal significant subsurface water seepage from Lake Nam Co, south-central Tibetan Plateau. *Journal of Hydrology*, 491:89–99.
- [165] Zongtai, W. and Huian, Y. (1992). Characteristics of the distribution of glaciers in China. *Annals of Glaciology*, 16:17–20.